Shear strength estimation of rock discontinuities –
Are the present roughness quantifications forward-looking for engineering use?

vorgelegt von
M.Sc.
Kristofer Marsch
ORCID: 0000-0002-1857-506X

an der Fakultät VI - Planen Bauen Umwelt
der Technischen Universität Berlin
zur Erlangung des akademischen Grades

Doktor der Ingenieurwissenschaften
- Dr.-Ing. -

genehmigte Dissertation

Promotionsausschuss:

Vorsitzender:	Prof. Dr.-Ing. Frank Rackwitz
Gutachter:	Prof. Dr. Tomas M. Fernandez-Steeger
Gutachter:	Prof. Dr. habil. Kurosch Thuro

Tag der wissenschaftlichen Aussprache: 16. Dezember 2021

Berlin 2022

für T.

Abstract

When the subsurface is used for technical structures such as caverns or artificial slopes, the natural stress balance is disturbed. As a result, the stresses redistribute. Naturally, pre-existing zones of weakness, e.g., faults, and "planar breaks" of all kinds, commonly referred to as discontinuities, are places where stresses concentrate. Since discontinuities determine the overall strength of a rock mass, means are needed to determine the strength of these planes of weakness. To this end, numerous empirical criteria have been proposed. They are all based on index parameters, among which the roughness of the shear surfaces plays an important role.

In this thesis, the measurement and quantification of the surface roughness are investigated. The focus is directed towards (i) the deficiencies of the quality of the surface representations in past studies and (ii) the lack of comprehensive documentation together with unknown sensitivity of the calculation schemes. Consequently, light is to be shed on whether complex roughness parameterisation and detailed surface mapping are constructive towards better shear strength estimation.

To answer these questions, state-of-the-art optical measurement techniques for the generation of 3D surface models are evaluated in chapter 2. Special attention is given to the capabilities of Structure-from-Motion/Dense Image Matching (SfM/DIM) techniques for obtaining high-resolution micro relief maps of some tensile fractures. The metrological reference data on surface models produced with a terrestrial laser scanner (TLS), SfM/DIM and a hand-held scanner were generated with a structured light scanner. Since the comparison of geometric data generated by different scanners suffers heavily from registration errors, the statistical and fractal roughness parameters derived from the 3D models are compared directly. From the analysis of the distributions of the Joint Roughness Coefficient (JRC) and Grasselli's roughness parameter (GP), it is concluded that SfM/DIM produces data suitable for the evaluation of micro-roughness. On the other hand, the derivation of micro-roughness from TLS data should be discarded. Furthermore, large differences in the calculation of the JRC between statistical and fractal methods become apparent. This finding leads as if by itself to the second study of this thesis in chapter 3.

All correlations of JRC with statistical and fractal indices are based on Barton's well-known and widely accepted type-profiles. For virtually every correlation equation, the standard chart has been digitised, although not always with due care. The renewed evaluation of three data sets of the type profiles in chapter 3 shows that most statistical indices are robust to measurement and digitalisation inaccuracies, but on the side of the fractal approaches this is only the case for the so-called *root mean square correlation*. Furthermore, important adjusting screws of the fractal approaches are dealt with, and the methods are described in full. Although the above is important in itself because a sensitivity analysis has not been done before, the crucial part of the study is a cross-validation with new independent data, some of which comes from chapter 2. Of course,

all methods lead to very similar JRC values for the type profiles. However, this is not the case for the six tensile fractures analysed here. In particular, fractal spectral analysis is overly complex and does not lead to better roughness estimates than simple statistical means.

As the goal of roughness parameterisation is to estimate the shear strength, in chapter 4, the findings of the previous chapters are applied to direct shear test data. Opposed to many prior works in which replica materials were used, real rock tensile surfaces are tested here. Additionally, as the the rock materials used exhibit much larger strength the study investigates the applicability of existing empirical shear criteria established based on low strength materials to high strength rocks. The roughness is parameterised using the well-established JRC and GP. It is shown that the shear strength is overestimated in 35% of the cases using Grasselli's roughness whereas applying the JRC leads to the underestimation of shear strength in most cases. Apparently, the two roughness parameterisations fail to account for "nonuniform roughness" elements such as singular, pronounced asperities which seemingly dominate the shearing process for high strength rocks.

In summary, the shear strength estimated based on the JRC calculated from SfM/DIM data is on the safe side. Especially with high strength rock, due to the presence of "nonuniform roughness", larger than estimated shear strength capacity can be assumed. A more nuanced, at best rock type related portfolio of constitutive equations is desirable.

Zusammenfassung

Die Nutzung des Untergrunds für technische Bauwerke wie Kavernen oder künstliche Hänge führt zur Störung des Spannungsgleichgewichts. In der Folge kommt es zu einer Umlagerung der Spannungen. Naturgemäß konzentrieren sich die Spannungen an bereits vorhandenen Schwächezonen, zum Beispiel Störungen und "flächige Brüche" aller Art, die gemeinhin als Trennflächen bezeichnet werden. Da diese die Gesamtfestigkeit eines Gebirges bestimmen, sind Mittel erforderlich, um ihre Festigkeit zu ermitteln. Zu diesem Zweck wurden zahlreiche empirische Scherfestigkeitskriterien vorgeschlagen. Sie beruhen alle auf Indexparametern, unter denen die Rauigkeit eine wichtige Rolle spielt.

In dieser Arbeit wird die Messung und Quantifizierung der Oberflächenrauigkeit untersucht. Der Fokus richtet sich dabei auf (i) die Mängel bei der Qualität der Oberflächendarstellung in früheren Studien und (ii) dem Mangel an umfassender Dokumentation zusammen mit der unbekannten Empfindlichkeit der Berechnungsschemata. Folglich soll geklärt werden, ob eine komplexe Parametrisierung der Rauigkeit und eine detaillierte Oberflächendarstellung zu einer besseren Abschätzung der Scherfestigkeit beitragen.

Zur Beantwortung dieser Fragen werden in Kapitel 2 modernste optische Messverfahren zur Erzeugung von 3D-Oberflächenmodellen evaluiert. Besonderes Augenmerk wird dabei auf die Möglichkeiten der Structure-from-Motion/Dense Image Matching (SfM/DIM)-Techniken zur Erstellung von hochaufgelösten Mikroreliefkarten einiger Zugbrüche gelegt. Die messtechnischen Referenzdaten zu Oberflächenmodellen, die mit einem terrestrischen Laserscanner (TLS), SfM/DIM und einem Handscanner erstellt wurden, wurden mit einem strukturierten Weißlicht-Scanner erzeugt. Da der Vergleich von geometrischen Daten, die von verschiedenen Scannern stammen, stark unter Fehlern in der Registrierung leiden, werden die statistischen und fraktalen Rauigkeitsparameter, die aus den 3D-Modellen abgeleitet werden, direkt verglichen. Aus der Analyse der Verteilungen des Joint Roughness Coefficient (JRC) und Grassellis Rauigkeitsparameter (GP) wird geschlossen, dass SfM/DIM Daten erzeugt, die für die Bewertung der Mikrorauigkeit geeignet sind. Andererseits sollte die Ableitung der Mikrorauigkeit aus TLS-Daten verworfen werden. Darüber hinaus werden große Unterschiede in der Berechnung der JRC zwischen statistischen und fraktalen Methoden deutlich. Dieser Befund stellt die natürliche Überleitung zu der zweiten Studie dieser Arbeit in Kapitel 3 dar.

Alle Korrelationen des JRC mit statistischen und fraktalen Indizes beruhen auf den bekannten und weithin akzeptierten Typ-Profilen von Barton. Für praktisch jede Korrelation wurde das Standard-Diagramm digitalisiert, wenn auch nicht immer mit der gebotenen Sorgfalt. Die erneute Auswertung von drei Datensätzen der Typ-Profile in Kapitel 3 zeigt, dass die meisten statistischen Indizes robust gegenüber Mess- und Digitalisierungsungenauigkeiten sind. Auf der Seite der fraktalen Ansätze ist dies jedoch nur für die so genannte *root mean square correlation* der Fall. Außerdem werden wichtige

Stellschrauben der fraktalen Ansätze behandelt und die Methoden ausführlich beschrieben. Obwohl die obigen Ausführungen an sich schon bedeutsam sind, weil eine Sensitivitätsanalyse bisher noch nicht durchgeführt wurde, ist der entscheidende Teil der Studie eine Kreuzvalidierung mit neuen unabhängigen Daten, von denen einige aus Kapitel 2 stammen. Natürlicherweise führen alle Methoden zu sehr ähnlichen JRC-Werten für die Typ-Profile. Dies ist jedoch bei den sechs hier untersuchten Zugbrüchen nicht der Fall. Insbesondere die fraktale Spektralanalyse ist übermäßig komplex und führt nicht zu besseren Rauigkeitsabschätzungen als einfache statistische Mittel.

Da das Ziel der Rauigkeitsparametrisierung die Abschätzung der Scherfestigkeit ist, werden die neuen Erkenntnisse in Kapitel 4 auf Ergebnisse direkter Scherversuche angewandt. Im Gegensatz zu vielen früheren Arbeiten, in denen Abgüsse von Trennflächen verwendet wurden, werden hier echte Zugrissoberflächen getestet. Da die verwendeten Gesteinsmaterialien eine wesentlich höhere Festigkeit aufweisen, wird außerdem die Anwendbarkeit bestehender empirischer Scherfestigkeitskriterien, die auf der Grundlage von Abgüssen mit geringer Festigkeit aufgestellt wurden, für hochfeste Gesteine untersucht. Die Rauigkeit wird mit Hilfe der bewährten JRC und GP parametrisiert. Es zeigt sich, dass die Scherfestigkeit in 35% der Fälle unter Verwendung der Grasselli-Rauigkeit überschätzt wird, während die Anwendung des JRC in den meisten Fällen zu einer Unterschätzung der Scherfestigkeit führt. Offensichtlich berücksichtigen die beiden Rauigkeitsparametrisierungen keine "ungleichmäßigen Rauigkeitselemente" wie z.B. einzelne, ausgeprägte Erhebungen, die den Scherprozess bei hochfestem Gestein zu dominieren scheinen.

Zusammenfassend lässt sich sagen, dass die Scherfestigkeit, die auf der Grundlage der aus SfM/DIM-Daten berechneten JRC geschätzt wird, auf der sicheren Seite liegt. Insbesondere bei hochfestem Gestein kann aufgrund des Vorhandenseins von "ungleichmäßiger Rauigkeit" von einer größeren Scherfestigkeit als der geschätzten ausgegangen werden. Ein nuancierteres, bestenfalls felsartbezogenes Portfolio von konstitutiven Gleichungen ist wünschenswert.

Contents

Chapter 1

Introduction

1.1 Motivation

Safety and economic rationality are the guidelines for all engineering works. To do justice to these in rock engineering, a sound assessment of the mechanical behaviour of the receiving rock mass, and particularly of possible weakness zones within, is needed. Primarily "planar breaks" of varying sizes determine the overall strength and entail rock masses to behave mechanically discontinuous. Consequently, the term *discontinuity* was chosen by the International Society for Rock Mechanics (ISRM) as a collective description of planar defects having zero or low tensile strength (ISRM, 1978b). In general, the properties of these discontinuities are of greater importance to the rock mass strength than the properties of the intact rock material (Bieniawski, 1989). Discontinuities relevant to engineering works could extend from tenths of millimetres (e.g. foliation) to hundreds of metres (e.g. faults). They originate from various geological processes and develop for example during sedimentation (bedding planes), due to tectonic stress (cleavage), due to thermal elasticity (exfoliation planes) or as results of loading/unloading events (joints).

Historically in engineering contexts, the term joint — despite its clear geological definition as the denomination for penetrative, repetitive planar breaks without appreciable shear displacement — is used for all or parts of the family of discontinuities in rock masses (Goodman, 1976). This lingering inconsistency may find its explanation in the field of modern rock mechanics itself as it formed as independent but overlapping research branch in geology and civil engineering in the 1960s. Still today, from the larger frequency of joints compared to other discontinuities in many rock masses subject to rock engineering Hencher and Richards (2015) deduce using the term joint synonymously with discontinuity admissible. Although being rather impure, this practice is followed here to enhance reading complaisance and to conform with common practise.

For the design of civil engineering structures in rock masses such as underground openings, cuts and slopes for infrastructure projects or foundations, means of determining the strength of the planes of weakness in lateral displacement, referred to as shear strength, are needed. It is along these discontinuities obviously where stress is transferred very differently compared to, on the macro-scale, continuous rock: while generally discontinuities exhibit substantial normal strength, even though smaller than intact rock material, they show drastically lower shear strength.

As it is costly in terms of labour to gather meaningful, intact joint samples from boreholes or outcrops and to conduct a significant number of direct shear tests, many empirical shear strength criteria incorporating index parameters have been put forward for

engineering use. Comprehensive yet not all-embracing compilations of these criteria can be found in Singh and Basu (2018) and (with transcription errors) in Li et al. (2020). The derivation of these criteria routinely consists of the following triad:

1. determining the strength of the rock material, commonly in terms of the basic friction angle (ϕ_b) and the uniaxial compressive (σ_C) or tensile strength (σ_T),
2. surface roughness measurement and quantification (for which numerous approaches exist) and
3. conducting direct shear tests for the deduction of mathematical formulas and/or for calibration.

The first and third points above, namely the determination of the strength parameters and the execution of direct shear tests, are altogether well standardised (c.f. ISRM, 1978a, 1979; Muralha et al., 2014; Alejano et al., 2018). Instead, amongst the available shear strength criteria the measurement and the quantification of the surface roughness are hardly comparable. On the one hand, the quality and the meaningfulness of the surface representations are often neglected and have not been investigated thoroughly. On the other hand, comprehensive documentation, and therefore traceability, of common roughness calculation schemes as well as an examination of their sensitivity are also missing. Taking a practitioner's point of view, this thesis therefore aims at evaluating whether

- detailed surface mapping and
- complex roughness parameterisation

are constructive towards better shear strength estimation. The necessity and timeliness of this work is due to the recently increasing availability and usage of highly capable sensors and algorithms for surveying rock surface topography. Before that background, put bluntly, should rock engineers use sophisticated measuring devices and elaborate roughness parametrisations simply because they now can?

1.2 Roughness characterisation

The abstract concept of roughness is used as a matter of course throughout the rock mechanics community. This is rather peculiar since no standard for use in rock engineering exists which exactly defines the meaning of roughness. Only the aged Suggested Methods for the Quantitative Description of Discontinuities in Rock Masses (ISRM, 1978b), though contradictory to their title, establish a framework at least for descriptive terms for the appearance of rock surface profiles. However, no standardised procedures for quantifying roughness have been introduced so far. Instead, many different calculation approaches for two-dimensional as well as three-dimensional roughness measures were developed in the past (c.f. Magsipoc et al., 2020). Note that in this thesis dimension is understood in terms of Euclidean space, meaning profiles are considered 2D objects (having x- and y-coordinates) whereas surface representations are regarded 3D objects (having x-,y- and z-coordinates).

1.2.1 ISRM nomenclature

For a start, in the introductory glossary of the Suggested Methods strangely the term roughness is used for the definition of the same. It is stated there that roughness is the

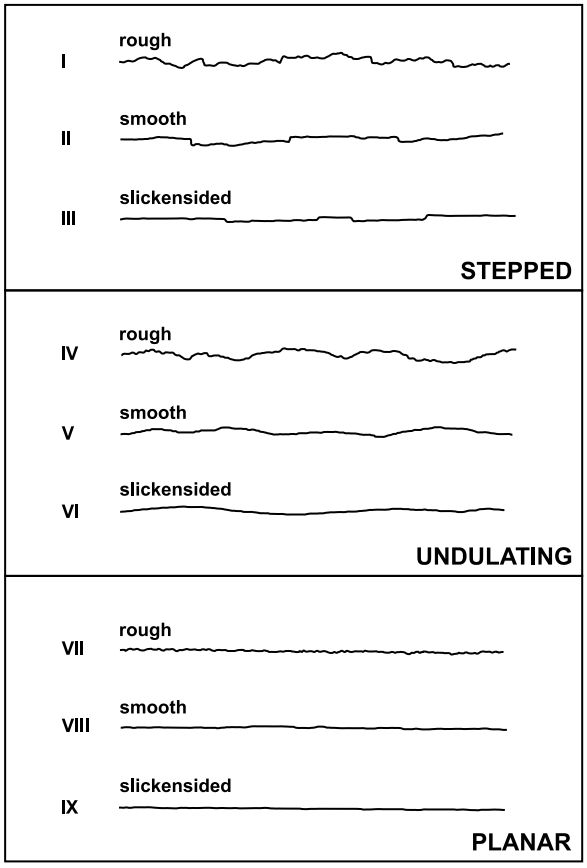

Figure 1.1: ISRM nomenclature for *unevenness*, lengths of profiles in the range of 1 to 10 metres (redrawn from ISRM, 1978b)

"inherent surface roughness and waviness relative to the mean plane of a discontinuity" (ISRM, 1978b, p. 321). However, it is left open what is to be understood by "mean plane". Yet, subsequently the meaning of roughness is narrowed down as follows:

> "In general terms the roughness of discontinuity walls can be characterized by a *waviness* (large scale undulations which, if interlocked and in contact, cause dilation during shear displacement since they are too large to be sheared off) and by an *unevenness* (small scale roughness that tends to be damaged during shear displacement unless the discontinuity walls are of high strength and/or the stress levels are low, so that dilation can also occur on these small scale features)." (ISRM, 1978b, p. 338)

Whereas *waviness* describes surface height differences over tens of metres, *unevenness* applies to smaller scale, namely to profiles ranging from 1 to 10 metres in length according to Figure 1.1. Moreover, *unevenness* subdivides further into intermediate scale (several metres) and small scale (several centimetres). On the intermediate scale profiles appear stepped, undulating or planar. Instead, they appear rough/irregular, smooth or slickensided on small scale. Although, the comparative table of Figure 1.1 facilitates the use of the concept of *unevenness* it is rather indecisive due to the large range of possible profile lengths that could be described based on it.

For further clarification the ISRM nomenclature is visualised in Figure 1.2. In that figure also the so-called Joint Roughness Coefficient (JRC), introduced by Barton (1973),

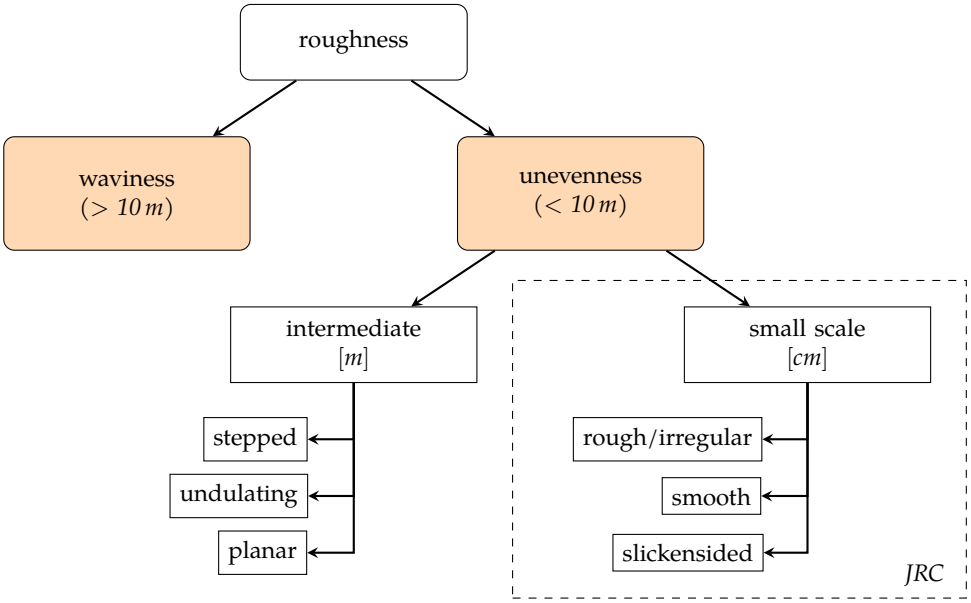

Figure 1.2: Structure of the ISRM nomenclature

is mentioned. This is because the Suggested Methods reproduces the JRC standard chart from Barton and Choubey (1977) (which is discussed below). However, the reference is made in the context of shear strength estimation and, therefore, strictly speaking, the JRC should not be considered part of the ISRM roughness nomenclature.

1.2.2 Joint Roughness Coefficient

First and foremost, it must be beard in mind that Barton's original definition of the Joint Roughness Coefficient is primarily of a mechanical nature. The basis for the JRC is formed of a series of direct shear tests conducted on model tension fractures made of some artificial, concrete-like compound. The specimens were assumed to "represent the roughest end of the joint spectrum" (Barton, 1973). The test results were then fitted with a newly introduced, enhanced Mohr-Coulomb equation incorporating the strength of the rock material in the form of the basic friction angle (ϕ_b) and the uniaxial compressive strength (σ_C). Solving that equation for JRC, which therefore has no geometrical information inscribed in it and which is purely a mathematical fitting parameter, leads to the following definition (c.f. Barton, 1973):

$$\text{JRC} = \frac{\tan^{-1}(\tau/\sigma_n) - \phi_b}{\log_{10}\left(\frac{\sigma_C}{\sigma_n}\right)} \tag{1.1}$$

with τ being the peak shear strength at a normal stress of σ_n.

However, targeting the estimation of shear strength without labour-intensive laboratory tests, examples of roughness profiles were also given as "preliminary efforts to improve the classification and description of non-planar joints" (Barton, 1973). The six profiles are depicted in Figure 1.3. Profiles A are described as "rough undulating" whereas profiles B are termed "smooth undulating". The appearance of profiles C is characterised as "smooth nearly planar". The associated JRC for A, B and C are 20, 10 and 5. However, the examples given have lengths of 500 mm and 5000 mm, respectively, which is surprising because the original test surfaces were only 60 mm by 25 mm in size (c.f. Barton,

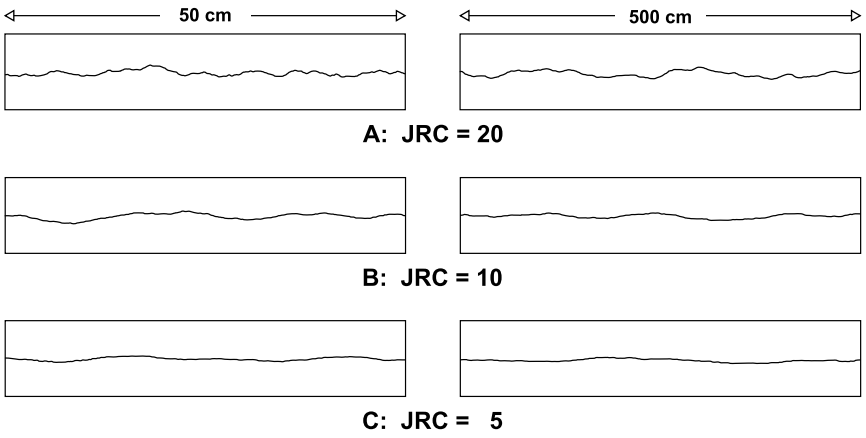

Figure 1.3: Six early examples of JRC roughness profiles (redrawn from Barton, 1973)

1971). Unfortunately, this inconsistency was not further explained and therefore the profiles should be viewed with caution.

Establishing exemplary profiles was resumed by Barton and Choubey (1977) who introduced a widely acknowledged chart showing ten roughness profiles with associated JRC ranges. It is reproduced in Figure 1.4 and it will be referred to as "the standard chart" or "the type-profiles" throughout this thesis. The chart was intended to enable practitioners "in the preliminary stages of a rock engineering project [...] to make a quick estimate to discover if the shear strength of the joints is so low that closer investigation is required" (Barton and Choubey, 1977).

The basis for the standard chart in turn is formed of some 140 rock joint specimens which were tested in direct shear. On the surfaces three profiles were measured using a tactile profile gauge with rods of 1 mm in diameter. The profiles were grouped according to the back calculated JRC (using Equation 1.1) and "an attempt was then made to select the most typical profiles of each group" (Barton and Choubey, 1977). However, the selection process was not further described and, consequently, the grounds on which these profiles were deemed to be representative are untraceable. The type-profiles are therefore not objective.

Promptly after the introduction of the type-profiles the practise of estimating JRC from subjective and rather unconcerned human eye-based comparison was questioned (for example, Beer et al. (2002) showed that every rock engineer has her/his own understanding of the visual JRC). First correlations of some statistical parameters with JRC based on the standard chart were introduced by Tse and Cruden (1979). Instead, Turk et al. (1987) were the first to put forward a function for JRC based on a fractal approach. Collections of the many works that followed since then can be found in Li and Zhang (2015) and Li and Huang (2015). Furthermore, other approaches exist, however being used singularly (e.g. Ficker and Martišek, 2016; Wang et al., 2017; Yong et al., 2018; Gravanis and Pantelidis, 2019).

Additionally, when making use of the JRC concept, the scale of the surfaces in question must be considered. With regards to the type-profiles, which are meaningful only to profiles of 100 mm in length, a reduction of JRC with increasing sample size was postulated (c.f. Barton and Choubey, 1977). Bandis et al. (1981) formalised this observation and introduced the following mathematical relationship:

$$\mathrm{JRC}_n \approx \mathrm{JRC}_0 \left(\frac{L_n}{L_0}\right)^{-0.02 \cdot \mathrm{JRC}_0} \tag{1.2}$$

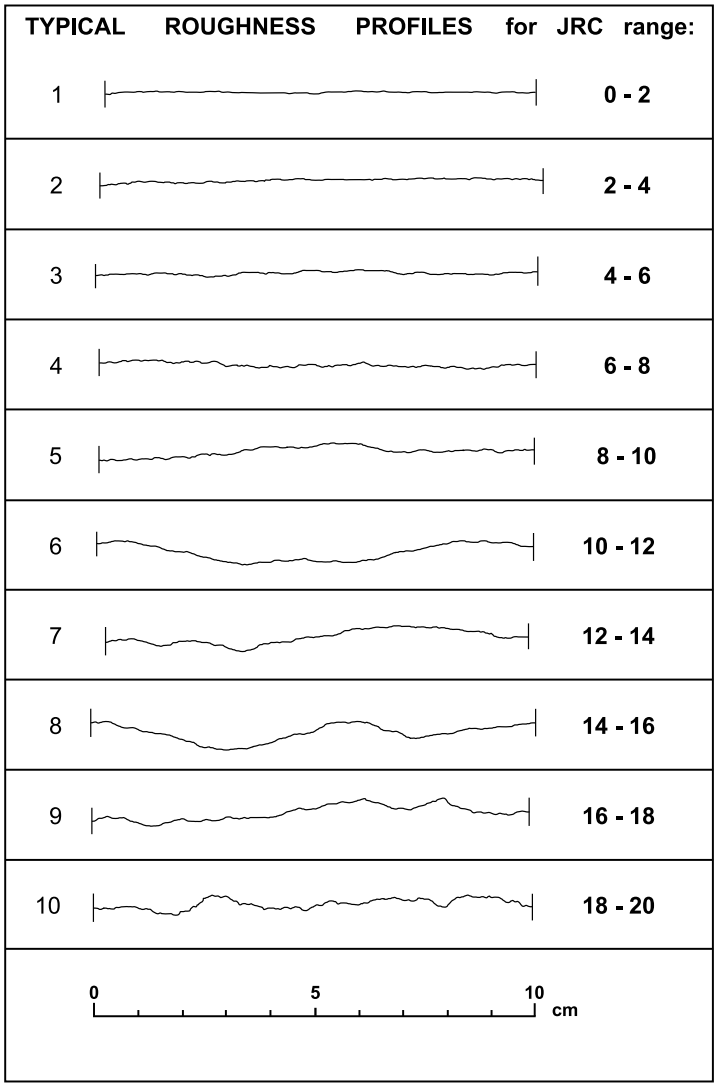

Figure 1.4: JRC standard chart containing the 10 type-profiles (redrawn from Barton and Choubey, 1977)

with JRC_0 being the roughness estimated on the standard length $L_0 = 100\,\text{mm}$ and JRC_n being the roughness on the length of interest L_n.

Concerning JRC, in summary, presumably due to its early introduction point in time and mentioning in the Suggested Methods, it became an unofficial, quasi-standard for rock roughness quantification in general. This becomes manifest in the mentioning of the concept in many textbooks on rock engineering, in numerous publications on correlations of JRC with all kinds of mathematical parameters and in the most recent adoption of the type-profiles in the revised standard ISO 14689 (2017) for the identification, description and classification of rock.

1.2.3 Two-dimensional and three-dimensional roughness parameters

When the ISRM nomenclature and the JRC were published in the 1970s the availability of powerful technical devices, in terms of resolution and accuracy, for the full reconstruction of joint surfaces was limited. Consequently, the characterisation of roughness referred only to 2D profiles. Not until the turn of the millennium, Grasselli et al. (2002) made 3D measurements of rock joints acceptable.

In principle, applying both for 2D or 3D roughness quantification there are two well-established categories, namely (i) statistical approaches and (ii) fractal schemes. With statistical methods the point coordinates of the surface representations are directly analysed. Instead, with fractal methods elaborate algorithms "beyond the general ideas of statistics" (Magsipoc et al., 2020) must be used.

Regarding 3D roughness quantification, according to Magsipoc et al. (2020) the widely accepted concept from Grasselli et al. (2002) deserves its own category, being a set of three "directional" parameters which merge in one measure, abbreviated as GP (Grasselli Parameter) in this thesis. Moreover, with Grasselli's notion, and for example with the approach from Ge et al. (2015) also, the real triangulated surface models are used directly (i). Opposite to that for example Renard et al. (2006) or Candela et al. (2009) used parameters averaged over a large number of linear profiles (ii) which are therefore rather pseudo three-dimensional measures.

Most obviously, the main argument for usage of 3D roughness parameterisations is the nature of shear failure on its own: rock blocks are practically never only in linear contact. According to Grasselli et al. (2002) "the shear strength of the joint, damage location, and joint morphology are strongly inter-dependent". Consequently, their spatial morphology as whole should be accounted for (e.g. Kulatilake et al., 1995; Gentier et al., 2000). To date still a major drawback for three-dimensional parameters is the lack of referential data. If at all, in prior works only the calculated roughness values were listed instead of providing the full raw data of the surface representations (e.g. Grasselli and Egger, 2003; Xia et al., 2014; Li et al., 2020). This makes calibration and validation of possible new 3D roughness parameterisations unfeasible. Moreover, the rock engineering community seemingly has limited itself lately to the application of Grasselli's roughness approach as the standard 3D procedure. It is incorporated in many recent empirical shear strength criteria (c.f. Li et al., 2020).

Concerning the determination of surface roughness from some profiles, indeed sufficiency must be questioned especially because their minimal representative number is unknown (Belem et al., 2000). However, there are efforts to resolve this issue for example by Li et al. (2019) through spiral sampling or by Yong et al. (2019) through overlapping sampling. Most importantly, roughness profiles are well accepted, captured easily in the field and laboratory, and have proven themselves useful in preliminary design (c.f. Hudson and Harrison, 1997). Moreover, the recent standard ISO 14689 (2017) considers the

JRC type-profiles and extends their meaning to larger scales. Consequently, it is reasonable to retain profile methods as a means of rock roughness characterisation at least in practical rock engineering.

1.2.4 Rock mass classifications

Remember, the estimation of rock mass strength for engineering works is the primary motivation for roughness characterisation as it is one influential factor in the overall strength. Therefore, it is reasonable to review rock mass classification systems on that topic, namely in what way and in which amount roughness is incorporated in the final rating of the rock mass. Many of these formalised techniques "were developed to create some order out of the chaos in site investigation procedures and to provide the desperately needed design aids" (Bieniawski, 1989). Mostly, they evolved during tunnelling projects in the 1970s.

One of the two broadly accepted classification schemes is the "Engineering Classification of Rock Masses for the Design of Tunnel Support" formulated by Barton et al. (1974), becoming well known under the abbreviation *Q-System*. In that framework the roughness of the discontinuities is quantified in terms of a *joint roughness number* (J_r). This parameter essentially picks up the suggested nomenclature from the ISRM as also undulating and planar roughness is delineated on the intermediate scale and rough, smooth and slickensided appearance on the small scale. According to these descriptions a factor in the range of 0.5 to 4 is determined which merges into a summarising equation to calculate the Q-value as a measure of the overall quality of the rock mass. It must be realised that the determination of J_r based on exemplary profiles is rather subjective as no details are given on the selection process of the divisions mentioned above.

The other most common classification is the *Rock Mass Rating System* (RMR). Bieniawski (1989) describes the RMR most comprehensively in a manual on engineering rock mass classifications in general. That version is frequently referred to as RMR89 whereas the version by Celada et al. (2014) is named RMR14. Most recently, Kundu et al. (2020) introduced continuous functions for each rating category of the RMR to overcome the original discrete nature of rating assignment. They also incorporate a function for roughness rating based on JRC. However, this new approach has yet to prove its usefulness in practise. Up to date, in general, within the RMR the roughness of the discontinuities is considered only by means of qualitative, visual descriptions according to "guidelines for classification of discontinuity conditions". There, five roughness classes are defined: very rough, rough, slightly rough, smooth and slickensided. Based on these classes individual ratings between 0 and 6 points are assigned. No further explanations on how to objectively select one of these categories are given. Most importantly however, in the introductory part of his manual Bieniawski (1989) defines roughness as "the nature of the asperities in the discontinuity surfaces" and states that "asperities usually have a base length and amplitude measured in millimeters and are readily apparent on a core-sized exposure of a discontinuity". However, in the part of RMR on discontinuity conditions, also ratings must be chosen for the discontinuity length in grades of several metres. Consequently, rating the discontinuities on one hand on millimetre-scale and on the other hand on metre-scale is rather inconsistent.

Instead, the *Geological Strength Index* (GSI) introduced by Hoek (1994), which is widely seen also as a rock mass classification system, was initially intended to enable the determination of the constants of the Hoek-Brown failure criterion. At first, a simple chart with descriptions of the structure and the surface conditions of the rock mass was given. However, since the axes were rather arbitrary Hoek et al. (2013) suggested to

quantify the structure of the rock mass by means of the *Rock Quality Designation* (RQD) and the surface conditions by means of using the partial rating for the discontinuity conditions (JCond89) of the RMR89 system. Other approaches to scale the axes of the original GSI chart also exist (e.g. Cai et al., 2004). It must be realised though that all these efforts resort to earlier rock mass classifications such as the Q-System, RMR or RMi (Palmstrøm, 1996). Consequently, the "quantified GSI" is not a system of its own and follows similar subjective descriptions within the characterisation of the roughness as described above.

In summary, considering the rock mass classifications mentioned here, the particular qualitative descriptions for the appearance of roughness profiles set rather stretchable frameworks.

1.2.5 ISO standards

In other academic fields the definition of roughness is more detailed. Especially, it is profitable to consider the definition of roughness from mechanical and materials engineering. There, a chain of standards for geometrical product specifications exists (c.f. ISO 8015, 2011) of which standard ISO 4287 (1997) deals with surface texture obtained from profile measurements (2D) whereas standard ISO 25178-2 (2012) deals with surface texture based on areal measurements (3D).

In ISO 4287 (1997) roughness and waviness are considered separate textural characteristics of a surface. This is contrary to the ISRM Suggested Methods (ISRM, 1978b) where roughness is defined as a combination of unevenness and waviness (see above). According to ISO 4287 (1997) instead, roughness and waviness are to be separated by a cut-off wavelength which depends on the tip radius of the contact (stylus) instrument used for profile capturing as given in ISO 3274 (1996). This hints at the crucial point of roughness being inseparably linked to the sampling capabilities of the used scanning device. Most importantly, it is also stated in ISO 4287 (1997) that in order to calculate any roughness measure from surface profiles a datum line must be established: the so-called "mean line" is the "line determined by fitting a least-squares line of nominal form through the primary profile" (ISO 4287, 1997). With reference to that line for example the arithmetic mean of the absolute ordinate values (Ra, being an amplitude parameter) or the mean value of the profile element widths (RSm, being a spacing parameter) can be calculated.

In the context of ISO 25178-2 (2012) for areal texture characterisation surfaces can be quantified by height parameters and spatial parameters. Of course, these parameters are also comparative measures with respect to a reference surface, which is the "surface associated to the scale-limited surface [of interest] according to a criterion" (ISO 25178-2, 2012). However, what such a criterion would be is not clarified. Instead concerning this matter information is given in standard ISO 17450-3 (2016) where it is stated that "by default [...] associations for establishing a geometrical feature [...] are established from the total least squares (Gaussian) objective function" (ISO 17450-3, 2016). This means that a reference plane (as for a profile) should be produced by fitting a least-squares plane through the measured surface. Within the fitting process it is of paramount importance to include all points from the measured surface as otherwise a shift of the reference plane location could occur (c.f. ISO 17450-3, 2016). In turn, this could change the deduced textural parameters.

Indeed, the definitions of roughness from mechanical and materials engineering are purely geometric and, unlike JRC and GP, do not have a mechanical meaning. However, from the standards described above, it can be learned that it is essential to establish

datum lines or planes for roughness definition based on clear, universally applicable criteria. However, this topic has been rather neglected in research on rock joint roughness. Clearly, standardised procedures for the establishment of planes of reference are needed to achieve full comparability of future works.

1.3 Surveying of rock surfaces

Upon thinking about reconstructing the topography of surfaces, intuitively tactile measuring equipment comes to mind. In addition, contact stylus instruments are used by default in material science. Unlike man-made surfaces however, rock joints are not always flat and macroscopically smooth which makes high resolution tactile instruments inapplicable. The subtle stylus tips tend to get caught at the steep steps of rock surfaces that originate for example from tectonic processes or simply from the rock mineral grains themselves. Yet, profile gauges, also referred to as tactile profilometers or "Barton combs", exhibiting much larger tips (usually 0.8 or 1 mm) are basic tools in rock roughness characterisation. However, their low accuracy and commonly very limited sample size are major issues. Instead, contact-less optical instruments at least do not exhibit these troubles.

For the selection of optical measuring devices, the first step is to define the scale of observation. In the previous section it was explained that in rock engineering roughness is usually characterised in the range of millimetres to a few tens of metres. This is because morphological features of discontinuities on sub-millimetre scale, namely micrometre scale ($1\ \mu\text{m} = 10^{-3}$ mm), are not relevant to dilation (c.f. Hencher and Richards, 2015). Consequently, they need not to be captured. This assessment makes it unnecessary for this thesis to consider some surface metrology systems such as scanning electron (SEM), confocal, or focus-variation microscopy. A shortlist including other methods can be found in standard ISO 25178-6 (2010).

Naturally, however, there are instances where roughness on sub-millimetre scale could be of interest. For example, investigating the basic friction angle, Pérez-Rey et al. (2020) used a focus-variation apparatus to visualise grooves on saw-cut sample surfaces. Another example is that of Kim and Jeon (2019) who applied SEM for investigating roughness decrease due to shearing, heating, and fluid flow in drill cores. Their results, however, should not be extrapolated due to scale dependent textural differences of the material.

In general, due to rapid advances in technology, reconstructing the earth's surface using optical approaches, such as LiDAR (Light Detection and Ranging) or, in a broad sense, photogrammetry, has been thriving. Concerning the use of terrestrial laser scanning (TLS) for example, studies have increased steadily over the last two decades and continue to increase today (Telling et al., 2017). On the side of photogrammetry, further developing Structure-from-Motion (SfM) workflows in conjunction with dense image matching (DIM), imported from computer vision disciplines and allowing high versatility and usability (Abellan et al., 2016), became indispensable in many earth sciences as essential tools for digital surface mapping (Eltner et al., 2016). In this thesis the terms SfM and DIM are used synonymously as reconstructing the spatial distribution of camera positions using point correspondences between individual images via SfM is a prerequisite to produce dense point clouds using DIM algorithms. However, in the geoscience community unlike in the field of computer vision and surveying technology a distinction between SfM and DIM is commonly not made and SfM is used as a collective term for the process of producing dense point clouds from uncalibrated imagery

(e.g. Westoby et al., 2012; Bemis et al., 2014; Eltner et al., 2016).

For in-situ rock discontinuity characterisation, for example Sturzenegger and Stead (2009) compared TLS and SfM on close range. Bistacchi et al. (2011) instead used a combination of TLS and SfM for a fault characterisation over hundreds of metres. Their primary objective of using SfM was to fill in regions in the lower resolution LiDAR data with high-resolution SfM data. Consequently, their work hints at limitations concerning the scale of application of the surveying techniques. In general, TLS is an accepted tool for the investigation of rock slope instabilities (c.f. Jaboyedoff et al., 2012; Abellán et al., 2014) and the derived point clouds provide the basis for the presently advancing automatic mapping of discontinuities (c.f. Riquelme et al., 2018). Instead, the use of SfM/DIM exclusively for small-scale roughness determination in terms of JRC has been rather limited until now. Apart from Kim et al. (2013, 2015), just recently, Salvini et al. (2020) and García-Luna et al. (2021) conducted studies on that topic.

However, for scanning laboratory-size samples the optical measuring method used most is laser profilometry (e.g. Brown, 1995; Fardin et al., 2001; Ishibashi et al., 2015). The application of laser profilometers is straightforward and usually resolutions and accuracies of about 25 μm can be achieved. A limitation of laser profilometers is their mechanical robustness; consequently, they are used seldom in the field.

Due to increasing economic viability structured light scanners (SLS) have also become often-used tools in rock roughness characterisation (e.g. Tatone and Grasselli, 2013; Vogler et al., 2017). They are standard measuring devices in the engineering industry and feature high resolution and accuracy. As for the laser profilometers, the sensitiveness of SLS however precludes broad usage for fieldwork.

Since there exist different optical measuring techniques, the choice which of them to use for rock roughness characterisation is not obvious. The supreme premise must always be the scale of observation and the resolution of the device. From that, also the needed accuracy should be determined.

1.4 Outline and objectives of this thesis

Three papers reproduced in the following chapters 2, 3 and 4 form the core of this cumulative dissertation. While the manuscripts are self-contained, as whole they retrace in parts the three-step process of establishing empirical shear strength criteria as mentioned in the motivation. However, the focus is directed on the pitfalls of the individual steps of (i) measuring and (ii) quantifying roughness. It is not the aim of this thesis to introduce a new shear strength criterion or roughness parameterisation as there are already plenty. Also, the goal is not to create a new sampling manner for JRC but to emphasise that the application of JRC on laboratory-scale has departed from its original intentions. This thesis shall rather critically review existing works however based on original, new data and consequently new insights to delineate possible dead ends and divert future work on the topic of roughness characterisation for shear strength estimation to potentially more promising paths.

Chapter 2: "On the usability of different optical measuring techniques for joint roughness evaluation"

Marsch K, Wujanz D, Fernandez-Steeger, TM (2020) On the usability of different optical measuring techniques for joint roughness evaluation. *B Eng Geol Environ* 79:811–830. `https://doi.org/10.1007/s10064-019-01606-y`

As first step, four different optical measuring techniques are compared in chapter 2. The need for such a comparison stems from the present lack of standardised procedures to produce surface representations as inputs for rock roughness characterisation. In previous studies different, sometimes self-constructed measuring techniques have been used, each time singularly. The meaningfulness of the deduced roughness measures however should be questioned because no references were used. Naturally, different surveying approaches result in different models regarding resolution and accuracy. Consequently, in chapter 2 three measuring techniques/sensors are compared to referential data produced using a SLS scanner which is a highly developed, standard metrology system. Since the use of SfM in geosciences increases drastically, yet on larger scales of observation, the primary goal of chapter 2 is to explore its applicability to small scale roughness determination.

Chapter 3: "Comparative Evaluation of Statistical and Fractal Approaches for JRC Calculation Based on a Large Dataset of Natural Rock Traces"

Marsch K, Fernandez-Steeger, TM (2021) Comparative Evaluation of Statistical and Fractal Approaches for JRC Calculation Based on a Large Dataset of Natural Rock Traces. *Rock Mech Rock Eng* 54:1897-1917.
`https://doi.org/10.1007/s00603-020-02348-0`

Various mathematical concepts for calculating JRC from the standard chart exist. By far, statistical and fractal schemes have been used most and are broadly accepted. It must be kept in mind that correlating JRC with these measures always refers to the type-profiles. However, their number is small, their initial measurement resolution is low and they are presented only graphically. As many studies lack a thorough, comprehensive evaluation and documentation of the calculation approaches used chapter 3 of this thesis aims at investigating the sensitivity of the roughness measures to parameter variation within their particular mathematical formulations as well as the sensitivity to the input signals. Consequently, the objective is to evaluate the robustness of statistical and fractal JRC calculation approaches. Moreover, the general hypothesis of interchangeability of different JRC calculation schemes is tested, which coercively derives from their referencing to the standard chart. This was achieved by cross-validation using over 40,000 original rock traces thereby extending the data space drastically.

Chapter 4: "Incoherency of replica-based shear strength criteria regarding tensile fractures with high wall strength"

Marsch K, Fernandez-Steeger, TM (2021) submitted to *Rock Mech Min Sci* (Elsevier)

Since chapters 2 and 3 cover rock roughness on a geometrical basis, its mechanical meaning is investigated in chapter 4 based on direct shear test results. Many empirical shear strength criteria have been established using rock replica material. This is understandable because it renders possible testing the same surface topographies under different normal stress. However, replica materials like cement, mortar, or concrete exhibit lower strength than many rock materials. Consequently, the deduced empirical equations might suffer from an imbalance concerning the influence of the wall strength versus the influence of the roughness on the overall peak shear strength. The aim of chapter 4 is therefore to verify whether existing shear strength criteria can be extrapolated to high strength rock. For the selection of the criteria to be tested only those resorting to JRC

and GP are considered because that ensures comparative figures being available. In this context also the questions shall be answered whether scanning the entire surface is beneficial to the determination of JRC and whether three-dimensional GP improves shear strength estimation.

Chapter 5: "Synthesis"

In this chapter the conclusions from chapters 2, 3 and 4 are summarised. They are coalesced to answer the questions formulated in this introduction. Finally, the courses of action of the individual studies are discussed from which suggestions for future studies are derived.

1.5 References

Abellan, A., Derron, M.-H., and Jaboyedoff, M. (2016). "Use of 3D Point Clouds in Geohazards" Special Issue: Current Challenges and Future Trends. *Remote Sensing*, 8(2):130. https://doi.org/10.3390/rs8020130.

Abellán, A., Oppikofer, T., Jaboyedoff, M., Rosser, N. J., Lim, M., and Lato, M. J. (2014). Terrestrial laser scanning of rock slope instabilities. *Earth Surf Proc Land*, 39(1):80–97. https://doi.org/10.1002/esp.3493.

Alejano, L., Muralha, J., Ulusay, R., Li, C., Pérez-Rey, I., Karakul, H., Chryssanthakis, P., and Aydan, O. (2018). ISRM suggested method for determining the basic friction angle of planar rock surfaces by means of tilt tests. *Rock Mech Rock Eng*, 51(12):3853–3859. https://doi.org/10.1007/s00603-018-1627-6.

Bandis, S., Lumsden, A., and Barton, N. (1981). Experimental studies of scale effects on the shear behaviour of rock joints. *Int J Rock Mech Min*, 18(1):1–21. https://doi.org/10.1016/0148-9062(81)90262-x.

Barton, N. (1971). A relationship between joint roughness and joint shear strength. *Proceedings Symposium on Rock Fracture, September, 1971, Nancy, France*.

Barton, N. (1973). Review of a new shear-strength criterion for rock joints. *Eng Geol*, 7(4):287–332. https://doi.org/10.1016/0013-7952(73)90013-6.

Barton, N. and Choubey, V. (1977). The shear strength of rock joints in theory and practice. *Rock Mech*, 10(1-2):1–54. https://doi.org/10.1007/bf01261801.

Barton, N., Lien, R., and Lunde, J. (1974). Engineering classification of rock masses for the design of tunnel support. *Rock Mech*, 6(4):189–236. https://doi.org/10.1007/bf01239496.

Beer, A., Stead, D., and Coggan, J. (2002). Technical note estimation of the joint roughness coefficient (JRC) by visual comparison. *Rock Mech Rock Eng*, 35(1):65–74. https://doi.org/10.1007/s006030200009.

Belem, T., Homand-Etienne, F., and Souley, M. (2000). Quantitative parameters for rock joint surface roughness. *Rock Mech Rock Eng*, 33(4):217–242. https://doi.org/10.1007/s006030070001.

Bemis, S. P., Micklethwaite, S., Turner, D., James, M. R., Akciz, S., Thiele, S. T., and Bangash, H. A. (2014). Ground-based and UAV-based photogrammetry: A multi-scale, high-resolution mapping tool for structural geology and paleoseismology. *J Struct Geol*, 69:163–178. https://doi.org/10.1016/j.jsg.2014.10.007.

Bieniawski, Z. (1989). *Engineering Rock Mass Classifications*. John Wiley and Sons, New York.

Bistacchi, A., Griffith, W. A., Smith, S. A., Toro, G. D., Jones, R., and Nielsen, S. (2011). Fault roughness at seismogenic depths from LIDAR and photogrammetric analysis. *Pure Appl Geophys*, 168(12):2345–2363. https://doi.org/10.1007/s00024-011-0301-7.

Brown, S. R. (1995). Simple mathematical model of a rough fracture. *J Geophys Res - Sol Ea*, 100(B4):5941–5952. https://doi.org/10.1029/94jb03262.

Cai, M., Kaiser, P., Uno, H., Tasaka, Y., and Minami, M. (2004). Estimation of rock mass deformation modulus and strength of jointed hard rock masses using the GSI system. *Int J Rock Mech Min*, 41(1):3–19. https://doi.org/10.1016/s1365-1609(03)00025-x.

Candela, T., Renard, F., Bouchon, M., Brouste, A., Marsan, D., Schmittbuhl, J., and Voisin, C. (2009). Characterization of fault roughness at various scales: Implications of three-dimensional high resolution topography measurements. *Pure Appl Geophys*, 166(10-11):1817–1851. https://doi.org/10.1007/s00024-009-0521-2.

Celada, B., Tardáguila, I., Varona, P., Rodríguez, A., and Bieniawski, Z. (2014). Innovating tunnel design by an improved experience-based RMR system. *Proceedings World Tunnel Congress, May 9-14, 2014, Foz do Iguaçu, Brazil*.

Eltner, A., Kaiser, A., Castillo, C., Rock, G., Neugirg, F., and Abellán, A. (2016). Image-based surface reconstruction in geomorphometry – merits, limits and developments. *Earth Surf Dynam*, 4(2):359–389. https://doi.org/10.5194/esurf-4-359-2016.

Fardin, N., Stephansson, O., and Jing, L. (2001). The scale dependence of rock joint surface roughness. *Int J Rock Mech Min*, 38(5):659–669. https://doi.org/10.1016/s1365-1609(01)00028-4.

Ficker, T. and Martišek, D. (2016). Alternative method for assessing the roughness coefficients of rock joints. *J Comput Civil Eng*, 30(4):04015059. https://doi.org/10.1061/(asce)cp.1943-5487.0000540.

García-Luna, R., Senent, S., and Jimenez, R. (2021). Using telephoto lens to characterize rock surface roughness in SfM models. *Rock Mech Rock Eng*. https://doi.org/10.1007/s00603-021-02373-7.

Ge, Y., Tang, H., Eldin, M. M. E., Chen, P., Wang, L., and Wang, J. (2015). A description for rock joint roughness based on terrestrial laser scanner and image analysis. *Scientific Reports*, 5(1):16999. https://doi.org/10.1038/srep16999.

Gentier, S., Riss, J., Archambault, G., Flamand, R., and Hopkins, D. (2000). Influence of fracture geometry on shear behavior. *Int J Rock Mech Min*, 37(1-2):161–174. https://doi.org/10.1016/s1365-1609(99)00096-9.

Goodman, R. E. (1976). *Methods of Geological Engineering in Discontinuous Rocks*. West Publishing, St. Paul.

Grasselli, G. and Egger, P. (2003). Constitutive law for the shear strength of rock joints based on three-dimensional surface parameters. *Int J Rock Mech Min*, 40(1):25–40. https://doi.org/10.1016/s1365-1609(02)00101-6.

Grasselli, G., Wirth, J., and Egger, P. (2002). Quantitative three-dimensional description of a rough surface and parameter evolution with shearing. *Int J Rock Mech Min*, 39(6):789–800. https://doi.org/10.1016/s1365-1609(02)00070-9.

Gravanis, E. and Pantelidis, L. (2019). Determining of the joint roughness coefficient (JRC) of rock discontinuities based on the theory of random fields. *Geosciences*, 9(7):295. https://doi.org/10.3390/geosciences9070295.

Hencher, S. and Richards, L. (2015). Assessing the shear strength of rock discontinuities at laboratory and field scales. *Rock Mech Rock Eng*, 48(3):883–905. https://doi.org/10.1007/s00603-014-0633-6.

Hoek, E. (1994). Strength of rock and rock masses. *ISRM News Journal*, 2(2):4–16.

Hoek, E., Carter, T., and Diederichs, M. (2013). Quantification of the geological strength index chart. *Proceedings 47th U.S. Rock Mechanics/Geomechanics Symposium, June 23–26, 2013, San Francisco, CA*.

Hudson, J. A. and Harrison, J. P. (1997). *Engineering Rock Mechanics*. Pergamon, Amsterdam.

Ishibashi, T., Watanabe, N., Hirano, N., Okamoto, A., and Tsuchiya, N. (2015). Beyond-laboratory-scale prediction for channeling flows through subsurface rock fractures with heterogeneous aperture distributions revealed by laboratory evaluation. *J Geophys Res - Sol Ea*, 120(1):106–124. https://doi.org/10.1002/2014jb011555.

ISO 14689 (2017). Geotechnical investigation and testing — identification, description and classification of rock. Standard, International Organization for Standardization, Geneva, CH. https://www.iso.org/standard/66347.html.

ISO 17450-3 (2016). Geometrical product specifications (GPS) — general concepts — part 3: Toleranced features. Standard, International Organization for Standardization, Geneva, CH. https://www.iso.org/standard/62309.html.

ISO 25178-2 (2012). Geometrical product specifications (GPS) — surface texture: Areal — part 2: Terms, definitions and surface texture parameters. Standard, International Organization for Standardization, Geneva, CH. https://www.iso.org/standard/42785.html.

ISO 25178-6 (2010). Geometrical product specifications (GPS) — surface texture: Areal — part 6: Classification of methods for measuring surface texture. Standard, International Organization for Standardization, Geneva, CH. https://www.iso.org/standard/42896.html.

ISO 3274 (1996). Geometrical product specifications (GPS) — surface texture: Profile method — nominal characteristics of contact (stylus) instruments. Standard, International Organization for Standardization, Geneva, CH. https://www.iso.org/standard/1916.html.

ISO 4287 (1997). Geometrical product specifications (GPS) – surface texture: Profile method – terms, definitions and surface texture parameters. Standard, International Organization for Standardization, Geneva, CH. https://www.iso.org/standard/10132.html.

ISO 8015 (2011). Geometrical product specifications (GPS) — fundamentals — concepts, principles and rules. Standard, International Organization for Standardization, Geneva, CH. https://www.iso.org/standard/55979.html.

ISRM (1978a). Suggested methods for determining tensile strength of rock materials. *Int J Rock Mech Min*, 15(3):99–103. https://doi.org/10.1016/0148-9062(78)90003-7.

ISRM (1978b). Suggested methods for the quantitative description of discontinuities in rock masses. *Int J Rock Mech Min*, 15(6):319–368. https://doi.org/10.1016/0148-9062(78)91472-9.

ISRM (1979). Suggested methods for determining the uniaxial compressive strength and deformability of rock materials. *Int J Rock Mech Min*, 16(2):137. https://doi.org/10.1016/0148-9062(79)91450-5.

Jaboyedoff, M., Oppikofer, T., Abellán, A., Derron, M.-H., Loye, A., Metzger, R., and Pedrazzini, A. (2012). Use of LIDAR in landslide investigations: a review. *Nat Hazards*, 61(1):5–28. https://doi.org/10.1007/s11069-010-9634-2.

Kim, D. H., Gratchev, I., and Balasubramaniam, A. (2013). Determination of joint roughness coefficient (JRC) for slope stability analysis: a case study from the gold coast area, australia. *Landslides*, 10(5):657–664. https://doi.org/10.1007/s10346-013-0410-8.

Kim, D. H., Poropat, G. V., Gratchev, I., and Balasubramaniam, A. (2015). Improvement of photogrammetric JRC data distributions based on parabolic error models. *Int J Rock Mech Min*, 80:19–30. https://doi.org/10.1016/j.ijrmms.2015.09.007.

Kim, T. and Jeon, S. (2019). Experimental study on shear behavior of a rock discontinuity under various thermal, hydraulic and mechanical conditions. *Rock Mech Rock Eng*, 52(7):2207–2226. https://doi.org/10.1007/s00603-018-1723-7.

Kulatilake, P., Shou, G., Huang, T., and Morgan, R. (1995). New peak shear strength criteria for anisotropic rock joints. *Int J Rock Mech Min*, 32(7):673–697. https://doi.org/10.1016/0148-9062(95)00022-9.

Kundu, J., Sarkar, K., Singh, A. K., and Singh, T. (2020). Continuous functions and a computer application for rock mass rating. *Int J Rock Mech Min*, 129:104280. https://doi.org/10.1016/j.ijrmms.2020.104280.

Li, Y. and Huang, R. (2015). Relationship between joint roughness coefficient and fractal dimension of rock fracture surfaces. *Int J Rock Mech Min*, 75:15–22. https://doi.org/10.1016/j.ijrmms.2015.01.007.

Li, Y., Mo, P., Aydin, A., and Zhang, X. (2019). Spiral sampling method for quantitative estimates of joint roughness coefficient of rock fractures. *Geotech Test J*, 42(1):245–255. https://doi.org/10.1520/gtj20170213.

Li, Y., Tang, C., Li, D., and Wu, C. (2020). A new shear strength criterion of three-dimensional rock joints. *Rock Mech Rock Eng*, 53(3):1477–1483. https://doi.org/10.1007/s00603-019-01976-5.

Li, Y. and Zhang, Y. (2015). Quantitative estimation of joint roughness coefficient using statistical parameters. *Int J Rock Mech Min*, 77:27–35. https://doi.org/10.1016/j.ijrmms.2015.03.016.

Magsipoc, E., Zhao, Q., and Grasselli, G. (2020). 2d and 3d roughness characterization. *Rock Mech Rock Eng*, 53(3):1495–1519. https://doi.org/10.1007/s00603-019-01977-4.

Muralha, J., Grasselli, G., Tatone, B., Blümel, M., Chryssanthakis, P., and Yujing, J. (2014). ISRM suggested method for laboratory determination of the shear strength of rock joints: Revised version. *Rock Mech Rock Eng*, 47(1):291–302. https://doi.org/10.1007/s00603-013-0519-z.

Palmstrøm, A. (1996). Characterizing rock masses by the RMi for use in practical rock engineering. *Tunn Undergr Sp Tech*, 11(2):175–188. https://doi.org/10.1016/0886-7798(96)00015-6.

Pérez-Rey, I., Bastante, F. G., Alejano, L. R., and Mas Ivars, D. (2020). Influence of microroughness on the frictional behavior and wear response of planar saw-cut rock surfaces. *Int J Geomech*, 20(8):04020118. https://doi.org/10.1061/(asce)gm.1943-5622.0001742.

Renard, F., Voisin, C., Marsan, D., and Schmittbuhl, J. (2006). High resolution 3d laser scanner measurements of a strike-slip fault quantify its morphological anisotropy at all scales. *Geophys Res Lett*, 33(4). https://doi.org/10.1029/2005gl025038.

Riquelme, A., Tomás, R., Cano, M., Pastor, J. L., and Abellán, A. (2018). Automatic mapping of discontinuity persistence on rock masses using 3d point clouds. *Rock Mech Rock Eng*, 51(10):3005–3028. https://doi.org/10.1007/s00603-018-1519-9.

Salvini, R., Vanneschi, C., Coggan, J. S., and Mastrorocco, G. (2020). Evaluation of the use of UAV photogrammetry for rock discontinuity roughness characterization. *Rock Mech Rock Eng*, 53(8):3699–3720. https://doi.org/10.1007/s00603-020-02130-2.

Singh, H. and Basu, A. (2018). Evaluation of existing criteria in estimating shear strength of natural rock discontinuities. *Eng Geol*, 232:171–181. https://doi.org/10.1016/j.enggeo.2017.11.023.

Sturzenegger, M. and Stead, D. (2009). Close-range terrestrial digital photogrammetry and terrestrial laser scanning for discontinuity characterization on rock cuts. *Eng Geol*, 106(3-4):163–182. https://doi.org/10.1016/j.enggeo.2009.03.004.

Tatone, B. S. A. and Grasselli, G. (2013). An investigation of discontinuity roughness scale dependency using high-resolution surface measurements. *Rock Mech Rock Eng*, 46(4):657–681. https://doi.org/10.1007/s00603-012-0294-2.

Telling, J., Lyda, A., Hartzell, P., and Glennie, C. (2017). Review of earth science research using terrestrial laser scanning. *Earth-Sci Rev*, 169:35–68. https://doi.org/10.1016/j.earscirev.2017.04.007.

Tse, R. and Cruden, D. (1979). Estimating joint roughness coefficients. *Int J Rock Mech Min*, 16(5):303–307. https://doi.org/10.1016/0148-9062(79)90241-9.

Turk, N., Greig, M., Dearman, W., and Amin, F. (1987). Characterization of rock joint surfaces by fractal dimension. *Proceedings 28th Symp. Rock Mechanics, June 29 - July 1, 1987, Tucson, AZ*.

Vogler, D., Walsh, S. D., Bayer, P., and Amann, F. (2017). Comparison of surface properties in natural and artificially generated fractures in a crystalline rock. *Rock Mech Rock Eng*, 50(11):2891–2909. https://doi.org/10.1007/s00603-017-1281-4.

Wang, L., Wang, C., Khoshnevisan, S., Ge, Y., and Sun, Z. (2017). Determination of two-dimensional joint roughness coefficient using support vector regression and factor analysis. *Eng Geol*, 231:238–251. https://doi.org/10.1016/j.enggeo.2017.09.010.

Westoby, M., Brasington, J., Glasser, N., Hambrey, M., and Reynolds, J. (2012). 'structure-from-motion' photogrammetry: A low-cost, effective tool for geoscience applications. *Geomorphology*, 179:300–314. https://doi.org/10.1016/j.geomorph.2012.08.021.

Xia, C.-C., Tang, Z.-C., Xiao, W.-M., and Song, Y.-L. (2014). New peak shear strength criterion of rock joints based on quantified surface description. *Rock Mech Rock Eng*, 47(2):387–400. https://doi.org/10.1007/s00603-013-0395-6.

Yong, R., Qin, J.-B., Huang, M., Du, S.-G., Liu, J., and Hu, G.-J. (2019). An innovative sampling method for determining the scale effect of rock joints. *Rock Mech Rock Eng*, 52(3):935–946. https://doi.org/10.1007/s00603-018-1675-y.

Yong, R., Ye, J., Liang, Q.-F., Huang, M., and Du, S.-G. (2018). Estimation of the joint roughness coefficient (JRC) of rock joints by vector similarity measures. *B Eng Geol Environ*, 77(2):735–749. https://doi.org/10.1007/s10064-016-0947-6.

Chapter 2

On the usability of different optical measuring techniques for joint roughness evaluation

This chapter is a postprint version of the following article, reproduced with permission from Springer Nature:

Marsch, K., Wujanz, D., and Fernandez-Steeger, T. M. (2020). On the usability of different optical measuring techniques for joint roughness evaluation. *Bull Eng Geol Environ*, 79:811–830.
https://doi.org/10.1007/s10064-019-01606-y

Abstract

The roughness of rock discontinuities is an important input parameter for mechanical models of rock masses. To reliably calculate roughness indices, adequate representations of the surfaces are required. Various optical measuring approaches have been applied in the past. However, many studies lack information on resolution and accuracy of the resulting surface meshes. These qualities are yet important, as they explicitly affect the deduced roughness metrics. Often, the sensors do not achieve the given precision and accuracy. Moreover, no technical standards presently exist for roughness evaluation from optical measuring approaches. Therefore, previous studies are difficult to compare. To overcome these issues, this study offers a comparison of four different techniques and sensors. Here, the focus lies on laboratory use and evaluation of micro roughness, meaning samples sizes up to 20 cm in length. Stationary structured light scanning (SLS) serves as the reference method. As results, the surface models from dense image matching are very consistent with the reference. Their calculated roughness values accord to a high degree, both for 2D and 3D indices. In addition, roughness indices deduced from models acquired with manually operated SLS show deviations from the reference yet within an acceptable range. Instead, terrestrial laser scanning turned out to be not suitable for micro-roughness evaluation, at least at laboratory scale. Furthermore, in this contribution, an algorithm is applied, which can retrace all possible profile measurements directly from the triangulated surfaces. That way the ambiguity of the profile-based roughness measure Joint Roughness Coefficient (JRC) is made visible.

2.1 Introduction

The discontinuities within rock masses predominantly define their overall deformational behaviour. Therefore, it is essential to have at least a realistic estimate of their shear strength. Besides the strength of the discontinuity walls and the normal stress, the roughness plays a vital role.

Most empirical shear strength criteria for unfilled discontinuities (e.g. Ladanyi and Archambault, 1970; Barton, 1973; Grasselli and Egger, 2003; Jang and Jang, 2015) incorporate roughness, yet in the form of various parameters. According to the ISRM (1978) and most rock engineering textbooks, roughness should be quantified in terms of Barton's (1973) Joint Roughness Coefficient (JRC). Most commonly, the JRC is determined by visual comparison or, more objectively, by mathematical correlations of surface traces with 10 standard-profiles from a nomographic chart developed by Barton and Choubey (1977). Tactile gauges, and secondarily digital profilometers, are established tools to gather the profiles. However, in this context, the omnipresent issue in engineering geology of characterising an area of interest based on an arbitrarily chosen set of samples also applies. Consequently, different users would sample different profiles on the surface. This leads to notably different results due to the subjective choice and quantity of sampled profiles. Hence, extrapolative effects are inevitable. Instead, 3D models of the discontinuities offer the possibility to overcome this subjectivity as many profiles can be sampled automatically from the data. Also, roughness indices can be computed readily based on the topography of the whole surface.

In past studies, essentially three optical measuring techniques appeared to gather data for roughness evaluation of rock surfaces: (a) laser profilometry, (b) terrestrial laser scanning (TLS), and (c) photogrammetric approaches, such as structured light scanning (SLS) and structure-from-motion (SfM) in conjunction with dense image matching (DIM). In singular cases, other methods were used (e.g. Shadow Profilometry by Maerz et al. (1990)).

In laser profilometry, the travel time of a laser beam is used to measure the height differences along a profile. Typically, a transmitter and receiver unit is fixed to a moveable mount attached to a stationary mechanical positioning system. The frame spans the sample, and height information is gathered as cross-sections of the surface or in a predefined raster. Brown (1995) used a probe with a given measuring point resolution of 25 μm horizontally and 4 μm vertically. Due to limitations in the structure, the uncertainty in height measurement was 20 μm. For example, Belem et al. (2000), Fardin et al. (2001), Jiang et al. (2006) and Ishibashi et al. (2015) used similar devices with comparable technical characteristics in the laboratory on samples of up to 150 mm in length. In order to benefit from the resolution of laser probes in situ and to overcome the difficulties of application in the field, Milne et al. (2009) introduced a portable profilometer specifying the laser spot size to a value of 0.5 mm. Laser profilometers are also used in soil sciences to assess runoff, erosion and retention from surface roughness measurements (Huang et al., 1988). For example, Pardini and Gallart (1998) used a laser profilometer with a resolution of 40–180 μm at a sampling interval of 0.15 mm, being able to scan lengths of a maximum of 1000 mm.

In the past two decades, the use of TLS in earth sciences has increased drastically. In the context of engineering geological questions, TLS is mainly applied for rock mass characterization and rock slope stability assessment (e.g. Kemeny et al., 2006; Sturzenegger and Stead, 2009; Nguyen et al., 2011; Abellán et al., 2014). The number of case studies in which TLS was employed solely for rock surface roughness determination is less exten-

sive. Fardin et al. (2004) used a laser scanner to digitize the surface of spacious rock fractures in situ with an assumed optimal accuracy of 3 to 5 mm. Pollyea and Fairley (2011) used LiDAR-derived data for the introduction of a new roughness parameter. Mah et al. (2013) used a triangulation-based scanner to measure surface heights of a stope in an underground mine. The inference of another roughness measure by Ge et al. (2015) was also built on LiDAR data. No aforementioned author gave information on spatial accuracy. This also applies to the study of Bitenc et al. (2015), who only mentioned the final grid spacing of 1 mm and 5 mm. As for laser profilometry, TLS scanners are also used in soil science for roughness determination. Milenković et al. (2015) showed that TLS data is adequate for roughness evaluation of soil surfaces on scales larger than 5 cm, while below that value, the laser beam footprint affects the accuracy of the model.

Photogrammetry is appreciated as a discontinuity mapping technique already in the suggested methods for the quantitative description of discontinuities (ISRM, 1978). Since then, and especially in the last decade, rapid improvement has been made concerning usability and accuracy. In the past, two different methods, namely SLS and SfM/DIM, have been used, both falling in the domain of photogrammetry but showing marked differences concerning accuracy.

Structured light scanners produce high-quality data which is used, for example, in the industry for quality control of component parts. Despite being portable, the scanners are mostly used indoors due to their sensitivity and limited range. With regard to roughness evaluation of rock, Grasselli et al. (2002) made use of SLS in the laboratory, but only reported the accuracy of the point cloud (being 50 μm on a 150 mm long sample). A similar device was used in successive publications (Tatone and Grasselli, 2009, 2013). More recently, Liu et al. (2017) presented results gathered with a scanner with a precision of 0.025 mm, giving no further information on resolution and the device itself. Instead, Vogler et al. (2017) obtained models with resolutions between 30 and 60 unique vertices per square millimetre of the scanned fracture surface, and reported the accuracy of the device to be between 9 and 27 μm for standardized objects.

Regarding the application of SfM/DIM, Haneberg (2007) used Sirovision commercial software to estimate roughness in terms of JRC from imagery acquired in the field. The model had an average point spacing of 4 cm with a root mean square (RMS) error of 0.6 cm. Kim et al. (2013) and Kim et al. (2015) used the same software. They identified the resolution of the images, and therefore the allowable camera-to-object distance, as a main impact factor on the quality of JRC estimation. Generally, when dealing with data gathered from several meters distance to an outcrop, Sturzenegger and Stead (2009) indicated that because of the resolution of the 3D models, only first-order roughness (waviness) and curvature should be investigated. Bistacchi et al. (2011) used photogrammetric models to determine the roughness of faults on large scale, recording a precision of 5 mm, but not going into detail about accuracy and software used. Also, SfM/DIM has been used in the laboratory to investigate roughness. For example, Wernecke and Marsch (2015) worked with near-distance photographs to evaluate JRC using VisualSFM open-source software . In order to evaluate differences in weathering, Oglesby et al. (2017) applied Agisoft Photoscan software to close-range calibrated imagery and compared 24 profiles with laser profilometry scanning data. Their surface models showed a horizontal resolution of 0.05 mm and a vertical repeatability of 1 μm. They concluded that photogrammetry can be used to assess roughness if the surfaces are more or less continuous and do not incorporate vugs. However, both studies lack information on the accuracy of the resulting profiles. Instead, Nilsson et al. (2012) gave a considerably wide range of accuracy of 0.5 to 1 mm for their surface model.

In order to genuinely measure and accordingly calculate roughness, reliable topographic models of the relevant rock discontinuities are needed. As stated above, many different approaches have been applied, providing obviously different resolutions and accuracy. Therefore, previous studies are also difficult to compare because no technical standards currently exist for roughness evaluation from optical measuring approaches. However, resolution is an important aspect, since the sampling interval has a crucial impact on roughness calculation (e.g. Li and Zhang, 2015). Moreover, previous studies often lack a critical examination of the accuracy of the models used for roughness evaluation. Most importantly, usually only one optical measuring technique or device is used, and the question remains how relevant the resulting topographic models are compared to other studies. As of now, a comparison regarding the applied measuring techniques has not been performed for surfaces under laboratory conditions and sample sizes.

In this contribution, four optical measuring techniques are used for investigation of the influence of data acquisition methods on roughness measures. As the standard procedure for the determination of roughness parameters is to perform direct shear tests in the laboratory (e.g. Barton, 1973; Grasselli and Egger, 2003; Jang and Jang, 2015; Hencher and Richards, 2015), in this paper, the focus is set on laboratory application of the measuring approaches. Hence, the attention is directed towards second-order roughness (unevenness) and especially towards its most used representation – the JRC. Besides the quality assessment of the measuring techniques, the practice to evaluate the 3D nature of surface roughness only by comparison of acquired profiles with Barton's 10 standard profiles is also addressed. In the beginning, short descriptions of the underlying principles of the optical measuring techniques are given. Then, data acquisition and processing as well as the data evaluation procedure are summarised. Subsequently, in the fourth section, the results of the study are presented with a special focus on profile-based JRC determination. After a discussion of the results, the paper closes with a conclusion in the sixth section.

2.2 Background of applied contactless 3D-data acquisition techniques

A distinct yet apparent advantage of contactless methods for 3D-data acquisition over tactile approaches is that no mechanical interaction between a sample and an instruments' gauge is required. As a consequence, sensors from the field of remote sensing can achieve much higher spatial sampling rates in a short amount of time without the necessity of signalisation. Since every sensor has very distinct characteristics in terms of resolution and measurement noise, a short introduction to all applied systems which were used in this study will be given below.

2.2.1 Dense image matching

Dense image matching (DIM) is a methodology to generate 3D point clouds commonly based on uncalibrated imagery, for instance captured by consumer cameras. Uncalibrated means that the interior orientation, respectively the parameters of the camera model, is unknown (Luhmann et al., 2011, pp. 114). For this, the parameters of the interior orientation as well as location and orientation of every photo have to be estimated within a bundle adjustment (Lourakis and Argyros, 2004; Luhmann et al., 2011, pp. 234). Before the bundle adjustment can be performed, information on point correspondences between individual images are required. Therefore, interest points must be extracted,

which are distinct pixel patterns within an image (Luhmann et al., 2011, pp. 380). They are then characterised by using so-called descriptors (Lowe, 2004). After the bundle adjustment, the dense point cloud is computed using DIM, for example, stereo processing by semi-global matching from Hirschmüller (2008). Note that the last required step before geological computations can be performed is to scale the resulting 3D model. To do so, ground control points with known metric coordinates or scale bars within the captured object space are required. Sound summaries on the subject can be found in Haala (2011), Rothermel et al. (2012) or Furukawa and Hernández (2015).

2.2.2 Terrestrial laser scanning

Terrestrial laser scanners (TLS) are active sensors for 3D data acquisition that consist of three major components: an emitter unit in form of a laser diode, a receiver unit, and a deflection unit (Jutzi and Stilla, 2003). The primary output of a laser scan is a point cloud, which consists of a large amount of unsorted points. Apart from geometric information, radiometric data is available for every point, also referred to as intensity (Höfle and Pfeifer, 2007). This information can be used for various processing tasks ranging from registration of point clouds (Böhm and Becker, 2007) to segmentation (Höfle et al., 2007). The essential technology that consequently allowed the development of TLS is the reflectorless rangefinder, which hence can be seen as its key component. In general, two different strategies can be found in TLS rangefinders, namely the phase-shift principle (Vosselman and Maas, 2010, pp. 7) or the time-of-flight methodology (Vosselman and Maas, 2010, pp. 11). The analysis of TLS precision has found much scientific attention over the years, while various influencing factors have been identified, such as the surface reflectivity (Böhler et al., 2003) or the scanning geometry (Soudarissanane et al., 2011). Recent research revealed an inherent relation between signal strength and range noise, which can be used for stochastic modelling or, in other words, to estimate the precision of individual ranges and consequently 3D points within a point cloud (Wujanz et al., 2017). A look at the available scanners on the market shows a huge variety in terms of maximum reach, ranging from several metres (Surphaser, 2017) to several kilometres (Riegl, 2019) and range noise from sub-millimetres (Surphaser, 2017) to centimetres (Riegl, 2019). Hence, different tasks and research questions require different scanners.

2.2.3 Structured light scanning

Structured light scanners (SLS) are active photogrammetric systems that consist of a stereoscopic camera pair and a projector. All components are attached to a mount that physically retains the relative (Luhmann et al., 2011, pp. 216) and the absolute orientation (Luhmann et al., 2011, pp. 227) of the system. Before metric measurements can be carried out, a calibration routine has to be completed that determines all unknown orientation parameters (Luhmann et al., 2011, pp. 266). Metric information is usually embodied in form of a calibration plate that includes coded targets (Luhmann et al., 2011, pp. 184). A vital requirement for photogrammetric measurements is sufficient contrast within the recorded imagery that is, for instance, biased by the given lighting conditions and/or the object's radiometric properties. In order to provide contrast even under poor conditions, the projector of the system projects a fringe pattern onto the object of interest. In general, two different strategies can be distinguished: static and dynamic fringe projections (Luhmann et al., 2011, pp. 426). The original result of a measurement with a structured-light scanner is a point cloud, yet usually without radiometric information.

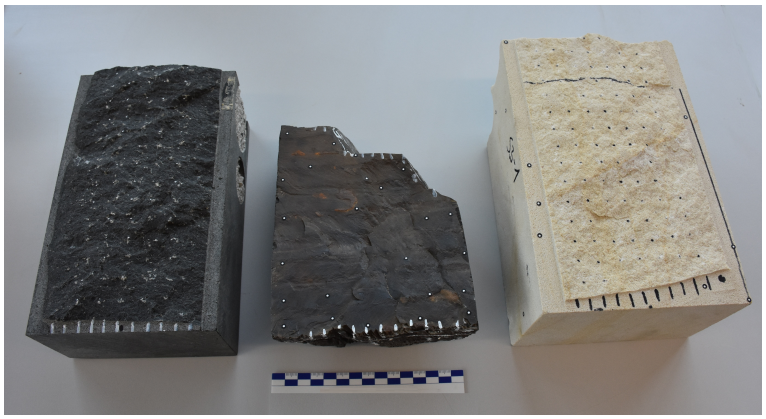

Figure 2.1: Rock samples; left to right B (basalt), M (schist), and S (sandstone); length of scale bar 15 cm

Since topological relationships are known for all pixels in the sensor's matrices, triangular meshes can be easily exported.

2.3 Materials and methods

2.3.1 Rock samples

When comparing different data acquisition methods among each other it is effectively insignificant which exact rock is used. Simply, it has to be taken care that the same unmodified sample is scanned with all methods in question under similar conditions. Nevertheless, rock samples with different degrees of roughness are desirable in order to gather results which are meaningful for a broad spectrum of naturally occurring rock surfaces. In this study, three different rocks were used, namely basalt with a rough stepped appearance (sample B), schist showing a smooth planar surface (sample M), and medium-grained sandstone (sample S) having a rough undulating surface. The three samples, shown in Figure 2.1, were used in order to reflect three typical roughness types as mentioned in ISRM (1978). The white respectively black markers at the lower end of the samples mark the starting points for tactile profile gauge measurements. The subareas of the samples which were used for later roughness evaluation ranged between 140 cm² and 210 cm² with widths of roughly 10 cm and lengths between 14 and 21 cm.

2.3.2 Conventional tactile measurements

The most widely used device to gather topographic information of joint profiles, especially in engineering practice, is a profile gauge (or sometimes referred to as Barton comb). Its popularity can be explained by the ease of use and straightforward application. The device consists of aligned round metal pins which are pressed onto the surface in question. Problems evolve since the freely moving pins do not assure a constant sampling interval and, due to the step-wise sampling method, introduce a band pass filter to the data (Reeves, 1985). However, the latter is a problem with all measuring procedures. Additionally, Gao and Wong (2015) showed how manual tracing of the profiles add human error especially with low-roughness profiles. This can be compensated partially by using automatic data extraction methods, e.g. introduced by Alameda-Hernández et al. (2014), still leaving behind the problem of filtering and low resolution of only

1 mm. Moreover, the measurement is not repeatable. On one hand, it cannot be ensured through manual application that the gauge is again located on the same spot on the surface, and on the other hand, with this procedure the surface is not archivable. However, profile gauge measurements were performed in this study for comparative purposes, as it is an established manual methodology. A profilometer with a pin diameter of 1 mm was used, which in turn results in a maximum resolution of 1 mm. The profiles were manually traced and digitised using scaled paper collecting height information at the middle of each pin. On every sample surface, profiles were captured with an approximate spacing of 10 mm. A total of 30 profiles was evaluated, 10 per sample.

2.3.3 Data acquisition and preparation

The sensors used in this study were chosen according to devices and methods used in previous studies, as mentioned in the introduction. The goal was to reproduce previous measuring setups as good as possible with similar devices accessible to the authors. This approach might inflict problems on comparability; however, it seems reasonable, since in this study the methods are compared among one another. Moreover, no standard devices and recommended procedures or suggested methods for roughness evaluation based on optically derived data sets exist which could have been applied and followed.

Data acquisition has been carried out under laboratory conditions with no direct exposure to sunlight that may bias the results of the optical sensors. The applied TLS was a FARO Focus3D X 330 HDR with a specified reach of 330 m, an angular resolution of 0.009°, and a rangefinder precision of 0.4 mm for an assumed albedo of 10% (for manufacturer datasheet see FARO, 2019). Two structured light scanners, the stationary GOM ATOS I and the handheld Artec Eva, were deployed. The ATOS allows one to capture 3D-information in a volume that spans 125 x 100 x 100 mm^3, yielding a lateral resolution of 0.12 mm for a single scan (GOM, 2019). Since the samples have been redundantly recorded, i.e. from various perspectives, a higher resolution can be expected on the surface of the object. As stated in the technical specifications (see Artec, 2019), the Eva handheld scanner allows one to acquire data with a spatial resolution of up to 0.5 mm with a specified 3D accuracy of 0.1 mm. The sensor is applicable in a working range between 0.4 and 1 m. Since both SLS scanners were moved around the object, the resultant models were captured with multiple directions of observation. On one hand, this increases the resolution; on the other hand, scanning shadows are avoided, as peaks and valleys are observed from different sides.

While the sensors mentioned above provide metric data, DIM in fact allows one to generate 3D information, yet not up to scale. Hence, it is of vital importance to determine a scaling factor that transforms the generated 3D model into a metric representation. This step systematically influences the quality of the outcomes. It must be rated as the most critical step in the processing chain. In order to tackle this issue, a lightweight, low-cost, precise and portable norm was manufactured (Figure 2.2). It enables reliable computing of scale information in three cardinal directions. In this case, the shape of the norm was chosen to conform to the shape of the samples. The norm consists of a frame fabricated of carbon fibre tubes that are insensitive to thermal variations due to their low coefficient of expansion – an aspect that is important for prospective field work in case notable changes in temperature occur. Twelve spherical markers are attached to the tubes and serve as spatial reference points. In order to assign metric information to each sphere's centre, 3D coordinates have been measured with the GOM ATOS scanner at high precision better than 0.01 mm (Marsch and Wujanz, 2016). The transformation parameters, including a scaling factor between the DIM data and the SLS data, are computed by determining cor-

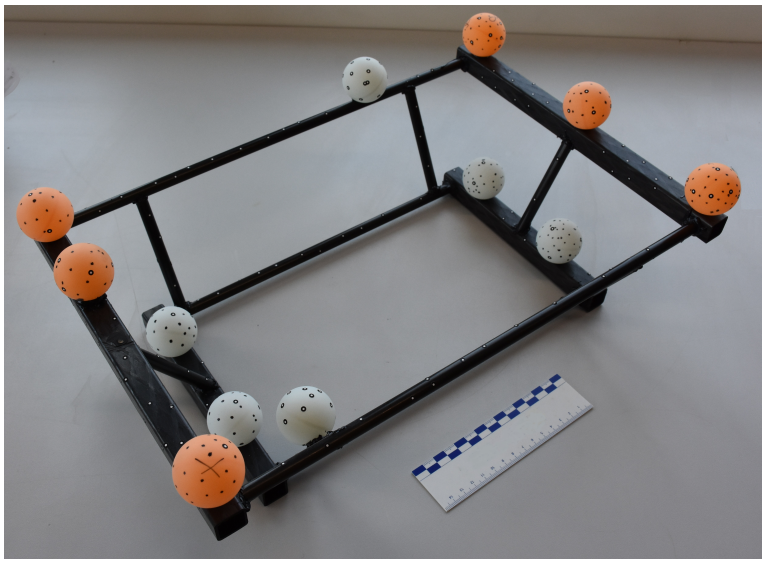

Figure 2.2: Portable norm for defining scale with DIM (length of scale bar 15 cm)

respondences between the according centre points of the spherical markers with JAG3D software (JAG3D, 2018). The spatial residuals of the 12 spherical marker points were computed to an average of 0.7 mm. Between 30 and 50 photographs were taken of each sample using a Nikon D800 digital camera. It has a 36-megapixel sensor, and a Nikon Nikkor AF-S 24-70 mm/2.8 lens fixed at 24 mm was employed. The resulting imagery was saved in JPG format at the lowest compression rate. First, the camera was moved around the object in two rings at different angles of view to adequately capture the rock sample with the norm. Secondly, the camera was positioned randomly at near distances to the sample to produce high-resolution images of the surface in question.

To produce the DIM models, SURE software (Rothermel et al., 2012) was applied to the uncalibrated images. Processing of the other datasets captured by the remaining sensors was done using the provided software packages with default settings of the corresponding manufacturer. If the devices ought to be used, there is no way out of this dilemma as the machines are integrated commercial systems. Yet, this rather uncritical use of the devices and software, which also occurred in many past studies, leads to uncertainty regarding the quality of the surface models. Due to intellectual property rights, all used devices and software are essentially black boxes. This means that neither it is comprehensible how noise and outliers are dealt with nor how the surface meshes are constructed from the captured point clouds. The models must be taken as they are without any possibility of calculation of errors. However, to raise awareness of these issues, the influence of surface reconstruction algorithms on roughness evaluation will be addressed briefly later on. Naturally, different measuring approaches and processing routines produce different models. Consequently, different roughness values are calculated. It has to be pointed out with great emphasis that in this contribution, because the principles of operation of the provided software (!) are unknown, the focus is set on the usability of the different technical packages for roughness evaluation and their capabilities as tools for engineering geological research questions in this field. It is beyond the scope of this paper to analyse the methods from a metrology point of view.

2.3.4 Calculation of roughness indices

There are two approaches to define roughness indices: considering profiles or considering surfaces. Using profiles is most popular, although it fails the 3D problem of shear resistance. Instead, definitions of 3D indices are available. The indices used in this study are depicted below.

Measures describing roughness in terms of profiles are generally derived based on statistical or fractal approaches. The statistical approaches predominantly focus on height differences between adjacent data points. The RMS of the first derivative of the profile, termed Z_2 (Myers, 1962), is one of the classic indices for roughness evaluation. It is a widespread roughness index in rock mechanics. Z_2 is defined as follows:

$$Z_2 = \sqrt{\frac{1}{L}\int_0^L \left(\frac{dy}{dx}\right)^2 dx} \approx \sqrt{\frac{1}{L}\sum_{i=1}^{n-1}\frac{(y_{i+1}-y_i)^2}{\Delta x}} \tag{2.1}$$

In Equation 2.1, L is the length of the profile, and dy is the height difference over a certain constant horizontal interval dx. In contrast, the fractal dimension D gives a numeric value representing the deviation of a profile from a straight line. Typically, the compass-walking or box-counting methods are employed. The total length of the profile, respectively, the number of boxes needed to cover the profile, are plotted in log-log-space versus the varying compass radii, respectively, box sizes. The slope of the linear fit yields the fractal dimension D.

The literature is abound with correlations of Z_2 and D with JRC; for an overview see Li and Zhang (2015) and Li and Huang (2015). However, the differences between most of the contemporary compared to older correlations are marginal. In this study, with regard to Z_2, the correlation from Yu and Vayssade (1991), which is valid for 1-mm sampling intervals, was used:

$$\text{JRC} = 64.22 \cdot Z_2 - 2.31 \tag{2.2}$$

To determine the fractal dimension D, the compass-walking method was used. Within this technique, the length of a profile is approximated by a chain of circles in which the circles originate at the intersection of the previous circle with the profile. The procedure is repeated with various radii that result in different numbers of circles needed to cover the profile. The radii are then plotted in log-log space against the number of circles needed. The slope of the linear fit to the data yields the fractal dimension D. According to Li and Huang (2015), compass-walking is more closely related to JRC than box-counting and geostatistical methods (h-L method). JRC was calculated from D according to the correlation from Lee et al. (1990) as follows:

$$\text{JRC} = -0.87804 + 37.7844 \cdot \left(\frac{D-1}{0.015}\right) - 16.9304 \cdot \left(\frac{D-1}{0.015}\right)^2 \tag{2.3}$$

Focusing on 3D roughness indices, which take the whole surface into account, in this study, two definitions were used. The so-called surface roughness coefficient R_S by Lange et al. (1993) is defined as the ratio between the actual surface area, A_t, and the surface area projected onto the xy plane, A_n ($R_S = A_t/A_n$). Alternatively, the roughness measure from Grasselli et al. (2002) is rather a set of parameters. It is defined by the following equation:

$$A_{\theta^*} = A_0 \left(\frac{\theta^*_{max} - \theta^*}{\theta^*_{max}}\right)^C \tag{2.4}$$

Here, essentially all parts of the surface that face the shear direction and lie under certain threshold dip values θ^* are identified successively, each termed A_{θ^*}. Then, a power law function with the parameters θ^*_{max}, A_0 and C is fitted to the data. These three parameters describe the roughness of the surface in question with regard to a specific shear direction. Also, JRC can be calculated from the parameter set, although, the coefficient of correlation is low. Besides, additional mechanical properties of the surface must be considered (Grasselli and Egger, 2003).

2.3.5 Post-processing for variability assessment of profile measurements

In order to evaluate the differences between the optical measurement techniques in terms of roughness indices, in this study, an algorithm for the analysis of the 3D data was implemented in Matlab, which made it possible to emulate all possible profile measurements of 10 cm length. On one hand, through capturing all possible profiles, the subjectiveness of placement is overcome. On the other hand, considering only 10-cm-long profiles is a requisite, as the standard-profiles on the nomographic chart from Barton and Choubey (1977) are also of 10 cm length. This requisite originates from scale effects shown by Bandis et al. (1981). Consequently, in a successive publication from Barton and Bandis (1982), a correction function was introduced which adjusts JRC determined from profiles deviating from the standard length. Therefore, in order to eliminate scaling issues, only standard-length profiles are meaningful when JRC are to be calculated using one of the plenty available correlations since they are all based on Barton and Choubey's (1977) standard profiles.

As basis for the calculations, the triangulated surface meshes are imported as ply files in ASCII format. For the subsequent analysis, it was convenient to move the meshes to positive values in a Cartesian coordinate system. Furthermore, the surfaces were aligned according to best-fit planes that run parallel to the xy plane.

In order to calculate 2D roughness indices, first, profiles have to be extracted from the models. To do so, arbitrary planes with user-defined spacing and orientation are assembled, which serve as cutting planes. Then, all triangles are identified that cross the cutting planes. To receive the traces of the planes on the surface, the intersection points of each triangle edge with the planes are calculated. This is fundamentally different to other studies as the data is not transformed onto a regular grid (e.g. Vogler et al., 2017). That way, a step of interpolation is avoided which usually tampers with the actual outcome of the optical measurements. The cutting planes can be arranged in space randomly so investigation of anisotropy is also possible.

Second, the overall slopes of the profiles are identified via linear least squares regression. Then, the profiles are rotated according to these slopes so that the regression lines run parallel to a constant horizontal axis. Additionally, height information is interpolated linearly in a predefined sampling interval. These steps are necessary since the statistical parameters used rely on height differences or slopes between adjacent points over a constant sampling interval. Therefore, a datum line must be defined. Barton and Choubey's (1977) standard profiles were recorded with a profile gauge of 1-mm sampling steps. Common sense would suggest using the same sampling interval, since the data used and the original data on which the JRC concept was founded should be coherent. Frankly, interpolating data below 1 mm is useless and does not introduce more information. Moreover, it may cause errors as the calculation of the JRC is sensitive to the sampling interval (see e.g. Yu and Vayssade, 1991). That is why, in this study, an identical sampling interval was employed.

The 3D roughness indices are calculated readily from the imported surface meshes. This is possible provided that the surfaces have been already aligned according to best-fit planes. As the same as for the profiles, alignment is necessary since the roughness indices used refer to the xy plane as the datum.

The great benefit of the algorithm described above is its capability of automatically extracting all possible 10-cm profiles from the data set. This procedure corresponds to moving a profilometer over the surface, just like applying an imaginary profile gauge, yet it results in a drastically larger amount of sampled profiles. The improvement consists in the possibility of statistical analysis of the calculated profile-based JRC. Also, by doing so, the influence of scale on the outcome can be assessed.

2.4 Results

In the following section, the results are presented. As stationary SLS scanners are industry standard, their data serves as the reference for comparing the other techniques. The differing optical measuring techniques, respectively the sensors, are abbreviated as follows: GOM ATOS stationary structured light scanner = stat.SLS; FARO Focus3D terrestrial laser scanner = TLS; Artec Eva handheld structured light scanner = hand.SLS; photogrammetric dense image matching = DIM.

2.4.1 Comparison of all applied optical measuring techniques

For roughness index calculation, reliable topographic models of the discontinuities are needed. As there exists no technical standard regarding contactless optical roughness measurement, it is important to assess the different approaches. Vital characteristics of the aforementioned 3D sensors are the accuracy, respectively, the precision of the captured data, as well as achievable resolution. It must be emphasised that the resulting spatial resolution (spt) in object space of a data set is directly correlated to the survey configuration. The published data sheets usually only specify the resolution of elementary observations, respectively, the ones of individual sensor components. Hence, it is not a trivial task to estimate the resulting precision and resolution of a recorded outcome! In most past studies (see the Introduction), only the theoretical resolutions and accuracies were reported. As for TLS, resolution and precision are individually specified for angles, which influence the lateral (ltl) sampling, as well as for ranges, that impact the longitudinal (lgl) components. Apart from these specified parameters, the size of the laser beam has a crucial influence on the resulting resolution (Böhler et al., 2003). In the case of photogrammetric data acquisition, the resolution of the outcome is mostly influenced by the pixel size of the image sensor as well as the image scale.

In Table 2.1 crucial characteristics of the sensors under investigation are summarised. In the first column, where applicable, the achievable resolution is given according to the data sheets of the manufacturers. The values in the second and third columns have been experimentally derived by capturing a test panel with a specified planarity below 0.06 mm. Using such a geometrically simple object assures comparability of the outcomes. The numbers for the resolution in the second column were derived from the projection of the points onto the xy plane. Based on the acquired points on the panel's surface, a plane has been approximated while the RMS of residuals, which is a measure of the spatial precision, is reported in the third column. The stationary SLS scanner features the highest value in terms of precision. For hand.SLS and DIM, the precision is in the same order of magnitude, whereas TLS yields values two orders lower than stat.SLS.

Table 2.1: Different sensors for 3D-data acquisition of a planar test surface ($^{(+)}$ GOM (2019), $^{(\#)}$ Artec (2019), $^{(\sim)}$ FARO (2019))

	Specified Resolution	**Exp. resolution planar** $[pts/mm^2]$	**Exp. spatial precision** $[mm]$	**Pot. field use**	**Metric scaling**
stat.SLS	0.07–0.5 mm (spt)$^{(+)}$	0.59	0.009	-	yes
hand.SLS	0.5 mm (spt)$^{(\#)}$	0.84	0.014	+	yes
DIM	-	1.01	0.035	+	no
TLS	0.009° (ltl)$^{(\sim)}$ 0.1 mm (lgl)$^{(\sim)}$	1.76	0.476	o	yes

Concerning resolution, for this specific example of a planar test panel, TLS provides the highest value. Upon evaluating the precision and resolution, it has to be kept in mind that the point clouds from stat.SLS, hand.SLS, and DIM are more or less calculated from digital imagery. During calculation within semi-global matching techniques, changes of adjacent disparities are penalised based on smoothness constraints (Hirschmüller, 2005). Therefore, depending on the implemented settings and threshold values, during processing, an unknown amount of points may be removed from or interpolated within the point cloud, affecting directly the resolution of the outcome. That way, the resolution in the output and the given maximum possible resolution of the device are not necessarily coherent.

Apart from the metric entries in Table 2.1, potential field use in remote areas is also briefly assessed in terms of difficult (-), pros and cons (o) and feasibility (+) for second-order roughness evaluation. A disadvantage of stat.SLS systems is their asset cost and the restricted portability (sensitivity, power supply, required space on slope, etc.). The latter downside does not apply to handheld systems that are quite easy to transport, yet at the cost of a slightly lower precision. TLS are very versatile sensors in terms of range, yet they also feature the largest noise and lowest resolution since the laser spot size usually sums up to several millimetres in the field when used on large distances, which affects the deduced roughness values (see e.g. Sturzenegger and Stead, 2009). When it comes to versatility, cost, and portability, cameras in combination with DIM appear to be an interesting alternative to the other established systems. However, the generated outcomes are not metric. Hence, the question arises, if there is an alternative way to introduce metric information into the object space during data acquisition apart from using artificial markers and total stations (Luhmann et al., 2011, pp. 479), which would add to the amount of equipment that has to be brought to the field.

As mentioned above, earlier research often lack information on precision and resolution of the applied measuring approaches in real measuring environments and scanning some random object. Therefore, the listed values in Table 2.1 offer, for the first time, a comparison of the different optical measuring techniques in the context of roughness evaluation. Nonetheless, the numbers are valid for the example of a planar test panel. After all, direct geometrical comparison of different geometric descriptions of the same rock object is practically impossible since it is exceedingly unlikely that the same exact relief points on the surface are captured with each and every measuring device. Therefore, perfectly aligned scans from differing measuring techniques are unattainable. This problem can only be addressed by statistical analysis of derived roughness parameters

as described later on.

Despite the difficulty mentioned before, an overall trend concerning the similarity of the variably measured topographic models can be visualised with the help of 3D deviations calculated according to Cignoni et al. (1998). To do so, all data sets of the particular rock sample were transformed in the specific referential coordinate system provided by the stationary SLS scanner. The computation of transformation parameters was done by usage of spherical markers in case of DIM as well as iterative closest point search (ICP) (Wujanz, 2012) in the cases of hand.SLS and TLS. The 3D deviations for DIM, hand.SLS, and TLS from the referential stationary SLS are exemplified in Figures 2.3, 2.4 and 2.5 for sample B. The best accordance is seen for DIM in Figure 2.3. For the majority of the surface, the spatial deviation is within 0.1 mm. Except for the edges, the deviations do not exceed 0.3 mm. The standard deviation amounts to 0.078 mm. For the hand.SLS data, the deviations are larger, as depicted in Figure 2.4. Nonetheless, most parts do not deviate more than 0.2 mm from the reference surface with a standard deviation of 0.115 mm. Instead, in Figure 2.5, huge differences between the reference and TLS are visible (note the rescaled colour bar). The majority of the surface deviates more than 0.35 mm. The standard deviation of 0.409 mm reflects the large discrepancy between the data sets. In order to obtain a colour bar similar to Figures 2.3 and 2.4, in 2.5 marginal areas that deviate more than ± 0.68 mm are depicted in grey. Unlike the results for the planar test panel, DIM outperforms hand.SLS, not only concerning the deviation from the reference, but also regarding resolution. The reference is comprised of the largest amount of points, followed by DIM with a small gap. However, huge differences are obtained for hand.SLS and TLS. These models show a resolution one order lower than the reference. The resultant experimental resolutions for the three different rock samples are listed in Table 2.2. The resolutions were calculated by projecting all points onto the xy plane parallel to the best-fit plane. The low resolution for sample M using DIM is caused by smoothness constraints in the matching algorithms, as explained earlier for the planar test surface. Since sample M is also relatively smooth compared to the other samples, the algorithms tend to thin out the point cloud. Note that the bracketed values for the standard spatial deviation for sample B in Table 2.2 apply for the case of considering the whole surface (as discussed above and visualised in Figures 2.3, 2.4 and 2.5). However, neither the edges nor the regions which were covered by control points were used for the subsequent quantitative analyses of roughness measures, because these parts cause large deviations (due to edge effects). Therefore, the models were trimmed, and the non-bracketed values in Table 2.2 refer to that case. Apart from TLS which yields comparatively low resolution and high spatial deviations throughout, at first glance, DIM and hand.SLS give similarly accurate models (max. difference 50 μm), yet with different resolutions. From this rather simple geometrical comparison, one might conclude that both methods would arrive also at similar roughness values. A sound analysis is given in subsection 2.4.2.

The differences between the measuring approaches are equally evident when profiles are compared. In Figure 2.6 the same profile, which was taken from sample B, is shown as a function of the applied measuring technique. For hand.SLS and TLS, the profiles are smoother compared to the reference. Additionally, stat.SLS and DIM yield more survey points, on average 19.05 pts/mm and 15.99 pts/mm, respectively, for this example. With the hand.SLS 6.05 pts/mm are attained. This exceeds the manufacturer's declaration of a lateral resolution of 2 pts/mm due to multiple acquisitions of the surface from various perspectives. For the TLS sample, a mean of 4.27 points per millimetre is calculated. More important, the smoothness of the profiles in case of hand.SLS and TLS

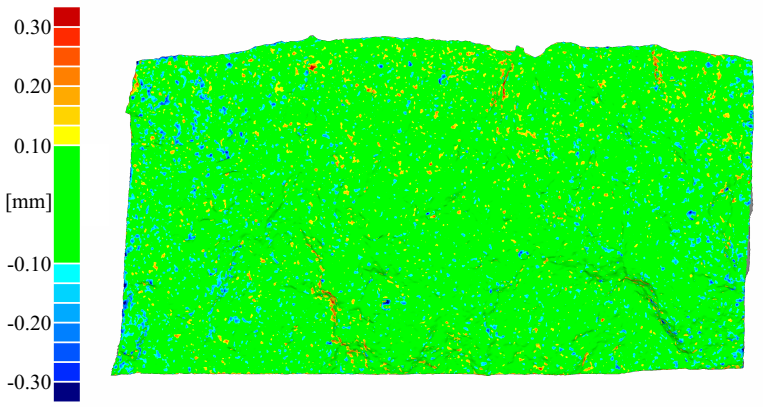

Figure 2.3: Spatial deviation for DIM from the reference, sample B

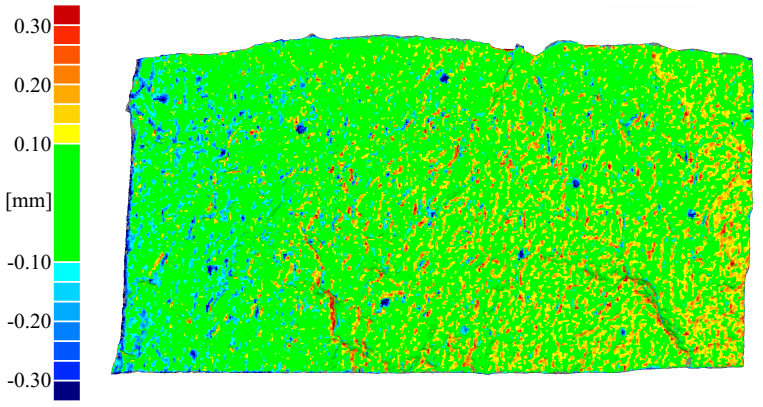

Figure 2.4: Spatial deviation for hand.SLS from the reference, sample B

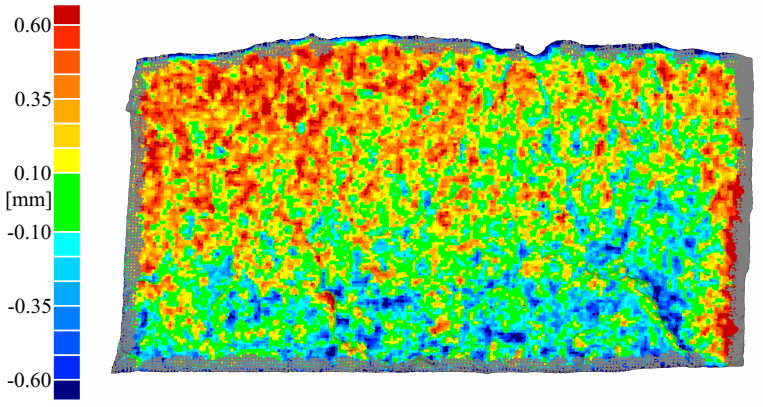

Figure 2.5: Spatial deviation for TLS from the reference, sample B

Table 2.2: Resolution and spatial deviation of the sensors for all samples (last three columns: bracketed numbers considering whole surface, non-bracketed values valid for trimmed surfaces to reduce edge effects)

Sample	**Experimental resolution** $[pts/mm^2]$				**Standard spatial deviation** $[mm]$		
	stat.SLS	DIM	hand.SLS	TLS	DIM	hand.SLS	TLS
B	18.58	15.15	2.22	1.17	(0.078) 0.117	(0.115) 0.096	(0.409) 0.225
S	14.71	8.90	2.45	1.22	0.081	0.096	0.568
M	2.59	0.51	4.04	1.17	0.134	0.078	0.322

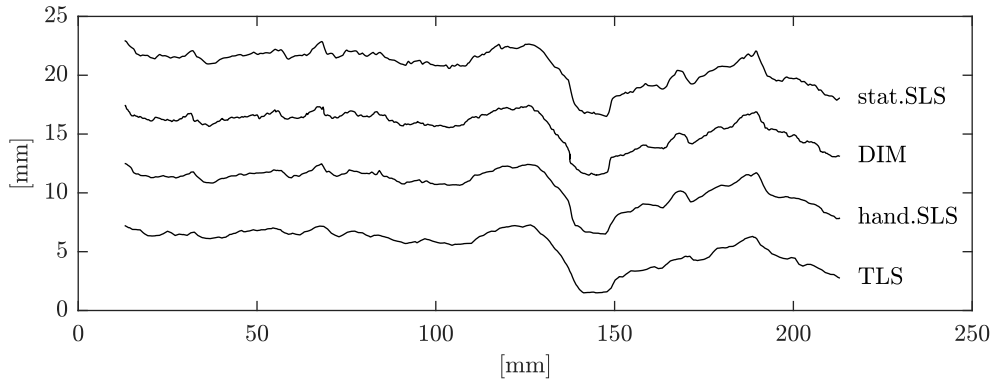

Figure 2.6: Comparison of profiles

is also copied to profiles of fixed sampling interval. This is crucial as they are later used for roughness calculation. In summary, lower resolution and less detail come to the fore on comparison of hand.SLS and TLS with the reference.

2.4.2 Implications for JRC

According to the original concept of JRC from Barton (1973), profiles can serve as characterisations of surfaces. This concept seems reasonable in the light of insufficiencies of historical measuring devices. However, it introduces random errors unfeasible to quantify. Obviously, the location of the point of origin on the surface and the direction is set arbitrarily by the specific user. Usually, in practice, no automated data acquisition and processing is used, which limits the amount of measurements drastically. As a result, assigning one roughness index to a surface, based on one or a few profile measurements only, is exceedingly subjective. Moreover, as mentioned earlier, JRC calculation should be carried out using profiles strictly of 10-cm length since all calculation methods depend on the 10 type traces from Barton and Choubey (1977) which are indeed only 10 cm long.

One problem this necessity evokes is exemplified by picking a random profile from sample B, as depicted in Figure 2.7. Here, the cutting plane (see subsection 2.3.5) is also shown. The corresponding extracted profile over the whole length of the surface is displayed at the bottom in Figure 2.8. Additionally, the standard-length profiles yielding the lowest, a mean, and the highest JRC (based on Z_2) are given. Depending on where the standard-length profiles originate on the horizontal axis, JRC of maximal 17.1, mean 14.4

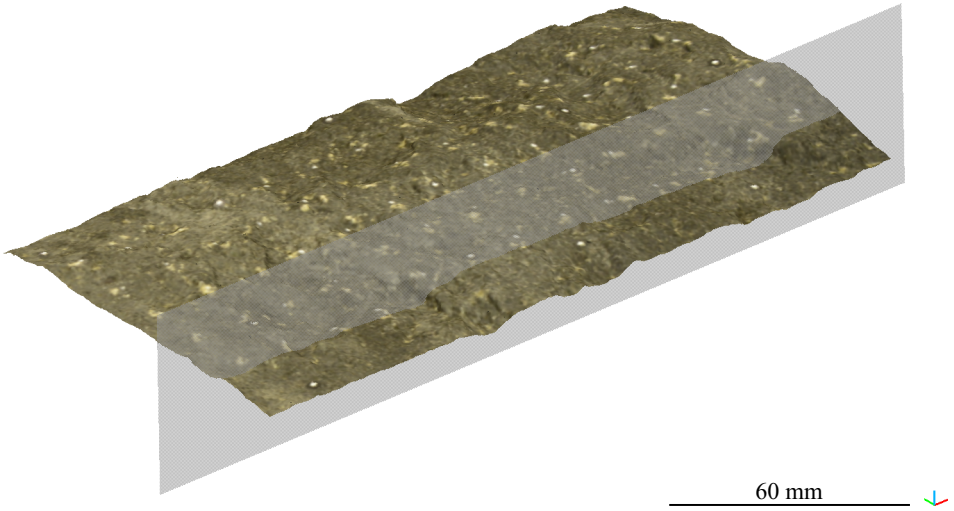

Figure 2.7: Example cutting plane on sample B (captured with DIM)

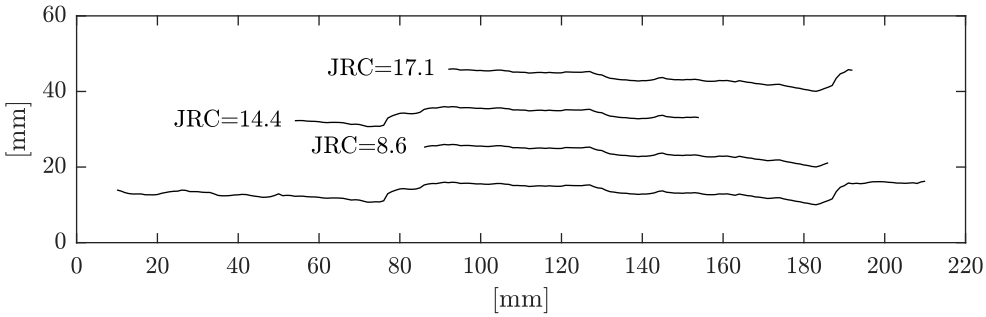

Figure 2.8: Example profile from sample B with lowest, mean and highest standard-length JRC

and minimal 8.6 result. Thus, a large bandwidth of 8.5 JRC units is received. Defining a representative JRC already for this particular profile, based on topographic information only, seems practically impossible.

This problem is gaining even more importance when the whole surface is considered. The surficial variability of the roughness coefficient is represented in Figure 2.9. In this study, profiles were extracted from the surface with a 1-mm x 1-mm raster for the profile starting points. The heat map displays all profile origins color-coded according to their JRC value (direction of analysis is parallel to the x-axis). Profiles incorporating sections of steep micro-relief and abrupt steps show higher values and are marked in red. However, most parts of the surface yield JRC in the range of 10 to 12, which are displayed in green and yellow. Clearly, a unique exact JRC does not exist since ambiguous results are achieved. Nevertheless, by means of the implemented processing steps, all possible tactile profile gauge measurements are virtually executed and ready to be utilised for statistical analysis. That way the randomness of sampling origins can be overcome.

In order to evaluate all possible profiles, not only visually as in Figure 2.9, histograms are assembled. In Figures 2.10, 2.11 and 2.12 the histograms of JRC are displayed for the

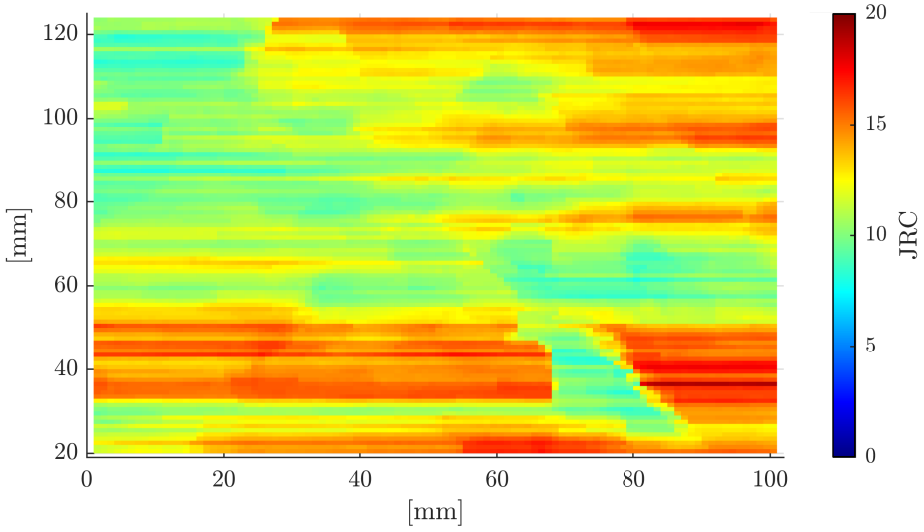

Figure 2.9: Surficial variability of JRC for sample B

four optical measuring techniques and the particular samples as a function of the calculation approach (namely, based on the statistical parameter Z_2 (left side) and based on the fractal dimension D (right side) as explained in subsection 2.3.4). For sample B, stat.SLS leads to the highest mean JRC for both calculation approaches amongst all measuring techniques. The histograms for the DIM model (Figure 2.10, b) and f)) are similar to those of the referential stat.SLS. However, the mean JRC are 0.7 units and 0.9 units lower. Nevertheless, the shapes of the distributions are in close agreement, which is reflected in similar standard deviations and ranges. On the contrary, for hand.SLS a shift of the mean JRC to the left in amounts of 1.8 and 2.2 units occurs compared to the reference (Figure 2.10, c) and g)). This is even more significant for TLS (Figure 2.10, d) and h)) where a drop to a totally different JRC class is seen. Not only are the mean JRC much lower, but the shapes of the distributions also change. Considering both calculation methods and the three optical measuring approaches that are to be compared to the reference, the most pronounced change follows for JRC based on D and derived from TLS data (Figure 2.10, h)). While the distribution for stat.SLS resembles a log-normal distribution, here the JRC seems to be normally distributed around a much lower mean value.

In Figures 2.11 and 2.12, the histograms of JRC for sample S and sample M are shown. Of paramount importance for both samples are the discrepancies concerning hand.SLS and TLS with regard to the reference. For the sandstone sample S, TLS yields considerably higher JRC than all other methods. This could be due to the large noise because of the radiometric properties of the surface (bright colour and penetrable quartz grains), which notably bias the results generated by TLS (Wujanz et al., 2017). On the contrary, for sample M (schist), TLS is in good agreement with the other techniques. This might be because the schist sample is quite smooth. That way, the lower lateral resolution of the TLS scanner is concealed as the asperity differences are small over great portions of the surface. Instead, for hand.SLS, the drop of approximately three JRC units for the sandstone sample S is rather large. After all, for the schist sample, the agreement with the other methods is good. Taking all three samples into account, no clear relationship with the reference can be drawn. As a result, there exist no universal shifts such as roughness values from hand.SLS or TLS being systematically lower or higher than

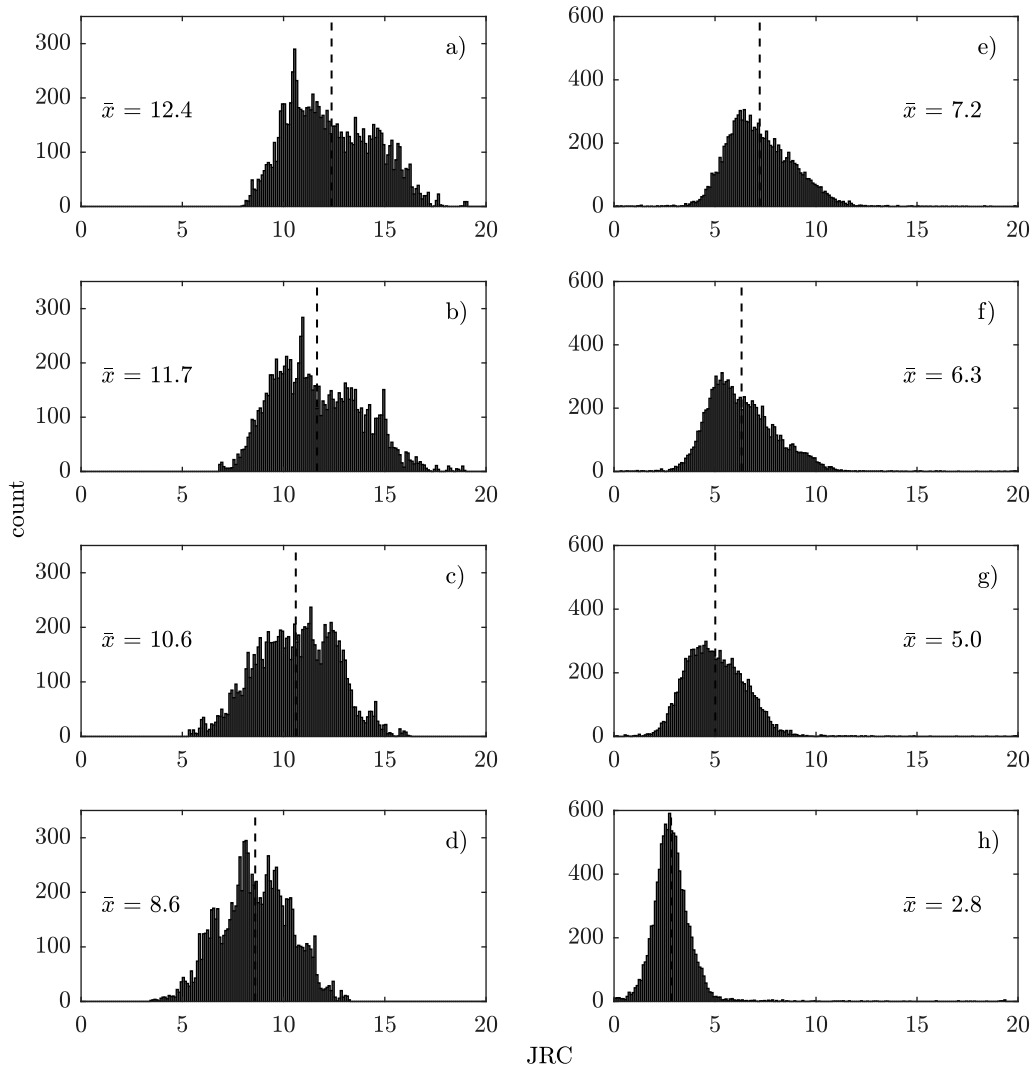

Figure 2.10: JRC histograms sample B – a),b),c),d) based on Z_2; e),f),g),h) based on D – reference a),e); DIM b),f); hand.SLS c),g); TLS d),h)

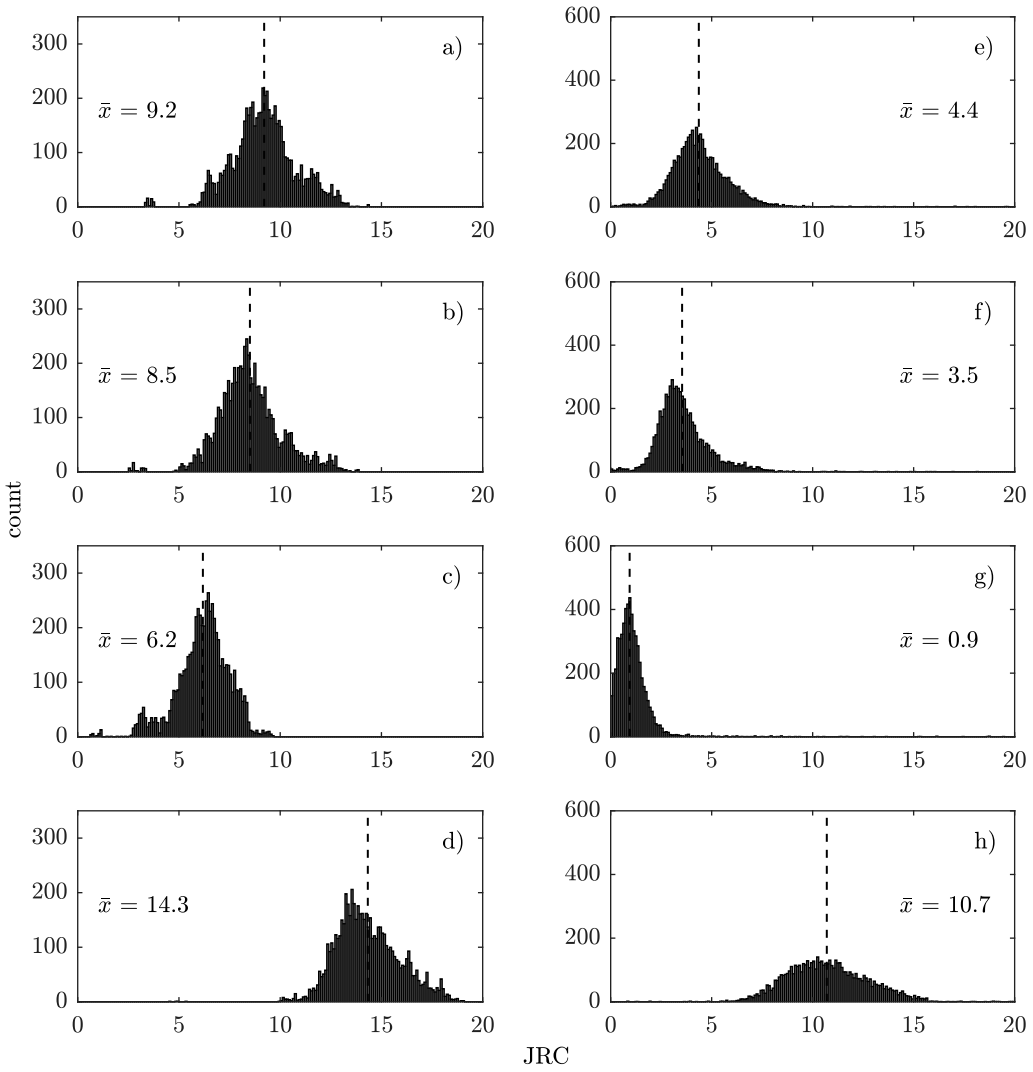

Figure 2.11: JRC histograms sample S – a),b),c),d) based on Z_2; e),f),g),h) based on D – reference a),e); DIM b),f); hand.SLS c),g); TLS d),h)

values derived from the reference data. Consequently, JRC inferred from hand.SLS or TLS data are inconclusive as the geometric information from these optical measuring approaches depends heavily on the surface texture. On the opposite, DIM agrees well with the reference for all samples showing similar mean JRC and similar distributions.

Another interesting result concerns the calculation routines for JRC. The values calculated based on the fractal dimension D are systematically lower than the values derived based on Z_2. Both calculation approaches should lead to the same JRC as they are derived from Barton and Choubey's (1977) standard profiles. However, this is clearly not the case. One reason for the obtained discrepancies might lie in the data source for the correlation functions. Lee et al. (1990) as well as Yu and Vayssade (1991) digitised the standard profiles yet in different ways with regard to accuracy and resolution. Additionally, their correlations were established solely based on the standard profiles. Instead, in this study, original surface scans were evaluated. In conclusion, JRC calculated from Z_2 according to Yu and Vayssade (1991) are not interchangeable with JRC calculated from D according to Lee et al. (1990) for none-standard profiles.

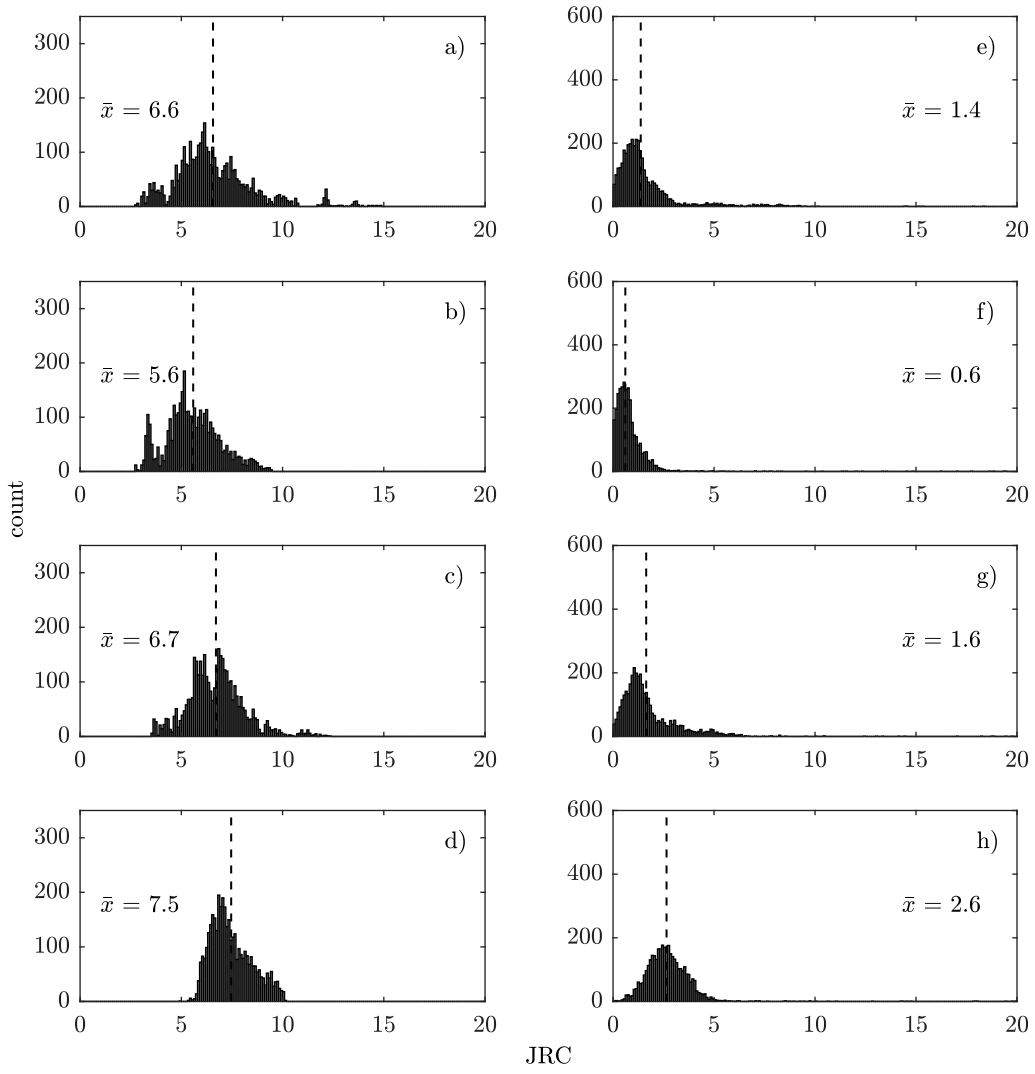

Figure 2.12: JRC histograms sample M – a),b),c),d) based on Z_2; e),f),g),h) based on D – reference a),e); DIM b),f); hand.SLS c),g); TLS d),h)

2.4.3 Influence of surface reconstruction

As mentioned earlier, all software packages used in this study to acquire and process the data are inaccessible to a deeper study of the surface reconstruction algorithms. Therefore, it is unclear how watertight and smooth meshes are constructed from partially very noisy data. Especially with hand.SLS, huge differences between the initial point cloud and the final mesh occurred. However, since the post-processing routine established for this study relies on the surface meshes, it is useful to address the influence of surface reconstruction from point clouds onto engineering geological roughness measures. For this purpose, the screened Poisson surface reconstruction algorithm developed by Kazhdan and Hoppe (2013) with different sets of controlling parameters is used. Examples are illustrated in Figure 2.13. In the top row, the original data from stat.SLS is shown. For the outcomes in the middle and bottom rows, the octree depth d was decreased, and the minimum number of sample points per node as well as the screening parameter α were increased. Although the input point cloud for all three surfaces is the same, the representations become smoother depending on the parameters of the reconstruction algorithm. Consequently, different distributions of JRC are calculated. A shift is seen towards lower JRC. Obviously, the surface gets gradually smoother. Note that the differences are only within one JRC class because the input data in this case was acquired with low noise stat.SLS. When more noisier data is used, the importance of the reconstruction becomes larger. In such cases, the surfaces might appear to be rougher than they really are.

2.4.4 Profilometers and adequate sample size

For comparative reasons, 10 surface traces per sample with a spacing of approximately 1 cm were captured manually using a tactile profile gauge with 1 mm sampling steps. According to Muralha et al. (2014), at least 3 profiles per sample are recommended. The results of the 30 measurements are shown in Figure 2.14. The whiskers in the boxplot extend from the maximum to the minimum value of the population. The JRC were calculated based on Z_2, taking the whole length of the profiles into account. For sample B the profiles were 21.5 cm long on average, those of sample S 17.1 cm, and 15.4 cm for sample M. A correction of scale, which strictly speaking would be necessary according to Barton and Bandis (1982), has not been carried out. Taking profiles over the full sample length and not correcting them for scale is common practice for laboratory-scale samples (see e.g. Li and Zhang, 2015; Hencher and Richards, 2015). However, scale effects are inevitable and not quantifiable. For sample B, a mean JRC of 11.1 with a bandwidth of 4.4 was calculated from the tactile profilometer measurements. Compared to the mean JRC inferred from all 10-cm-long traces of the 3D data, which is 12.4 for the reference scan, the difference amounts to 1.3 JRC units. Regarding the mean for sample S and sample B, which came to be 8.4 (bandwidth 4.0) and 7.2 (bandwidth 3.2), the difference from the optically derived standard-length JRC amounts to 0.9 and 0.6, respectively (c.f. Figures 2.11 and 2.12). Surprisingly, the means from whole-length profilometer and standard-length optical measurements conform quite well. However, the bandwidths for the 10 profilometer measurements is large. For all three samples, the JRC span over two roughness classes (bandwidth of 4.0 units). Therefore, the question arises whether a sample size of 10 profiles is enough to characterise the surface roughness.

The issue of adequate sample size for profile measurements is exemplified for sample B in Figure 2.15. In order to eliminate scale effects, only standard-length profiles are taken into account. The uppermost histogram represents the basic population of JRC

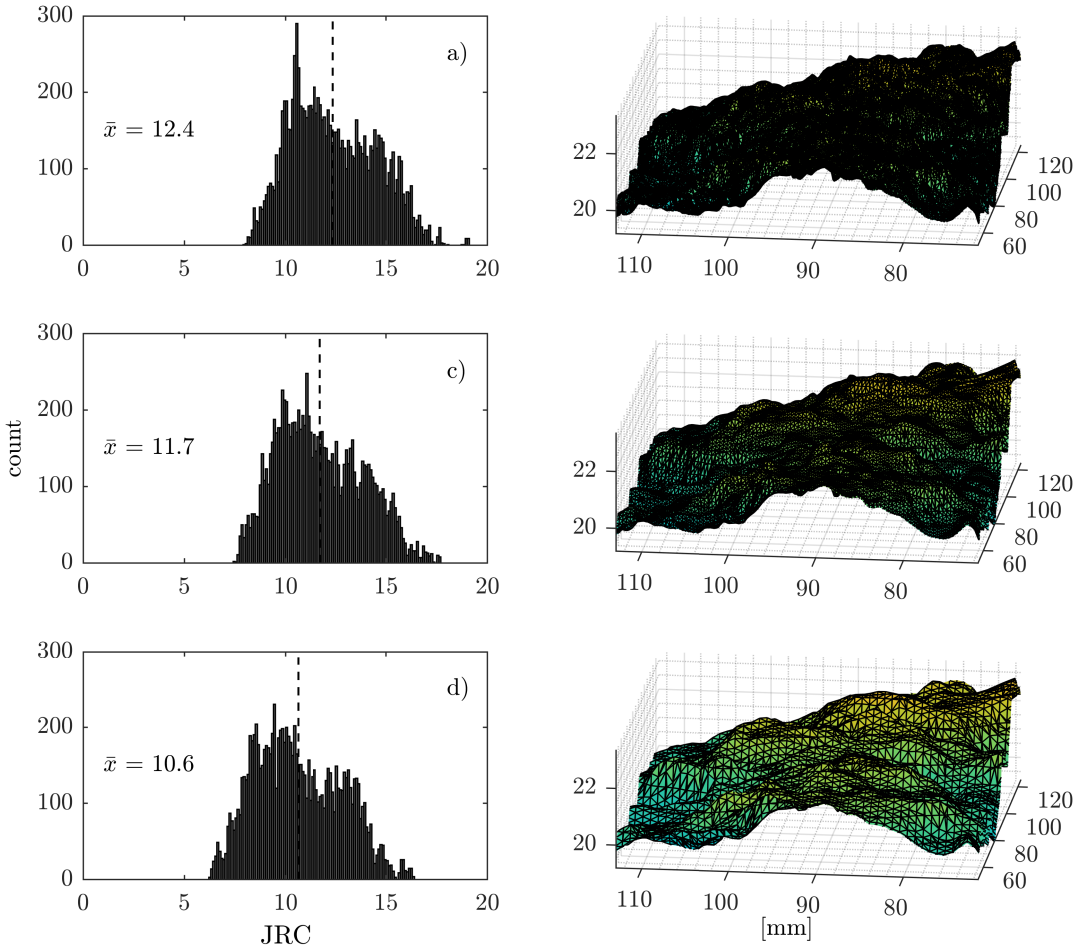

Figure 2.13: Influence of surface reconstruction based on Kazhdan and Hoppe (2013): a) original data; b) d=9, pts/node=10, α=5; and c) d=8, pts/node=20, α=10

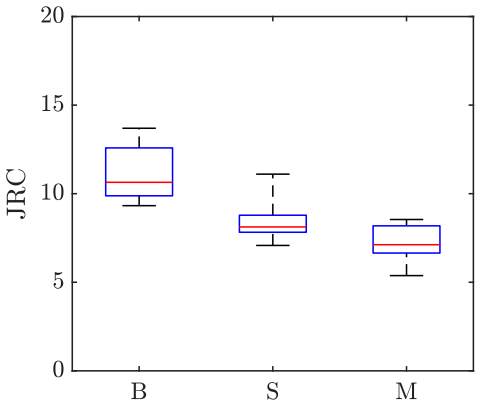

Figure 2.14: Boxplots of 10 tactile profile gauge measurements per sample

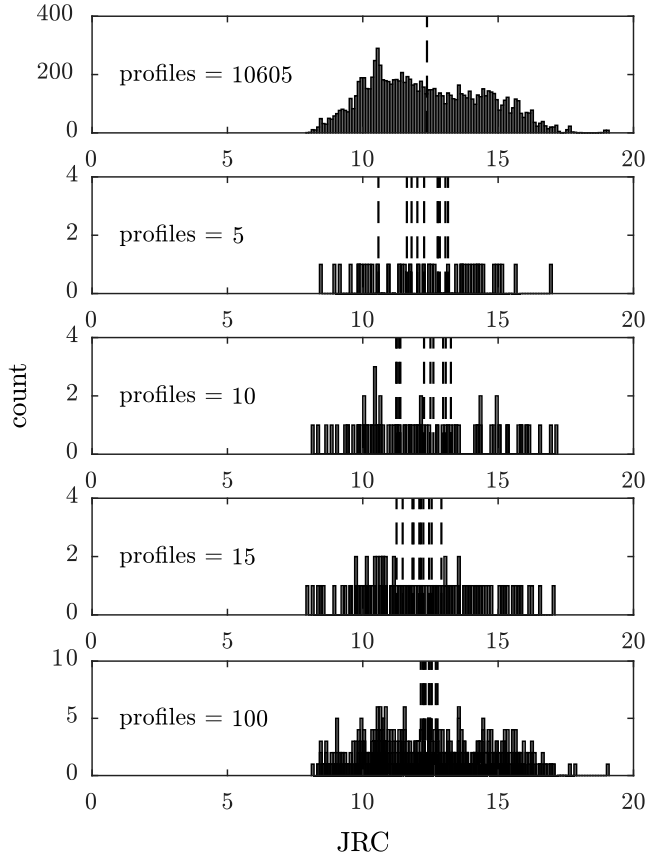

Figure 2.15: Comparison of different sample sizes

with a mean of 12.4. Technically, recording a profile with a digital or tactile profilometer is nothing else but arbitrarily picking from this basic population. Now imagine to manually record and process 5, 10 or 15 profiles. These are reasonable common numbers, but capturing these traces would already be a time-consuming task. As a benchmark, an extraction of 100 profiles was used. To make the differences clearer, the random selections were repeated 10 times, resulting in different mean values for the specific sub-sample. The means are marked as dotted lines in Figure 2.15. In case of a sample size of 5, the JRC means for 10 cycles lie between 10.6 and 13.1, resulting in a gap of 2.5 JRC units for this specific arrangement. Consequently, the information that can be deduced from the measurements is somewhat arbitrary since the user does not know how far away the outcome is from the basic population's mean. However, the range becomes successively smaller with increasing sample size. For the benchmark, the means span 12.1 to 12.8, with a cluster around the mean value of the basic population. This leads to the conclusion that 100 profile measurements would suffice to define a meaningful JRC. In summary, JRC values established based on a few profilometer measurements are to be treated with great caution. Even 15 profile measurements on a laboratory scale sample, which would exceed normal amounts in practice (e.g. Hencher and Richards, 2015; Muralha et al., 2014), would not satisfactorily reproduce the basic population.

Table 2.3: 3D roughness parameters (reference = stat.SLS)

Sample	Sensor	R_S	Grasselli's parameter set	
			$\theta^*_{max}/(C+1)$	GP
B	reference	1.061	11.14	11.27
	DIM	1.072	11.12	11.54
	hand.SLS	1.046	9.55	10.01
	TLS	1.036	8.75	8.73
S	reference	1.045	9.05	8.49
	DIM	1.045	9.13	8.60
	hand.SLS	1.020	6.38	5.77
	TLS	1.090	13.66	13.25
M	reference	1.025	5.02	6.56
	DIM	1.025	6.21	7.55
	hand.SLS	1.025	6.21	7.61
	TLS	1.031	8.29	9.02

2.4.5 Surficial roughness parameters

In this study, two 3D roughness parameters were calculated, namely R_S and Grasselli's parameter set. It is condensed in $GP = 2A_0[\theta^*_{max}/(C+1)]$ (Tatone and Grasselli, 2009). This parameter GP is dependent on the analysis direction. Here, the analysis was carried out parallel to the x-axis of the Cartesian coordinate system just like the extraction of the profiles. The results are summarised in Table 2.3.

Regarding R_S, the calculated values derived from DIM in comparison to the reference are in very good accordance. For samples S and M, the results are identical, and for sample B, the difference is much smaller than for the other optical measuring techniques. On the contrary, differences are computed for hand.SLS and TLS. For sample B, the index R_S decreases, probably due to smoothing of the surface during data processing, and therefore converges towards 1. This is comprehensible since for a perfect plane, R_S would equal 1. The reason for the drastic difference in TLS relative to the reference concerning sample S presumably lies in the large noise due to the radiometric properties of the surface, as mentioned earlier. For the schist sample, no marked discrepancies concerning R_S are visible since the surface is quite smooth, thus masking effects of varying resolution and accuracy of the sensors.

Concerning Grasselli's parameter set, the index GP is not as plain as R_S because it consists of three input values. The results are visualised in Figure 2.16. For all three samples, the course of the curves from DIM accord very well with the reference, and GP arrives at similar values. Differences of varying size and shape occur for hand.SLS and TLS. However, for these two optical tools, again no systematic change is revealed. Their curves lie above the reference for samples S and M, but underneath for sample B. Another noteworthy detail concerns the maximum apparent dip angle θ^*_{max}, being one out of three input values for GP. Focussing on sample B, it becomes evident that a rather minor decrease from 89.6° to 84° (TLS versus reference) results in a considerable decrease of GP. However, the differences in C and A_0 are small, and the shape of the TLS curve resembling the curve of the reference GP drops 2.5 units (see Figure 2.16 a)). This indicates a direct effect of measurement errors, noise, and the surface reconstruction upon θ^*_{max}. Therefore, GP is sensitive to changes of θ^*_{max} and it must be emphasized that the optical measuring technique has an immediate considerable impact.

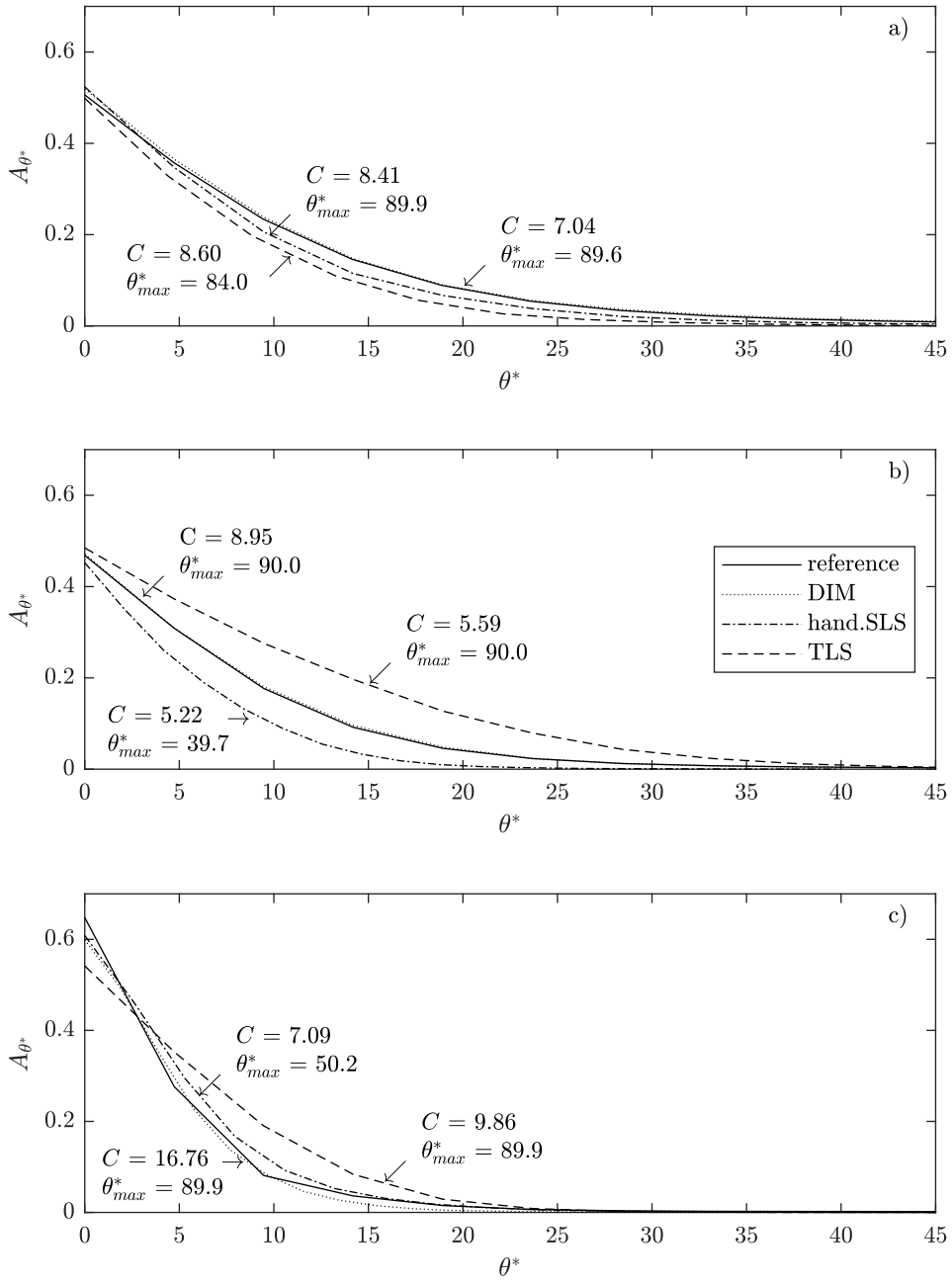

Figure 2.16: Grasselli's parameter GP for a) sample B, b) sample S and c) sample M

In summary, as discussed in subsection 2.4.2, DIM outperforms hand.SLS and TLS. The difference between the reference and hand.SLS data for 3D roughness measures, however, is not as pronounced as for profile-based JRC. Clearly, TLS leads to the largest differences.

2.5 Discussion

Calculated roughness values are always depended on the measuring equipment. However, certain optical measuring approaches are more useful to micro-roughness evaluation than others. This is because second order roughness features are of sub-millimetre size and therefore the measuring devices must be able to catch relatively small asperities. The measuring approaches that were used in this study have been shown to not necessarily meet this criterion but on paper some of them claim to do so. Presumably for that fact methods such as TLS have been used in previous studies to infer micro-roughness parameters (see introduction for details). As mentioned earlier, for the paper at hand the goal was to reflect these previous measuring setups.

It has been shown that stationary SLS captures the surfaces with high resolution and accuracy. Values of more than 18 points per square millimetre at an accuracy of 0.01 mm can be expected for the final processed surface mesh. The reason for that lies in the design which always ensures the orientation between the camera pairs to be known and to be stable over the measuring period. Moreover, using reference points enables the system to align multiple-view scans with great certainty. The result is data with very low noise, so the final meshes are trustworthy representations of the rock surface. Although, the same applies for the used handheld SLS concerning the design, its outcomes are not as good. The scope of application lies in a fast and intuitive way of producing aesthetic models of all kinds of objects such as architectural features or art statues already up to metric scale. However, the continuous unsteady motion of the device around the object of interest during measurement and the desire for not needing targets results in a challenging transformation of the successive scans into one coordinate system. Supposedly, that is why the data is relatively smoothed out during post-processing in the manufacturer's software. Therefore, the final meshes should be applied with some scepticism to micro-roughness determination. Nonetheless, handheld SLS was used in this study as the machines become more and more available, have better measuring capabilities than former techniques and are of prospect use to the engineering geological community as they are very much manageable in the field. Additionally, compared to the commonly used linear laser profilometers, hand.SLS yielded equivalent or even better accuracy with the advantage of capturing a whole surface rather than just one profile. Good usability in the field also relates to TLS, however, for determination of unevenness the error of the laser-based ranging is considerably larger than acceptable values for that purpose. The resulting meshes have been shown to be quite clean which is apparently also due to extensive smoothing in the software. This is reasonable to produce good-looking models because of the relatively large noise but it is useless for micro-roughness determination. The given rangefinder precision which amounts to 0.4 mm and which equals the spatial standard deviation of the resulting surface models (see section 2.4.1) is simply too large for the task. This technique was not capable of capturing small-scale unevenness even under controlled laboratory conditions. Instead, the results from dense image matching were not subject to that problem. Nonetheless, with this technique it is vital to carefully execute a specific routine when taking the photographs. The relative orientation of the viewpoints is calculated based on recurring features in the photos and therefore they

need to overlap to enable registration of the points in the cloud. It was shown that taking approximately 40 photographs of a 100 mm x 200 mm surface patch from distances between 0.3 and 1 m was very much suitable to attain meaningful representations of the rock surfaces. Another important parameter is the resolution of the sensor. The good results of this study were produced using a 36 MP sensor. In general, the higher the sensor's resolution and the smaller the object-to-camera distance are the higher the resolution of the point cloud becomes. However, with this method the greatest issue is the scaling of the outcome. Accordingly, a routine needs to be established using a well-defined geometric norm to introduce metric information into the point cloud. That way low standard spatial deviations can be received. Additionally, the method is promising regarding later field application since it is relatively inexpensive and portable. It can be concluded that in complying with the requirements stated above DIM is highly suitable for micro-roughness evaluation.

Undoubtably, there is a strong need for thorough recommendations that define minimum requirements concerning optical measuring techniques for successful application in the field of roughness determination. Without them comparing future works will remain challenging.

2.6 Conclusion

Within this study, four optical measuring techniques were applied to produce digital representations of rock joint surfaces enabling the calculation of 2D and 3D roughness measures. For the first time concerning actual rock surfaces, the paper at hand gives values for the achievable resolution and accuracy of the resulting models as a function of the used techniques under laboratory conditions. This is in contrast to previous studies which gave theoretical resolutions and accuracies of the devices only. However, in order to assess the quality of calculated roughness measures, in turn, it is essential to evaluate the quality of the surface models. For future works, as a first step towards better comparability, it is encouraged to always include information on the quality of the models (e.g. resolution, accuracy). This is especially important as new technologies offer a level of detail that has not been seen before. However, the question has to be answered if these high-resolutions are necessary since most empirical equations are based on lower resolution models. Additionally, comparing different models geometrically is error-prone due to the uncertainty in the transformation into one coordinate system. Therefore, in this study the comparison was done using the statistical distributions of roughness measures. The four roughness parameters used, namely Z_2, D, R_S and GP, were chosen according to their broad use in rock engineering research.

The application of dense image matching led to a high degree of accordance with the referential stationary structured light scanner, both for the spatial standard deviation and for the calculated roughness measures. However, for scaling of the models it is strongly recommended to introduce highly robust and well-defined geometric norms into the object space in order to ensure accuracy as the operation scale is very small. With respect to handheld structured light scanning, it can be concluded that the device used fills the gap between high-resolution, small scale stationary SLS and low-resolution, large scale TLS, on grounds of yielding results closer to the reference than TLS. Also, from this study it becomes clear that the use of TLS for second-order roughness evaluation in the laboratory needs to be avoided. Micro-roughness inferred from TLS field data is usually even more erroneous due to noise and should be discarded.

Furthermore, the general benefits of 3D data acquisition were addressed and ex-

plained based on the most popular roughness measure JRC. Using 3D models and the described post-processing routine all possible standard-length profilometer measurements were emulated which results in an extensive amount of data. Such an approach was used for the first time in this study. As a result, the subjective positioning of the profile on the surface and scale effects were avoided. Based on the generated histograms it must be concluded that defining a representative JRC solely based on a few profile measurements is not practicable as the ranges of values were wide. Additionally, JRC calculated from Z_2 are not interchangeable with JRC based on D. Concerning Grasselli's 3D roughness metric, a pronounced sensitivity to measurement errors and noise was seen. However, roughness parameters that take the whole surface into account might be more appropriate in the sense that they characterise and capture the sample in terms of one distinct, unmistakable value.

Prospective research should focus on additional criteria besides simple geometric parameters for the definition of profile-based roughness measures. Here, the fact might be of service that during shearing parts of large micro-relief facing the shear direction serve as obstacles. Hence, profiles incorporating these steps could be more suitable to define roughness from a mechanical point of view. Besides, profiles include the positive property of having a direction which is vital to shear resistance. When looking at 3D roughness measures undoubtedly the small amount of data is a problem. There is a great need for openly available surface models together with results from direct shear tests. Providing such data would enable the community of engineering geologists to calibrate potentially new and also older geometrical indices resulting in meaningful measures of roughness.

2.7 References

Abellán, A., Oppikofer, T., Jaboyedoff, M., Rosser, N. J., Lim, M., and Lato, M. J. (2014). Terrestrial laser scanning of rock slope instabilities. *Earth Surf Proc Land*, 39(1):80–97. https://doi.org/10.1002/esp.3493.

Alameda-Hernández, P., Jiménez-Perálvarez, J., Palenzuela, J. A., Hamdouni, R. E., Irigaray, C., Cabrerizo, M. A., and Chacón, J. (2014). Improvement of the JRC calculation using different parameters obtained through a new survey method applied to rock discontinuities. *Rock Mech Rock Eng*, 47(6):2047–2060. https://doi.org/10.1007/s00603-013-0532-2.

Artec (2019). Artec Scanners Booklet. https://www.artec3d.com/files/pdf/ArtecScanners-Booklet-EURO.pdf. Accessed: 2019-03-07.

Bandis, S., Lumsden, A., and Barton, N. (1981). Experimental studies of scale effects on the shear behaviour of rock joints. *Int J Rock Mech Min*, 18(1):1–21. https://doi.org/10.1016/0148-9062(81)90262-x.

Barton, N. (1973). Review of a new shear-strength criterion for rock joints. *Eng Geol*, 7(4):287–332. https://doi.org/10.1016/0013-7952(73)90013-6.

Barton, N. and Bandis, S. (1982). Effects of block size on the shear behavior of jointed rock. *Proceedings 23rd Symp. Rock Mechanics, August 25-27, 1982, Berkeley, CA*.

Barton, N. and Choubey, V. (1977). The shear strength of rock joints in theory and practice. *Rock Mech*, 10(1-2):1–54. https://doi.org/10.1007/bf01261801.

Belem, T., Homand-Etienne, F., and Souley, M. (2000). Quantitative parameters for rock joint surface roughness. *Rock Mech Rock Eng*, 33(4):217–242. https://doi.org/10.1007/s006030070001.

Bistacchi, A., Griffith, W. A., Smith, S. A., Toro, G. D., Jones, R., and Nielsen, S. (2011). Fault roughness at seismogenic depths from LIDAR and photogrammetric analysis. *Pure Appl Geophys*, 168(12):2345–2363. https://doi.org/10.1007/s00024-011-0301-7.

Bitenc, M., Kieffer, D., Khoshelham, K., and Vezocnik, R. (2015). Quantification of rock joint roughness using terrestrial laser scanning. *Proceedings IAEG XII Congress, September 15-19, 2014, Torino, Italy*.

Böhler, W., Vicent, M. B., and Marbs, A. (2003). Investigating laser scanner accuracy. *Proceedings Cipa 2003 International Symposium, September 30 - October 04, 2003, Antalya, Turkey*.

Böhm, J. and Becker, S. (2007). Automatic marker-free registration of terrestrial laser scans using reflectance features. *Proceedings 8th Conference on Optical 3D Measurement Techniques, Zurich, Switzerland*.

Brown, S. R. (1995). Simple mathematical model of a rough fracture. *J Geophys Res - Sol Ea*, 100(B4):5941–5952. https://doi.org/10.1029/94jb03262.

Cignoni, P., Rocchini, C., and Scopigno, R. (1998). Metro: Measuring error on simplified surfaces. *Computer Graphics Forum*, 17(2):167–174. https://doi.org/10.1111/1467-8659.00236.

Fardin, N., Feng, Q., and Stephansson, O. (2004). Application of a new in situ 3d laser scanner to study the scale effect on the rock joint surface roughness. *Int J Rock Mech Min*, 41(2):329–335. https://doi.org/10.1016/s1365-1609(03)00111-4.

Fardin, N., Stephansson, O., and Jing, L. (2001). The scale dependence of rock joint surface roughness. *Int J Rock Mech Min*, 38(5):659–669. https://doi.org/10.1016/s1365-1609(01)00028-4.

FARO (2019). FARO Laser Scanner Focus3D X330 techsheet. http://www.faro.com/download-center. Accessed: 2019-03-07.

Furukawa, Y. and Hernández, C. (2015). Multi-view stereo: A tutorial. *Foundations and Trends in Computer Graphics and Vision*, 9(1-2):1–148. https://doi.org/10.1561/0600000052.

Gao, Y. and Wong, L. N. Y. (2015). A modified correlation between roughness parameter z 2 and the JRC. *Rock Mech Rock Eng*, 48(1):387–396. https://doi.org/10.1007/s00603-013-0505-5.

Ge, Y., Tang, H., Eldin, M. M. E., Chen, P., Wang, L., and Wang, J. (2015). A description for rock joint roughness based on terrestrial laser scanner and image analysis. *Scientific Reports*, 5(1):16999. https://doi.org/10.1038/srep16999.

GOM (2019). Webpage of GOM Atos Measuring System. https://www.gom.com/metrology-systems/atos.html. Accessed: 2019-03-07.

Grasselli, G. and Egger, P. (2003). Constitutive law for the shear strength of rock joints based on three-dimensional surface parameters. *Int J Rock Mech Min*, 40(1):25–40. https://doi.org/10.1016/s1365-1609(02)00101-6.

Grasselli, G., Wirth, J., and Egger, P. (2002). Quantitative three-dimensional description of a rough surface and parameter evolution with shearing. *Int J Rock Mech Min*, 39(6):789–800. https://doi.org/10.1016/s1365-1609(02)00070-9.

Haala, N. (2011). Multiray photogrammetry and dense image matching. *Proceedings Photogrammetric Week '11*.

Haneberg, W. (2007). Directional roughness profiles from three-dimensional photogrammetric or laser scanner point clouds. *Proceedings 1st CANUS Rock Mechanics Symposium, May 27-31, 2007, Vancouver, Canada*.

Hencher, S. and Richards, L. (2015). Assessing the shear strength of rock discontinuities at laboratory and field scales. *Rock Mech Rock Eng*, 48(3):883–905. https://doi.org/10.1007/s00603-014-0633-6.

Hirschmüller, H. (2005). Accurate and efficient stereo processing by semi-global matching and mutual information. *Proceedings IEEE Conference on Computer Vision and Pattern Recognition (CVPR), June 20-26, 2005, San Diego, CA*.

Hirschmüller, H. (2008). Stereo processing by semiglobal matching and mutual information. *IEEE T Pattern Anal*, 30(2):328–341. https://doi.org/10.1109/tpami.2007.1166.

Höfle, B., Geist, T., Rutzinger, M., and Pfeifer, N. (2007). Glacier surface segmentation using airborne laser scanning point cloud and intensity data. *Proceedings of the ISPRS Workshop 'Laser Scanning 2007 and SilviLaser 2007', September 12-14, 2007, Espoo, Finland*.

Höfle, B. and Pfeifer, N. (2007). Correction of laser scanning intensity data: Data and model-driven approaches. *ISPRS J Photogramm*, 62(6):415–433. https://doi.org/10.1016/j.isprsjprs.2007.05.008.

Huang, C., White, I., Thwaite, E., and Bendeli, A. (1988). A noncontact laser system for measuring soil surface topography. *Soil Sci Soc Am J*, 52(2):350–355. https://doi.org/10.2136/sssaj1988.03615995005200020009x.

Ishibashi, T., Watanabe, N., Hirano, N., Okamoto, A., and Tsuchiya, N. (2015). Beyond-laboratory-scale prediction for channeling flows through subsurface rock fractures with heterogeneous aperture distributions revealed by laboratory evaluation. *J Geophys Res - Sol Ea*, 120(1):106–124. https://doi.org/10.1002/2014jb011555.

ISRM (1978). Suggested methods for the quantitative description of discontinuities in rock masses. *Int J Rock Mech Min*, 15(6):319–368. https://doi.org/10.1016/0148-9062(78)91472-9.

JAG3D (2018). OpenAdjustment - An OpenSource Least-Squares-Adjustment Tool. http://javagraticule3d.sourceforge.net. Accessed: 2018-09-22.

Jang, H.-S. and Jang, B.-A. (2015). New method for shear strength determination of unfilled, unweathered rock joint. *Rock Mech Rock Eng*, 48(4):1515–1534. https://doi.org/10.1007/s00603-014-0660-3.

Jiang, Y., Li, B., and Tanabashi, Y. (2006). Estimating the relation between surface roughness and mechanical properties of rock joints. *Int J Rock Mech Min*, 43(6):837–846. https://doi.org/10.1016/j.ijrmms.2005.11.013.

Jutzi, B. and Stilla, U. (2003). Laser pulse analysis for reconstruction and classification of urban objects. *Proceedings Photogrammetric Image Analysis Workshop, September 17-19, 2003, Munich, Germany*.

Kazhdan, M. and Hoppe, H. (2013). Screened poisson surface reconstruction. *ACM T Graphic*, 32(3):1–13. https://doi.org/10.1145/2487228.2487237.

Kemeny, J., Turner, K., and Norton, B. (2006). Lidar for rock mass characterization: Hardware, software, accuracy and best-practices. *Proceedings Laser and Photogrammetric Methods for Rock Face Characterization Workshop, June 17-18, 2006, Golden, CO*.

Kim, D. H., Gratchev, I., and Balasubramaniam, A. (2013). Determination of joint roughness coefficient (JRC) for slope stability analysis: a case study from the gold coast area, australia. *Landslides*, 10(5):657–664. https://doi.org/10.1007/s10346-013-0410-8.

Kim, D. H., Poropat, G. V., Gratchev, I., and Balasubramaniam, A. (2015). Improvement of photogrammetric JRC data distributions based on parabolic error models. *Int J Rock Mech Min*, 80:19–30. https://doi.org/10.1016/j.ijrmms.2015.09.007.

Ladanyi, B. and Archambault, G. (1970). Simulation of shear behavior of a jointed rock mass. *Proceedings 11th Symp. Rock Mechanics, June 16-19, 1969, Berkeley, CA*.

Lange, D. A., Jennings, H. M., and Shah, S. P. (1993). Relationship between fracture surface roughness and fracture behavior of cement paste and mortar. *J Am Ceram Soc*, 76(3):589–597. https://doi.org/10.1111/j.1151-2916.1993.tb03646.x.

Lee, Y.-H., Carr, J., Barr, D., and Haas, C. (1990). The fractal dimension as a measure of the roughness of rock discontinuity profiles. *Int J Rock Mech Min*, 27(6):453–464. https://doi.org/10.1016/0148-9062(90)90998-h.

Li, Y. and Huang, R. (2015). Relationship between joint roughness coefficient and fractal dimension of rock fracture surfaces. *Int J Rock Mech Min*, 75:15–22. https://doi.org/10.1016/j.ijrmms.2015.01.007.

Li, Y. and Zhang, Y. (2015). Quantitative estimation of joint roughness coefficient using statistical parameters. *Int J Rock Mech Min*, 77:27–35. https://doi.org/10.1016/j.ijrmms.2015.03.016.

Liu, Q., Tian, Y., Liu, D., and Jiang, Y. (2017). Updates to JRC-JCS model for estimating the peak shear strength of rock joints based on quantified surface description. *Eng Geol*, 228:282–300. https://doi.org/10.1016/j.enggeo.2017.08.020.

Lourakis, M. and Argyros, A. (2004). The Design and Implementation of a Generic Sparse Bundle Adjustment Software Package Based on the Levenberg-Marquardt Algorithm. Technical Report FORTH-ICS/TR-340, Institute of Computer Science, Heraklion, Crete, Greece.

Lowe, D. G. (2004). Distinctive image features from scale-invariant keypoints. *Int J Comput Vision*, 60(2):91–110. https://doi.org/10.1023/b:visi.0000029664.99615.94.

Luhmann, T., Robson, S., Kyle, S., and Harley, I. (2011). *Close range photogrammetry: principles, techniques and applications*. Whittles Publishing, Dunbeath.

Maerz, N., Franklin, J., and Bennett, C. (1990). Joint roughness measurement using shadow profilometry. *Int J Rock Mech Min*, 27(5):329–343. https://doi.org/10.1016/0148-9062(90)92708-m.

Mah, J., Samson, C., McKinnon, S. D., and Thibodeau, D. (2013). 3d laser imaging for surface roughness analysis. *Int J Rock Mech Min*, 58:111–117. https://doi.org/10.1016/j.ijrmms.2012.08.001.

Marsch, K. and Wujanz, D. (2016). Determination of roughness parameters based on dense image matching and structured light scanning. *Proceedings 2nd Virtual Geoscience Conference, September 22-23, 2016, Bergen, Norway*.

Milenković, M., Pfeifer, N., and Glira, P. (2015). Applying terrestrial laser scanning for soil surface roughness assessment. *Remote Sensing*, 7(2):2007–2045. https://doi.org/10.3390/rs70202007.

Milne, D., Hawkes, C., and Hamilton, C. (2009). A new tool for the field characterization of joint surfaces. *Proceedings 3rd CANUS Rock Mechanics Symposium, May 2009, Toronto, Canada*.

Muralha, J., Grasselli, G., Tatone, B., Blümel, M., Chryssanthakis, P., and Yujing, J. (2014). ISRM suggested method for laboratory determination of the shear strength of rock joints: Revised version. *Rock Mech Rock Eng*, 47(1):291–302. https://doi.org/10.1007/s00603-013-0519-z.

Myers, N. (1962). Characterization of surface roughness. *Wear*, 5(3):182–189. https://doi.org/10.1016/0043-1648(62)90002-9.

Nguyen, H., Fernandez-Steeger, T., Wiatr, T., Rodrigues, D., and Azzam, R. (2011). Use of terrestrial laser scanning for engineering geological applications on volcanic rock slopes – an example from madeira island (portugal). *Nat Hazard Earth Sys*, 11(3):807–817. https://doi.org/10.5194/nhess-11-807-2011.

Nilsson, M., Edelbro, C., and Sharrock, G. (2012). Small scale joint surface roughness evaluation using digital photogrammetry. *Proceedings Eurock2012, May 28-30, 2012, Stockholm, Sweden*.

Oglesby, J., Kolb-Lugo, J., Brown, S., Harris, A., Hudyma, N., Johansen, D., and Bliss, A. (2017). Comparison of roughness indices from weathered, differentially weathered and vuggy profiles obtained using laser scanning and photogrammetry. *Proceedings 51st U.S. Rock Mechanics/Geomechanics Symposium, 25-28 June, San Francisco, CA*.

Pardini, G. and Gallart, F. (1998). A combination of laser technology and fractals to analyse soil surface roughness. *Eur J Soil Sci*, 49(2):197–202. https://doi.org/10.1046/j.1365-2389.1998.00149.x.

Pollyea, R. M. and Fairley, J. P. (2011). Estimating surface roughness of terrestrial laser scan data using orthogonal distance regression. *Geology*, 39(7):623–626. https://doi.org/10.1130/g32078.1.

Reeves, M. (1985). Rock surface roughness and frictional strength. *Int J Rock Mech Min*, 22(6):429–442. https://doi.org/10.1016/0148-9062(85)90007-5.

Riegl (2019). VZ-6000 datasheet. http://www.riegl.com/uploads/tx_pxpriegldownloads/RIEGL_VZ-6000_Datasheet_2018-12-05.pdf. Accessed: 2019-03-07.

Rothermel, M., Wenzel, K., Fritsch, D., and Haala, N. (2012). Sure: Photogrammetric surface reconstruction from imagery. *Proceedings LC3D Workshop, December, 2012, Berlin, Germany*.

Soudarissanane, S., Lindenbergh, R., Menenti, M., and Teunissen, P. (2011). Scanning geometry: Influencing factor on the quality of terrestrial laser scanning points. *ISPRS J Photogramm*, 66(4):389–399. https://doi.org/10.1016/j.isprsjprs.2011.01.005.

Sturzenegger, M. and Stead, D. (2009). Close-range terrestrial digital photogrammetry and terrestrial laser scanning for discontinuity characterization on rock cuts. *Eng Geol*, 106(3-4):163–182. https://doi.org/10.1016/j.enggeo.2009.03.004.

Surphaser (2017). Surphaser 100HSX data sheet. http://www.surphaser.com/pdf/Surphaser%20100HSX.pdf. Accessed: 2019-03-07.

Tatone, B. S. and Grasselli, G. (2009). A method to evaluate the three-dimensional roughness of fracture surfaces in brittle geomaterials. *Rev Sci Instrum*, 80(12):125110. https://doi.org/10.1063/1.3266964.

Tatone, B. S. A. and Grasselli, G. (2013). An investigation of discontinuity roughness scale dependency using high-resolution surface measurements. *Rock Mech Rock Eng*, 46(4):657–681. https://doi.org/10.1007/s00603-012-0294-2.

Vogler, D., Walsh, S. D., Bayer, P., and Amann, F. (2017). Comparison of surface properties in natural and artificially generated fractures in a crystalline rock. *Rock Mech Rock Eng*, 50(11):2891–2909. https://doi.org/10.1007/s00603-017-1281-4.

Vosselman, G. and Maas, H. (2010). *Airborne and terrestrial laser scanning*. CRC Press, Boca Raton.

Wernecke, C. and Marsch, K. (2015). Mapping rock surface roughness with photogrammetry. *Proceedings Eurock2015, October 7-10, 2015, Salzburg, Austria*.

Wujanz, D. (2012). Towards transparent quality measures in surface based registration processes: Effects of deformation onto commercial and scientific implementations. *Proceedings of the XXII Congress of the International Society of Photogrammetry and remote Sensing, Melbourne, Australia*.

Wujanz, D., Burger, M., Mettenleiter, M., and Neitzel, F. (2017). An intensity-based stochastic model for terrestrial laser scanners. *ISPRS J Photogramm*, 125:146–155. https://doi.org/10.1016/j.isprsjprs.2016.12.006.

Yu, X. and Vayssade, B. (1991). Joint profiles and their roughness parameters. *Int J Rock Mech Min*, 28(4):333–336. https://doi.org/10.1016/0148-9062(91)90598-g.

Chapter 3

Comparative evaluation of statistical and fractal approaches for JRC calculation based on a large dataset of natural rock traces

Marsch, K., and Fernandez-Steeger, T. M. (2021). Comparative Evaluation of Statistical and Fractal Approaches for JRC Calculation Based on a Large Dataset of Natural Rock Traces. *Rock Mech Rock Eng*, 54:1897-1917.
https://doi.org/10.1007/s00603-020-02348-0

Abstract

After the publication of the type-profiles for the estimation of the Joint Roughness Coefficient (JRC) a discussion evolved about how to adequately use these traces. Based on the chart numerous researchers assembled mathematical correlations with various parameters seeking objectivity in the determination of JRC. Within these works differences concerning the database and the mathematical implementations exist. Consequently, each correlation, although predominantly the same parameters are used, leads to different JRC values. In theory, for any arbitrary profile, irrespective of the particular calculation approach, the same JRC should result. This is a requisite because of the referencing of all correlations to the 10 type-profiles. However, it is shown in this study that in most cases equal or even satisfactorily similar results are not obtained. The discrepancies are vast when non-standard profiles are evaluated, in this case, more than 40,000 traces from six different rock surfaces that cover a broad range of roughness categories. The simple intuitive parameter Z_2 served as an agent for the statistical methods because of its broad use and consequently good comparability. On the part of the fractal approaches, three definitions were used. However, JRC inferred from fractal correlations are very much dependent on the particular calculation routine. In fact, the theory of fractals is overly complex for the sparse and low-resolution type-profiles. In summary, fractal approaches do not produce safer or more reliable estimates of roughness compared to simple statistical means and using Z_2 perfectly suffices to determine the class of JRC.

3.1 Introduction

Since the introduction of Barton's empirical shear strength criterion in 1973 there has been a discussion about how to reliably determine the joint roughness coefficient (JRC) as a mechanically meaningful measure for rock surface roughness. Barton and Choubey (1977) published a chart containing 10 type-profiles to estimate the JRC by visual comparison. In doing so, the JRC, being a parameter rather of mechanical nature that shall embrace all effects of roughness within shearing processes, is determined from morphological surface roughness along a profile, of course preferably in shear direction. The initial intention was to enable engineers and geologists to "make a quick estimate" (Barton and Choubey, 1977) of JRC without conducting sophisticated mechanical direct shear tests.

However, this practice of roughness determination was questioned since human eye-based visual comparison is error-prone and highly subjective (e.g. Beer et al., 2002; Alameda-Hernández et al., 2014). Therefore, it seems reasonable to eliminate the user's influence by applying mathematical means. In the case of surface roughness, this is a common approach in engineering and material sciences (e.g. ISO 4287, 1997). Consequently, based on the standard chart numerous researchers assembled mathematical correlations with various parameters seeking objectivity in the determination of JRC. Tse and Cruden (1979) were the first to calculate statistical parameters for the type-profiles and to correlate them with JRC. Since then, many authors have published a still growing number of correlations of other statistical parameters. Li and Zhang (2015) give a rather recent overview of these endeavours. Apart from statistical approaches, the theory of fractals was also applied to the problem. Turk et al. (1987) spearheaded the calculation of the fractal dimension D for the 10 type-profiles using the divider method. A compilation of other fractal correlations is available in Li and Huang (2015). Additionally, Magsipoc et al. (2020) recently published an overview of most methods for surface roughness determination in two and three dimensions that have been applied also in part to JRC determination. Till now, correlating all kinds of mathematical parameters with JRC, using different techniques is ongoing. Besides many others, for example, Ficker and Martišek (2016) used an image recognition approach, Wang et al. (2017) used support vector regression to calculate JRC, Yong et al. (2018) applied a vector similarity measure and Gravanis and Pantelidis (2019) employed the theory of random fields. However, to date they remain singular cases and statistical and fractal means have been explored more often. Nevertheless, the usefulness of repetitive correlation of already used or new measures with JRC solely based on the type-profiles must be doubted for various reasons.

Within previous works, differences concerning the database exist. Even though all correlations refer to the 10 type-profiles they were digitised by the various researchers in different ways, resulting in varying resolution and subsequently different sampling intervals. For example, the pioneers Tse and Cruden (1979) enlarged the profiles with a factor of 2.5 and picked points in an interval of 1.27 mm using a digitising table. Consequently, an effective sampling interval of approximately 0.5 mm was achieved. Yu and Vayssade (1991) and Tatone (2009) also performed scanning, enlarging, and manual tracing of the type-profiles at sampling intervals between 0.5 and 2.4 mm. Instead, Bae et al. (2011) used a digital copy of the type-profiles for image analysis in order to extract points on the profiles automatically. They reported a resolution of 20 pixels per 1 mm resulting in a sampling interval of 0.05 mm. Overall, concerning the digitalisations of the type-profiles, Tatone (2009) stands out. He was the first to make his digital type-profiles

publicly available. Unfortunately, since then only Li and Zhang (2015) and Stigsson and Mas Ivars (2019) followed the lead and published their source data.

Besides the differing database, uncertainty concerning the calculation procedures exist. Often, the implementations of the algorithms and the pre-processing steps of the data are not described in their entirety. However, adequate traceability is especially important with fractal approaches. If thorough documentation is not supplied, reproduction of prior findings is nearly impossible or at least achieving similarity is, in either case, cumbersome. Consequently, even when the same data is used different values of JRC result. Especially for the fractal dimension, the discrepancies are large since several calculation routines have been used in the past (c.f. Magsipoc et al., 2020). Moreover, in this context, confusion exists regarding the applicability of the different fractal calculation approaches with respect to the self-affine nature of rock discontinuity profiles.

Most importantly, for any arbitrary profile, irrespective of the particular calculation approach, the same JRC should result. This is a requisite because of the referencing of all correlations to the 10 type-profiles. Consequently, statistical and fractal approaches must yield the same JRC. However, previous publications used statistical or fractal techniques independently and never compared resulting JRC directly. Furthermore, they often focused on the type-profiles only. Nevertheless, it is extremely important to compare the approaches for a larger dataset of profiles to evaluate their universal validity. Only Marsch et al. (2020) investigated the problem rudimentary. They showed that JRC calculated from the statistical parameter Z_2 were not equal or even satisfactorily similar to JRC calculated e.g. from the fractal compass dimension D_{comp}. Certainly, there is a strong need for analyses of naturally occurring profiles other than the type-profiles.

Due to the problems addressed above, this study aims towards testing the hypothesis whether for any profile the same JRC results independent of the calculation scheme. This is achieved by revisiting the type-profiles and additional application of the approaches to six different rock surfaces. Having particularly field engineers and practitioners in mind, the primary objective is to denominate the most simple, intuitive, and reliable approach amongst a selection of tools available, may they be statistical or fractal procedures.

Firstly, some general remarks on the quality and availability of the type-profiles are given. This is followed by a presentation of the mathematical methods used. In section four the sensitivity of these methods is discussed by evaluating different digitalisations of the type-profiles. Thereafter, the application of the approaches to six different rock samples forms the main part of the study. Finally, the outcome is discussed, and conclusions are drawn.

3.2 General issues concerning the database for JRC correlations

Without exceptions, the set of Barton and Choubey's (1977) ten type-profiles forms the basis for all previously published correlations between JRC and statistical or fractal values. As marginal note—a few authors, e.g. Li and Zhang (2015) and Li et al. (2017), also included other profiles available in the literature, e.g. from Bandis (1980). However, this does not necessarily improve the correlations. When using these functions some fundamental problems with the referential type-profiles must be considered.

3.2.1 Measurement quality of the original type-profiles

Due to the only graphical presentation of the type-profiles, it is practically impossible to assess the quality of the measurements. Additionally, in the original publication the

type-profiles are downscaled compared to the initial measuring length whereby information is lost. Consequently, the profiles appear to be continuous which is incomprehensible, as the traces were gathered with a tactile profilometer and therefore should exhibit a stepwise progression (see Tatone and Grasselli, 2010). Moreover, the device consists of aligned metal pins of usually 1 mm in diameter, which are pressed onto the surface to gather the height information. During this process, an unavoidable deformation of the pins occurs leaving behind small gaps in the trace and resulting in variable sampling intervals. Following the classic approach, the profilometer measurements are transformed to paper by hand, which adds another source of error as the pins might slip again. Additionally, with the apparatus roughness wavelengths below 1 mm are not resolved, and, obviously, wavelengths greater than the profilometer, which is usually 100 to 150 mm in length, are also not collected. Moreover, solely the largest amplitude over the length of the pin diameter is measured. The device, therefore, acts as a low-cut filter and band-pass filters the original surface trace (Maerz et al., 1990). Indeed, all measuring approaches let them be contactless optical devices or tactile procedures do have a limited resolution and low-cut filtering is always happening. However, with the tactile profilometer, the resolution is relatively low, compared to most recent measuring tools, amounting to 1 mm only.

In summary, due to the uncertainties described above it is pointless to use finer sampling resolutions when digitising the type-profiles (as it was done by many authors in the past). Consequently, applying more and more sophisticated measuring devices for natural surfaces with higher resolution is unneeded if the objective is to determine the JRC based on the 10 type-profiles. At all times, it must be kept in mind that all correlations rest upon the sparse, low-resolution, and from today's perspective inexact type-profiles.

3.2.2 Available input data

As pointed out in the introduction, only a hand full of researchers made their digitalisations accessible. As an example for the available three data sets, in Figure 3.1 the fifth type-profile (JRC = 9.5) is displayed. At first glance the traces appear similar. However, with increasing length the variations in height grow larger. There seems to exist a tipping point at approximately 32 mm where a steep increase in the lines is seen. After that, the lines diverge more. Certainly, due to contrasting digitalisation procedures discrepancies are visible and consequently statistical and fractal parameters will be, most likely, unequal amongst the data sets. Additionally, in Figure 3.1 the overall trends of the traces are indicated as dotted lines colour-coded according to each originator. It will be shown that removing these overall trends is of major importance. It is essential to establish a horizontal datum line always in the same manner in order to obtain reproducible and reasonable roughness measures.

Apart from the height variations, different degrees of detail are also visible in Figure 3.1. Especially between the blue line and the red and orange lines at the relative peak at 55 mm length, the contrast is large. Generally, the various authors of the available correlations not only used separate methods for digitalisation but also, applied disparate sampling intervals. This is also valid for the profiles in Figure 3.1. Accordingly, the amounts of sampling points and the sampling intervals are shown in Figure 3.2. Li and Zhang (2015) and Tatone (2009) sampled the profiles with a constant interval of 0.4 mm and 0.5 mm, respectively. Instead, Stigsson and Mas Ivars (2019) picked points with an average spacing of 1 mm using sampling steps of up to 4.4 mm, however referencing their later correlation to a different, not available data set from Jang et al. (2014).

Remember, the original data from Barton and Choubey (1977) was gathered using

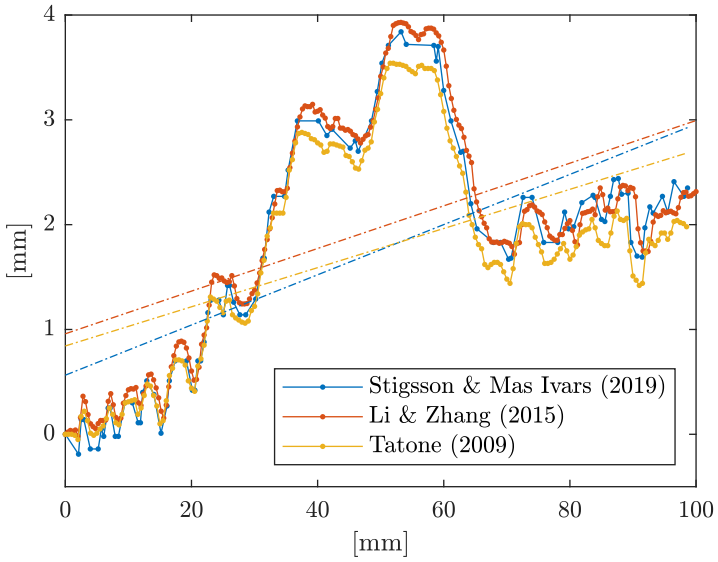

Figure 3.1: Variation of the fifth type-profile (JRC = 9.5, exaggeration in height 15)

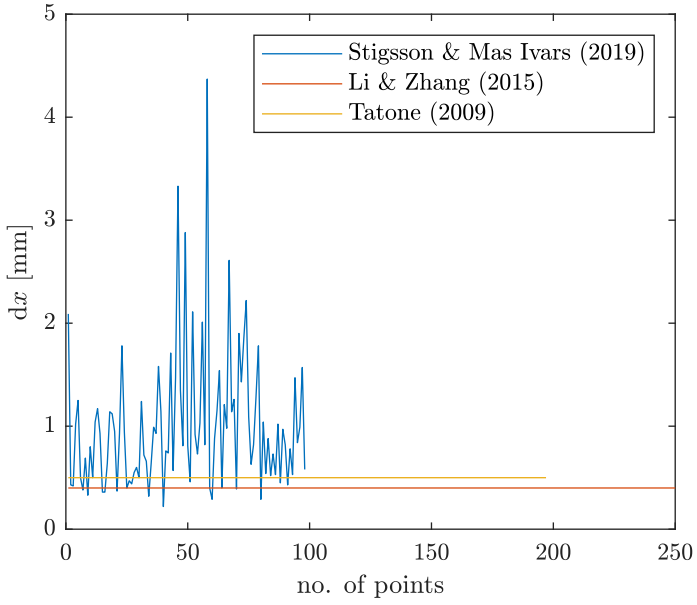

Figure 3.2: Amounts and spacings of sampling points for type-profile five

a resolution of 1 mm. Therefore, using a larger sampling rate would inevitably lead to noise in the secondary profiles. On the other hand, obviously using lower sampling rates would lead to a loss of information. Already Yu and Vayssade (1991) addressed the issue related to sampling. However, they only pointed out that it is important to adjust the correlation functions to the sampling interval and vice-versa. Regardless, for their (inaccessible) digitalisation they also used sampling intervals smaller than the one of the original type-profiles.

For future works (in case adding another correlation to the already plenty is desired) it is advisable to use an existing data set in order to eliminate an influencing variable. From the available data of Figures 3.1 and 3.2, the one from Tatone (2009) is most suitable as a reference set: the type-profiles were digitised using the original sampling interval of 1 mm and the overall trends in the profiles have been removed. Moreover, his routine is well documented and good enough in light of the low graphical quality of the original type-profiles.

3.3 Methods

In principle, there are two possibilities to calculate JRC: using statistical parameters, or using fractal approaches in various peculiarities. In isolated cases, other approaches have been used (e.g. Tatone, 2009; Zhang et al., 2014; Pickering and Aydin, 2016). The mathematical implementation of most of the statistical parameters is straightforward and software for simple spreadsheet analysis suffice for the calculation. Instead, certain algorithms for the calculation of the fractal dimension are quite elaborate, mathematically complex, and consume computational power. For this paper, all calculation approaches were implemented in Matlab© and the function scripts and data are available in the online repository to this publication (see Marsch, 2020).

3.3.1 Statistical Parameters

From all statistical parameters that have been used in rock mechanics the root mean square of the first derivative of the surface profile, named Z_2, is the one used most (c.f. Li and Zhang, 2015). Myers (1962) established the parameter for use in material sciences and it is written in Equation 3.1. When using a constant sampling interval Equation 3.1 evolves to the discrete form of Equation 3.2 where N is the total number of vertices and y_i the height coordinate of the profile points.

$$Z_2 = \sqrt{\frac{1}{L}\int_0^L \left(\frac{\mathrm{d}y}{\mathrm{d}x}\right)^2 \mathrm{d}x} \tag{3.1}$$

$$Z_2 = \sqrt{\frac{1}{(N-1)(\mathrm{d}x)^2}\sum_{i=1}^{N-1}(y_{i+1}-y_i)^2} \tag{3.2}$$

Besides, individual authors used other statistical parameters, such as the standard deviation of the slope angles of each sampling step σ_i (Yu and Vayssade, 1991) or the ultimate slope of the profile λ, as a measure of the peak amplitude of the profile versus its projected length (Barton and de Quadros, 1997). Examples of other parameters used more often than σ_i and λ are the roughness profile index R_p (Tatone and Grasselli, 2010; Yu and Vayssade, 1991; Maerz et al., 1990) and the so-called Structure Function of the profile, termed SF (Tse and Cruden, 1979; Yu and Vayssade, 1991; Yang et al., 2001). R_p is

defined as the ratio between the actual versus the projected length of the profile whereas SF can be calculated from Z_2 by introducing the sampling interval.

It will be shown later that the statistical parameters mentioned are interchangeable to a certain degree. Therefore, in this study, the inference of JRC from statistical values is represented by using Z_2 and the correlation from Tatone and Grasselli (2010). Indeed, other correlations, such as the ones from Yu and Vayssade (1991) or from Tse and Cruden (1979), yield quite similar results. However, Tatone and Grasselli (2010) made their input data accessible and they used a 1 mm sampling interval for digitalisation in compliance with Barton and Choubey (1977). The correlation of JRC with Z_2 from Tatone and Grasselli (2010) reads as follows:

$$\mathrm{JRC}_{Z_2} = 55.03 \cdot (Z_2)^{0.74} - 6.1 \tag{3.3}$$

3.3.2 Fractal measures

By means of the theory of fractals, it is possible to measure irregular and complex natural patterns even on small scales (Hastings and Sugihara, 1994). The essential requirement for the use of the fractal concept for roughness determination is the distinction between (a) self-similarity and (b) self-affinity. These qualities exist for natural entities that are build out of recurring patterns of themselves so that they look alike and/or have the same statistical properties on different scales. With self-similar profiles, rescaling is isotropic. However, for self-affine profiles rescaling has to be different for each direction to obtain the same appearance and/or statistical properties. Kulatilake et al. (2006) postulated that rock discontinuity profiles are of self-affine nature. This is fundamental since the difference between self-similarity and self-affinity entails the need for diverse calculation procedures for the fractal dimension D or the Hurst-exponent H, which convert into each other.

In past studies, the term fractal dimension has been used quite unthinkingly in the context of rock roughness evaluation. Of course, different authors applied different calculation procedures, e.g. compass walking, box counting or spectral analysis. Consequently, different numbers for D for the type-profiles were calculated (e.g. Lee et al., 1990; Odling, 1994). However, researchers claimed to have calculated "the fractal dimension". Instead, it is of paramount importance to distinguish between the values according to the calculation algorithms, as they are obviously not interchangeable. Mandelbrot (1985) himself—who is widely regarded as the initiator of the fractal theory—suggested that different denominations, such as "compass dimension" or "box dimension", should be used.

Concerning fractal measures, in the beginning of their application to JRC calculation, researchers like Turk et al. (1987) and Lee et al. (1990) used compass walking and the divider method. Later, Den Outer et al. (1995) and/or Kulatilake et al. (2006) have identified these approaches as being inadequate of capturing the self-affine nature of rock profiles. Nonetheless, this did not prevent the use of these approaches thereafter (e.g. Bae et al., 2011). Moreover, the impracticality of the methods has not been shown thoroughly but was rather argued solely on a theoretical basis. Consequently, compass walking is the method used most frequently in the context of roughness evaluation (c.f. Li and Huang, 2015). Apart, correlating the compass dimension of the type-profiles with JRC works just fine. Therefore, in this study compass walking is also analysed for comparative reasons.

In the already mentioned, most recent work by Stigsson and Mas Ivars (2019) an important fact is underlined: fractal calculation schemes are meaningful only if an ad-

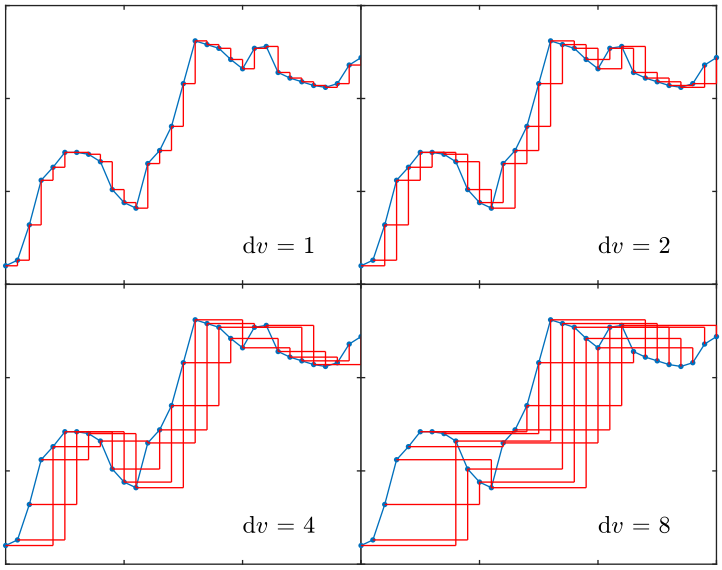

Figure 3.3: Concept of RMS-COR method

ditional magnitude parameter is incorporated. Magsipoc et al. (2020) recognized this simultaneously, identifying power spectral density and the root-mean-square correlation method (RMS-COR) as being eligible for roughness characterisation. Consequently, possible correlations of fractal measures with JRC need another parameter apart from H or D to be fully constrained. Stigsson and Mas Ivars (2019) used RMS-COR and power spectrum analysis to produce H and an asperity measure, which they named $\sigma\delta h(\mathrm{d}x)$. The two variables were then linked to the JRC. Accordingly, RMS correlation and spectral analysis are used in this study.

Of course, besides the three approaches used in this study and described hereafter, other fractal methods for roughness evaluation exist (for example box counting). However, they all lack reasonable correlation with JRC and are therefore discarded here. What is meant by "reasonable correlation" will become clear in the following and is discussed later.

RMS-COR method With this method, the roughness of a profile is evaluated by using the variation of the distribution of height differences in dependence of spatial wavelength (Renard et al., 2006). For varying vertex intervals, $\mathrm{d}v$, a population of corresponding height differences, $\mathrm{d}h$, is acquired as depicted in Figure 3.3. Then, the standard deviation of the height differences, $\sigma(\mathrm{d}h)$, for each vertex interval is calculated. By plotting $\sigma(\mathrm{d}h)$ versus $\mathrm{d}v$ in log-log space the Hurst exponent is received as the slope of the linear fit. A requirement for this technique is that the profile vertices are equally spaced. Additionally, the method rests upon height differences; therefore, the profiles must be free of possible overall trends.

An important aspect of the RMS-COR method is that the intercept of the linear fit line with the y-axis serves as a magnitude parameter for the profile. This value is necessary since the Hurst exponent only does not describe self-affine fractal entities distinctively (Magsipoc et al., 2020). In this study, the terminology from Stigsson and Mas Ivars (2019) for the magnitude parameter $\sigma\delta h(\mathrm{d}x)$ is used. Also, they introduced a correlation of H and $\sigma\delta h(\mathrm{d}x)$ with JRC which is given hereafter:

$$\mathrm{JRC} = -4.3 + 54.6 \cdot \sigma\delta h(1\mathrm{mm}) + 4.3 \cdot H \tag{3.4}$$

Equation 3.4 is valid for sampling intervals of 1 mm. As stated earlier, this should be the default for JRC determination. However, in case a different constant sampling interval dx is used $\sigma\delta h(1\text{mm})$ evolves from scaling $\sigma\delta h(\text{d}x)$ according to the following conversion:

$$\sigma\delta h(1\text{mm}) = \frac{\sigma\delta h(\text{d}x)}{(\text{d}x/1\text{mm})^{H}} \tag{3.5}$$

Furthermore, Stigsson and Mas Ivars (2019) stated that a shortcoming of the RMS-COR technique is an underestimation of H due to the natural finite length of profiles in general. To account for this effect, they constructed artificial profiles with pre-set Hurst exponents and asperity measures using an inverse Fast-Fourier-Transform algorithm. Subsequently, calculating H with the RMS-COR method yielded systematically lower Hurst exponents for profiles having a generated H of larger than 0.5. They applied a rule for compensation, however, not including it in their writing. Therefore, adopting their approach and data, the following correction equation was produced in this study, being valid for the RMS-COR method and being necessary in case the calculated Hurst exponent, $H_{\text{RMS,cal}}$, is larger than 0.5:

$$H_{\text{RMS}} = \ln\left(H_{\text{RMS,cal}}\right) + 1.18 \qquad \text{for } H_{\text{RMS,cal}} > 0.5 \tag{3.6}$$

Power spectrum analysis Predominantly in tectonophysics power spectral analysis using the Fast-Fourier-Transform (FFT) is often applied for the evaluation of roughness of rock joints and faults (e.g. Candela et al., 2009; Bistacchi et al., 2011; Corradetti et al., 2017). FFT algorithms convert the spatial information of the profile to the frequency domain. By plotting the associated power versus each length frequency in log-log space, the Hurst exponent is received as the slope of the linear fit. Additionally, the asperity measure $\sigma\delta h(\text{d}x)$ can be calculated using H and the intercept with the ordinate of the linear fit together with an evolution of sine waves according to the frequency spectrum of the profile (see Stigsson and Mas Ivars, 2019). To calculate JRC Equation 3.4 can be used which is also applicable to H and $\sigma\delta h(\text{d}x)$ inferred from power spectral analysis.

As for the RMS-COR method, with spectral analysis discrepancies exist concerning the calculation of the Hurst exponent using FFT for fractal lines of known H. Here, an overestimation was seen and Stigsson and Mas Ivars (2019) introduced another equation for compensation purposes:

$$H_{\text{FFT}} = 0.616 \cdot \ln\left(H_{\text{FFT,cal}}\right) + 0.92 \qquad \text{for } H_{\text{FFT,cal}} > 0.7 \tag{3.7}$$

Compass walking The procedure is essentially an approximation of the length of a profile through a chain of circles in which each subsequent circle originates at the intersection of the previous circle with the profile. By repetition, a relationship is obtained between the various radii and the corresponding number of circles needed to cover the profile. Depending on the implementation, possible relics of the profile (parts not covered by circles) are neglected or incorporated in the analysis, the latter being valid for the algorithm that was implemented in this study. The slope of the linear fit to the data plotted in log-log space yields the fractal compass dimension D_{comp}. A visualisation of the technique is given in Figure 3.4.

The crucial setscrew in this approach is the compass radius. It is somewhat unclear which specific radii different authors used. However, Lee et al. (1990) provided some values. Coherently, their set of radii and their equation were used in this study. Their

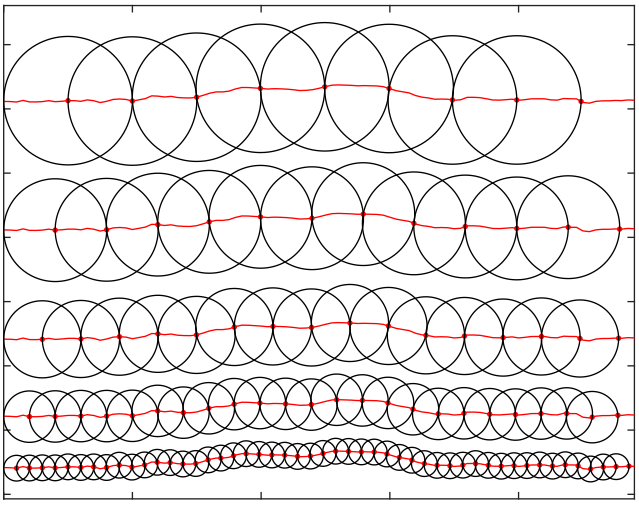

Figure 3.4: Concept of compass walking method

correlation reads as follows:

$$\text{JRC} = -0.87804 + 37.7844 \cdot \left(\frac{D_{\text{comp}} - 1}{0.015}\right) - 16.9304 \cdot \left(\frac{D_{\text{comp}} - 1}{0.015}\right)^2 \tag{3.8}$$

A disadvantage of Equation 3.8 is its quadratic, non-monotonic composition. The approach might be adequate for fitting the data of the type-profiles but if compass dimensions larger than 1.016738 are calculated erroneously low JRC would result (angular point of the equation). Therefore, the linear correlation from Turk et al. (1987) was also used. It is written in the following expression:

$$\text{JRC} = -1138.6 + 1141.6 \cdot D_{\text{comp}} \tag{3.9}$$

3.4 Re-Evaluation of the 10 type-profiles

One of the main problems with the existing JRC correlations is the traceability of their creation. Often, neither the digitalisations of the type-profiles and pre-processing steps are given nor the input variables for the calculation of the specific roughness measures are revealed. Therefore, the importance of this information is demonstrated in the following by revisiting the type-profiles using the three available data sets and different input variables.

3.4.1 Statistical approaches

There are at least 10 different statistical parameters that have been correlated with JRC (see Li and Zhang, 2015). To greater or lesser extent, for the 10 type-profiles decent coefficients of determination were found for the specific parameters with JRC. On the other hand, for example Wang et al. (2019) stated that σ_i behaves approximately the same as Z_2. Overall, Z_2 is well established and used often, therefore, in Figure 3.5 its relations to the four statistical parameters mentioned above are shown. Apparently, λ is not correlated with Z_2. The reason for this could lie in its rudimentary formulation

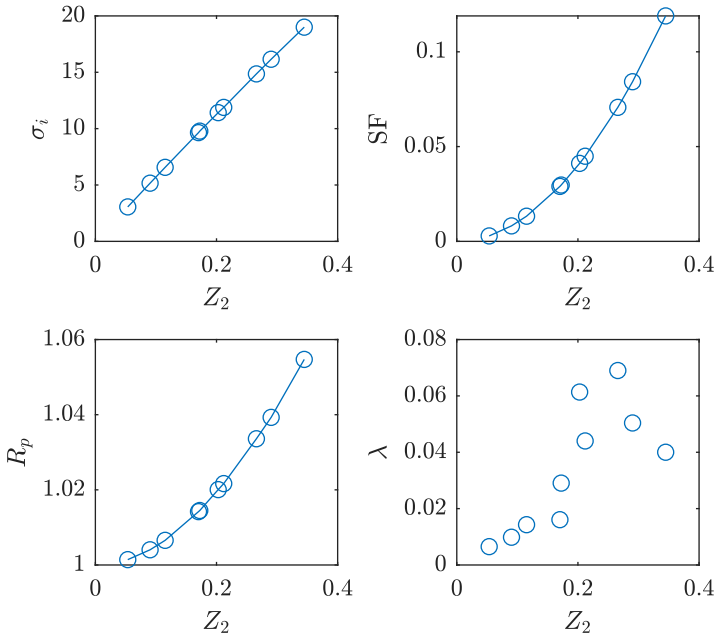

Figure 3.5: σ_i, SF, R_p and λ versus Z_2 for the 10 type-profiles (profile data from Tatone (2009))

Table 3.1: Transfer functions for σ_i, SF, R_p and λ to Z_2

Parameter	**Transfer function**	**Coefficient of determination**
σ_i	$\sigma_i = 54.79 \cdot Z_2 + 0.25$	$R^2 = 0.99$
SF	$\mathrm{SF} = (Z_2)^2$	$R^2 = 1.00$
R_p	$R_\mathrm{p} = 0.414 \cdot (Z_2)^2 + 0.0188 \cdot Z_2 + 0.9991$	$R^2 = 0.99$
λ	$\lambda = 0.0306 \cdot \ln(Z_2) + 0.0885$	$R^2 = 0.62$

in mathematical and physical terms, as it is only the ratio of the peak amplitude to the projected length of the profile. However, for σ_i, SF and R_p there exist precise transfer functions with coefficients of determination of $R^2 \approx 1$. The equations are given in Table 3.1. Consequently, σ_i, SF, R_p and Z_2 are interchangeable and Z_2 can serve as an agent for the four statistical parameters.

Common sense implies more or less similar numbers for Z_2 regardless of the digitalisation of the type-profiles as long as the initial sampling interval is close to 1 mm. However, this is not the case. In Table 3.2, the values of Z_2 exemplified again for the fifth type-profile according to each data set of Figure 3.1 and the used equations (Equations 3.1 and 3.2) are given in the second and third column. Note, that it has been common practice to use only the discrete form of Z_2 as of Equation 3.2. There exist no differences concerning the use of Equations 3.1 or 3.2 for the data from Tatone (2009) and Li and Zhang (2015). This is not surprising as for both data sets the original sampling interval is constant (as shown in Figure 3.2). However, for Stigsson and Mas Ivars' (2019) data a clear contrast is calculated. In order to use Equation 3.2 the data has to be equally spaced and their original data was interpolated according to the average sampling interval of 1 mm.

As stated earlier, Barton and Choubey (1977) employed a 1 mm sampling interval,

Table 3.2: Z_2 for type-profile JRC = 9.5

Data source	Original Data		Rotated and interpolated	JRC
	Eq. 3.1	Eq. 3.2		Eq. 3.3
Stigsson and Mas Ivars (2019)	0.2577	0.1866	0.1840	9.6
Li and Zhang (2015)	0.2073	0.2073	0.1758	9.1
Tatone (2009)	0.1937	0.1937	0.1724	8.9

which should therefore be the default for all JRC calculations. Additionally, Z_2 is a parameter that relies on the calculation of height differences between adjacent points. Hence, a horizontal datum line has to be established. Accordingly, in Table 3.2 the values for Z_2 are given also for the case that the trend is removed and that subsequently the rotated profile is interpolated at 1 mm sampling steps. The trend removal was achieved by performing a linear least squares regression and rotating the profile by the resulting overall slope angle towards the horizontal axis referred to as "simple detrending" hereafter. In detail, this pre-processing procedure results in a decrease of Z_2 in the amount of 0.0315 for the data from Li and Zhang (2015) and 0.0213 for Tatone's (2009) data. These numbers are numerically small; however, it must be considered that this change is significant since the whole range of Z_2-values for all 10 type-profiles is only 0.4. Consequently, the tailoring prior to calculation culminates in a change of 8% on the Z_2 scale. For the final JRC (far right column of Table 3.2) the variation decreases down to 4%, however, a maximal difference of 0.5 on the JRC scale prevails.

Therefore, it is of vital importance to follow certain pre-processing steps vigorously, namely trend removal and 1 mm sampling, to receive comparable results for the same profiles from differing data sets. The effect of doing so is depicted for all type-profiles in Figure 3.6. In part a) and b) it becomes clear that pre-processing reduces the values of Z_2. The transformation of Z_2 into JRC applying Equation 3.3 is depicted in parts c) and d) of Figure 3.6. For the uncorrected data, JRC in excess of 20 are calculated. This contradicts the range of the type-profiles, which is marked with a rectangle in c) and d). Most importantly, correcting all data sets yields very good accordance of the curves and moves them to a reasonable range of JRC. This comparison leads to the conclusion that, if proceeded as mentioned above, analysing data originally gathered with sampling intervals close to 1 mm, Z_2 is insensitive to the input signal. This means that using Z_2 is a robust approach of calculating JRC.

3.4.2 Fractal approaches

RMS-COR method In Figure 3.7 the relationships for $\sigma(\mathrm{d}h)$ and $\mathrm{d}v$ are plotted for the 10 type-profiles. In this case, all possible numbers for $\mathrm{d}v$ are shown, ranging from 1 to 100 for a 100 mm profile sampled at 1 mm. It becomes visible that the progression of the curves is erratic for large vertex interval length $\mathrm{d}v$. To account for this unavoidable effect due to the natural finite length of the profiles, Malinverno (1990) proposed using only vertex intervals smaller than 20% of the total length L of the trace (dotted-dashed line in Figure 3.7). However, this number is too large to restrict all graphs to a more or less linear portion.

The influence of the vertex interval length on H_{RMS} and $\sigma\delta h(1\mathrm{mm})$ is illustrated furthermore in Figure 3.8. The three cut-off length for $\mathrm{d}v$ from Figure 3.7 are evaluated, namely 10, 15 and 20% of the total length of the profile. For comparison, the results from

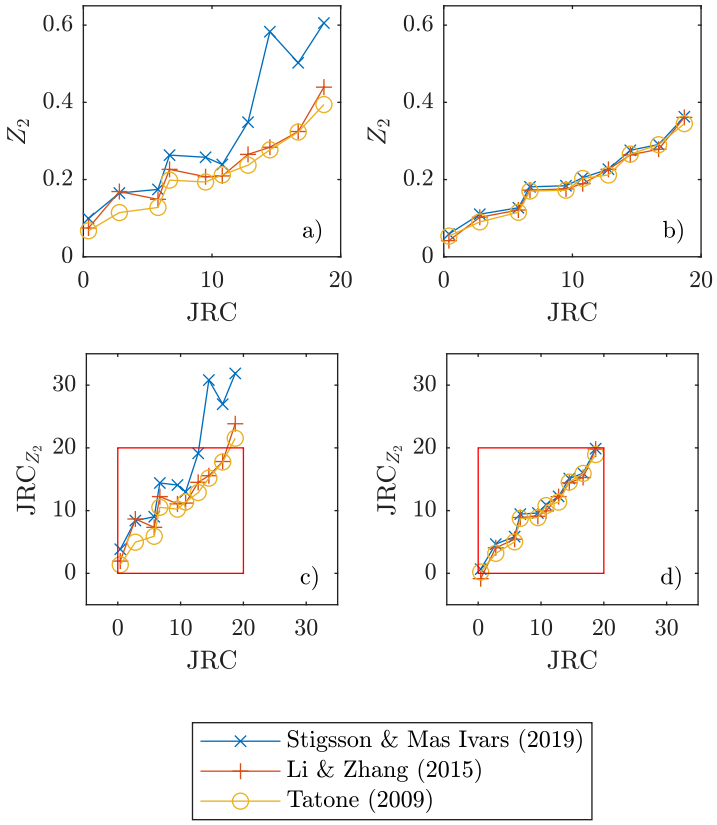

Figure 3.6: Influence of the input data and pre-processing in the Z_2 approach and deduced JRC for the type-profiles; a) and c) original data, b) and d) simply detrended and interpolated

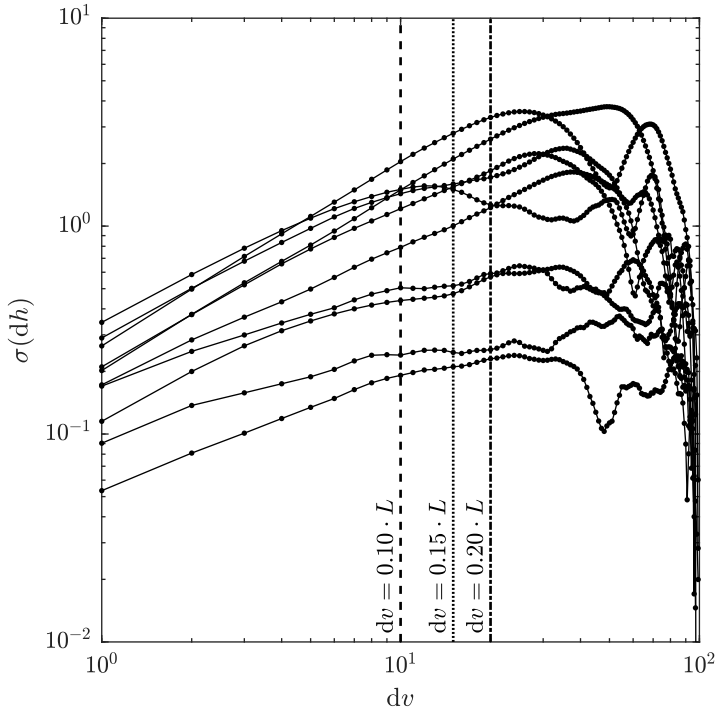

Figure 3.7: Finite length effect regarding the RMS-COR method for the type-profiles (profile data from Tatone (2009))

Stigsson and Mas Ivars (2019) were re-digitised from one of their graphs. The largest differences, both for H_{RMS} and $\sigma\delta h(1\mathrm{mm})$, are seen for $\mathrm{d}v = 0.2L$. Concerning the case of $\mathrm{d}v = 0.15L$ good agreement is achieved for H_{RMS}, however, for JRC larger than 15 differences occur for the asperity measure, $\sigma\delta h(1\mathrm{mm})$. Instead, a cut-off at a maximal vertex window of 10% of the total length excludes the first dents for most curves of Figure 3.7 and results in a good agreement with the reference data for $\sigma\delta h(1\mathrm{mm})$ in Figure 3.8.

Taking into consideration both Figures 3.7 and 3.8, in this study the vertex interval length $\mathrm{d}v$ was limited to 10% of the total profile length. This is reasonable regarding especially the relationship between $\sigma(\mathrm{d}h)$ and $\mathrm{d}v$ in Figure 3.7. Consequently, it leads to acceptable Hurst exponents and asperity measures regarding the only available comparative values. The discrepancies can be explained by divergent input data and by the fact that it is somewhat unclear which cut-off value for $\mathrm{d}v$ Stigsson and Mas Ivars (2019) used and, subsequently, what values they included in their linear fit of $\sigma(\mathrm{d}h)$ and $\mathrm{d}v$ in log-log space. Unfortunately, so far the procedure has not been fully described, considering all aspects necessary for reproduction. Therefore, in this study, the methodology applied has been fully disclosed.

As for the statistical measure Z_2 it is also important for the RMS-correlation method to assess its dependence on the data fed into the algorithm. From Figure 3.9 it becomes clear that for all three data sets of the type-profiles H and $\sigma\delta h(1\mathrm{mm})$ reach very similar values. Therefore, also RMS-correlation method is rather forgiving concerning imprecision during digitalisation. Note that the conclusions are drawn from detrended and interpolated input data, which is also a necessity for this technique as it operates with height differences of adjacent points on the profile.

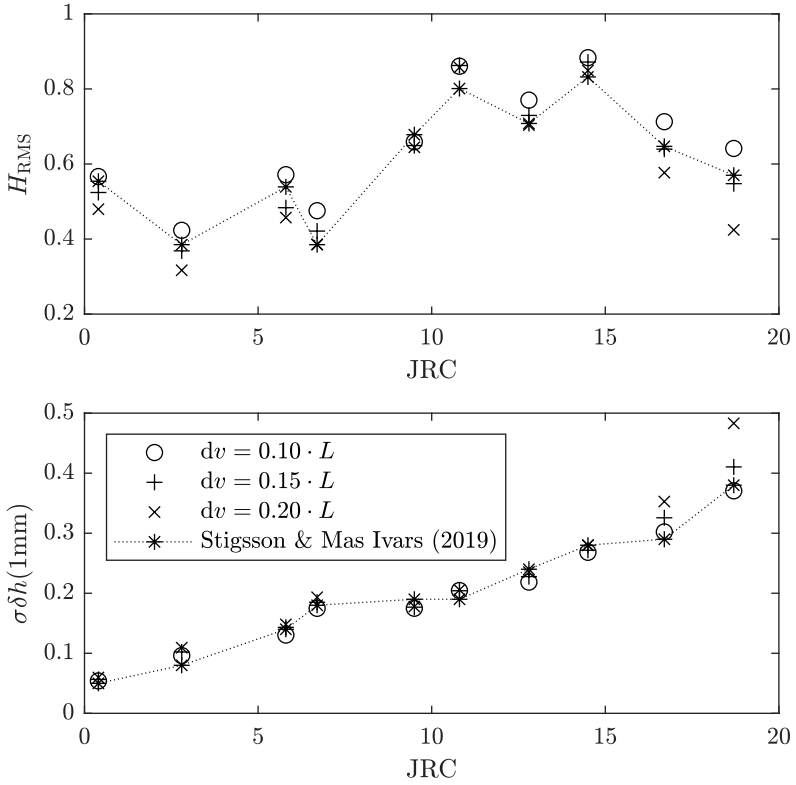

Figure 3.8: Influence of vertex interval length $\mathrm{d}v$ in RMS-COR method for the type-profiles (profile data from Tatone (2009))

Power spectrum analysis For the calculation of JRC from power spectral analysis Equation 3.4 can be used. However, it is important to realise that this correlation function was derived under consideration of only 64 vertices of each type-profile. Stigsson and Mas Ivars (2019) argued that the input signal length for FFT processing should be a power of two. In fact, it is only a question of speed of the particular algorithm: FFT is fastest for data lengths being powers of 2 and slowest for length values being prime numbers. However, most implementations of the FFT algorithm factorise the sample length thereby splitting up the transformation into manageable sub sets (being necessary really only if large data is analysed).

In this study, Matlab© was used in which the FFT is implemented according to Frigo and Johnson (2005). Their library is capable of dealing with whatever signal lengths and with non-periodic signals as well. Consequently, all points of the type-profiles can be considered. This is advisable since omitting 36% of data points in the already scarce population of the type-profiles produces large uncertainties.

Another issue in using Equation 3.4 in conjunction with the spectral approach concerns the pre-processing of the input signal. Stigsson and Mas Ivars (2019) applied a "vertical adjustment [of the profile vertices] to avoid artificial high power biases of low frequencies". This vertical adjustment is essentially a proportional linear reduction of the y coordinates according to the height difference over the full profile length. However, constricting the data in that way introduces bias in the high frequency range. Moreover, it directly effects the amplitude of the signal and therefore alters the asperity measure $\sigma\delta h(\mathrm{d}x)$. From a practical point of view keeping pre-processing of the input signal to a minimum seems reasonable as it avoids possible introduction of errors. The

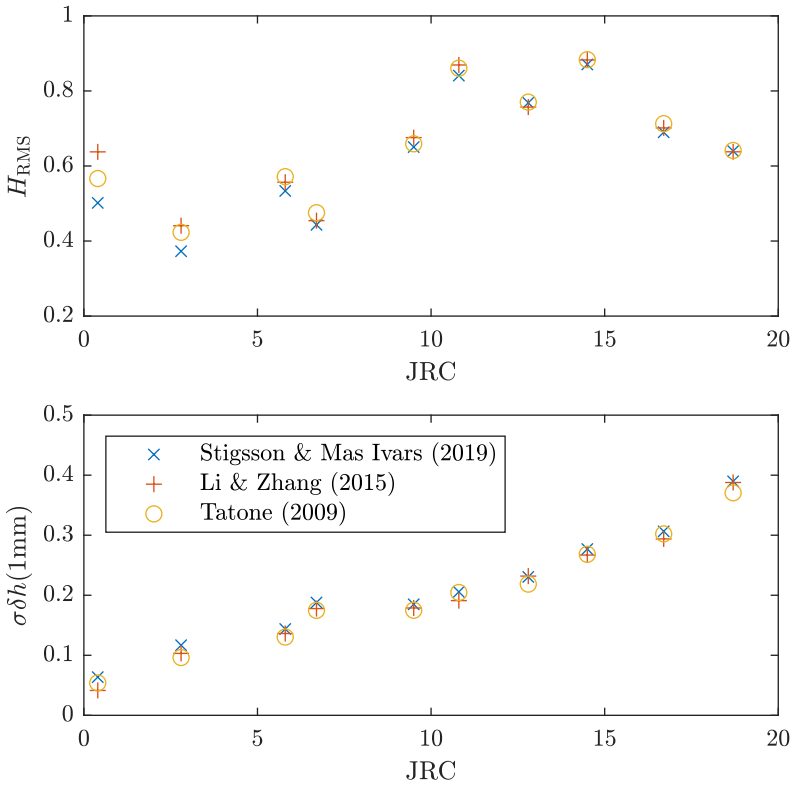

Figure 3.9: Influence of the input data in the RMS-COR method for the type-profiles ($\mathrm{d}v = 0.1L$)

scope should be to implement simple and safe routines to infer JRC. Therefore, the type-profiles are re-evaluated using FFT but this time applying it to the same input signals as for the other methods. Consequently, all available data points from the type profiles are considered which were simply detrended and which were sampled coherently at 1 mm intervals.

The effects of simple detrending versus vertical adjustment are plotted in Figure 3.10. By definition, Equation 3.4 is suitable to produce JRC from spectral analysis and from RMS-correlation. This implies that more or less equal numbers for H and $\sigma\delta h(1\mathrm{mm})$ should result irrespective of the two methods. For the case of vertical adjustment of the input signal, depicted in c) and d) of Figure 3.10, noteworthy differences evolve compared to the values generated with RMS-COR (dashed line in Figure 3.10). However, attention must be payed to the fact that in order to reproduce Stigsson and Mas Ivars (2019) data for FFT the first ten segments of a 100 mm profile containing 64 vertices have to be analysed and from that population, the one with the maximal asperity measure is considered representative. However, in case the same and full, simply detrended input signal is used for FFT and RMS-COR, better agreement between the two methods is seen as in a) and b) of Figure 3.10. Most importantly, since the heights of the profile vertices are not tampered with the asperity measure accords to an acceptable degree for both methods, as visible from b) compared to d) of Figure 3.10. Consequently, when the whole length of the type-profiles (100 mm) is considered compensation as of Equations 3.6 and 3.7 is not necessary in order to obtain similar results with FFT and RMS-COR.

In fact, the introduction of the compensation Equations 3.6 and 3.7 presupposed that using an inverse Fast-Fourier-Transform (and consequently a spectral approach) is ac-

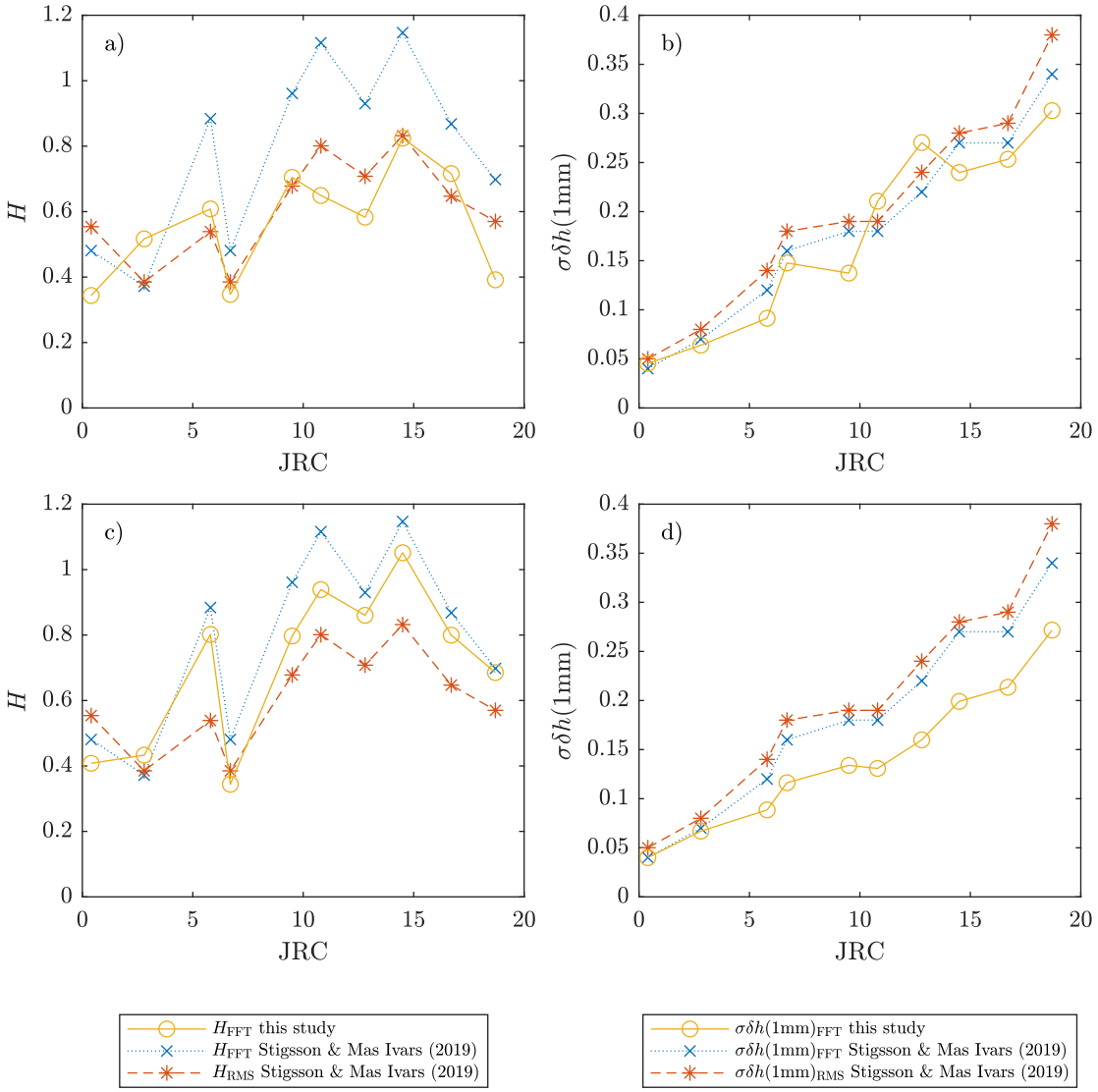

Figure 3.10: Influence of pre-processing on H and $\sigma\delta h(1\text{mm})$ calculated using FFT: a) and b) simple detrending, c) and d) vertical adjustment (profile data from Tatone (2009))

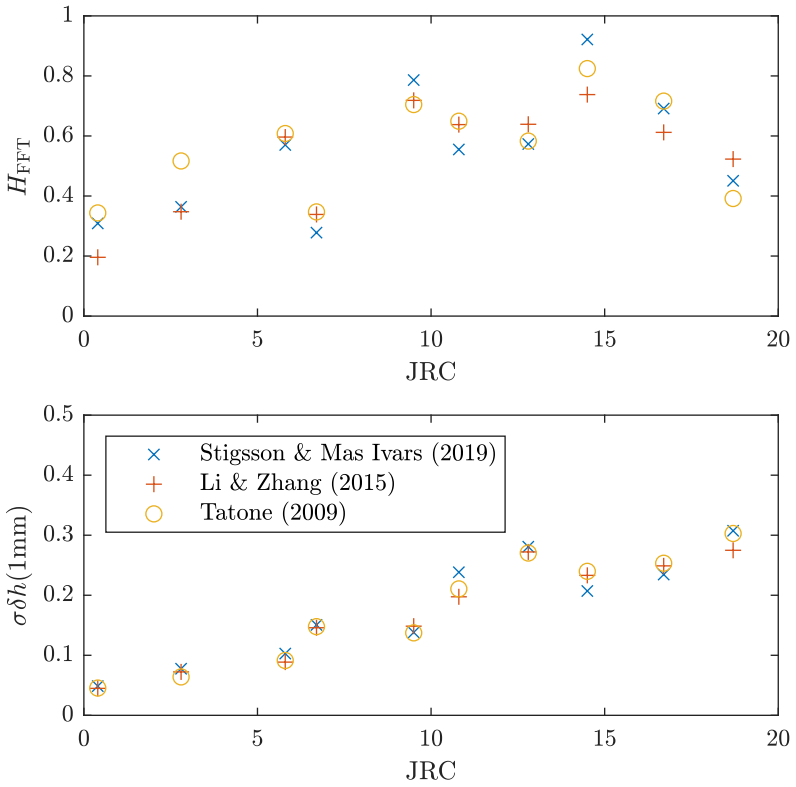

Figure 3.11: Influence of the input data in the power spectrum method for the type-profiles (simple detrending)

ceptable to produce the reference profile. Indeed, RMS-COR is a different mathematical algorithm relying on height differences between points and, therefore, it leads to divergent results. However, the finite length effect can be coped with by limiting the vertex interval length dv to 10 percent of the profile length, as explained earlier, and a "correction" of H as of Equation 3.6 seems to be not necessary. In case of Equation 3.7 the situation is even more inconsistent. From a theoretical point of view, a compensation should be unnecessary, however, for a fractal line, which is produced using an inverse FFT, the forward application of that algorithm results in different values of H. Once more, these contradictions illustrate the complexity of fractal approaches.

To enable comparison of the calculation methods also the sensitivity of the power spectrum analysis to the input is investigated. The calculated values for H and $\sigma\delta h(\mathrm{d}x)$ are depicted in Figure 3.11. The differences in the asperity measure are small. However, for the Hurst exponent even the datasets from Li and Zhang (2015) and Tatone (2009) show considerable differences although they have similar constant sampling intervals. Therefore, compared to Z_2 and RMS-COR methods the spectral approach is sensitive to the input signal.

Compass walking With this method, the pivotal choice to be taken involves the set of radii. The upper part a) of Figure 3.12 shows the recalculated compass dimensions for the type-profiles for the case that Lee et al.'s (1990) set of radii is used (r=2, 4, 6, 8, 10 mm) and for the case Turk et al.'s (1987) parameter set (r=2, 6, 20, 60 mm) is used. Additionally, another set of radii containing five values spaced equally on logarithmic scale from 1 to 15 mm was introduced. It must be emphasized that although the latter set is perfectly

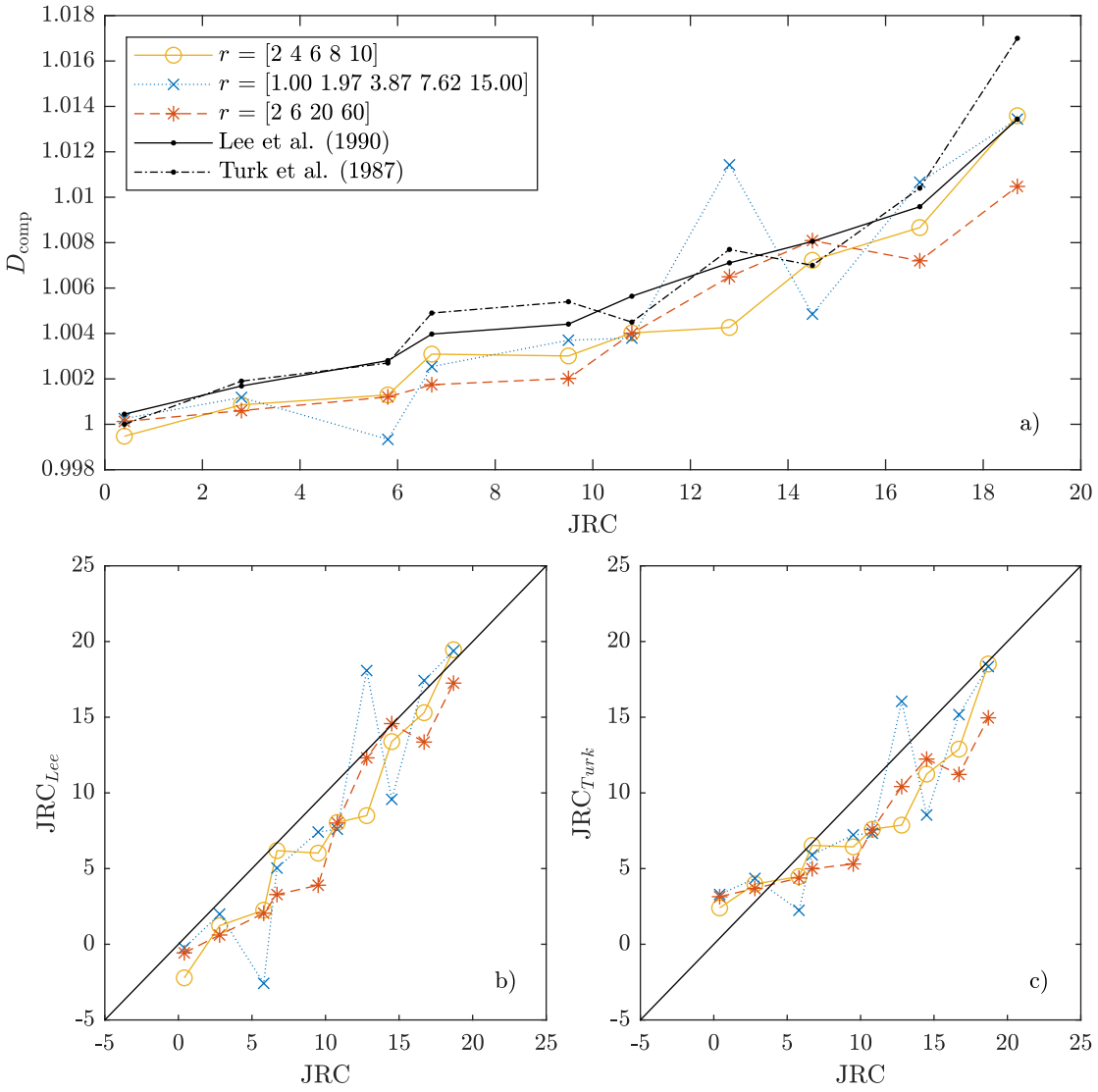

Figure 3.12: Influence of the radii on the compass dimension D_{comp} and JRC (profile data from Tatone (2009))

reasonable, as its values are larger than the sampling interval of the profile, smaller than the profile length and it falls in the range of prior works, large differences occur. For type-profile 7 discrepancies in excess of 0.007 points on the scale of D_{comp} result. This transfers into an enormous contrast of 9.6 for the JRC when Equation 3.8 is used (part b) of Figure 3.12) and amounts to 8.2 JRC-points when equation (3.9) is utilised (part c) of Figure 3.12). For the other type-profiles also divergence appears according to the set of radii used. Consequently, the technique is sensitive to the choice of compass radii. Furthermore, Figure 3.12 illustrates the dependence of the compass walking method on the input data as, obviously, other profile data than the original from the authors of the equations was used (in this case from Tatone, 2009). Finally, irrespective of the three different sets of radii applied here, in general, with both correlations an underestimation of JRC emerges as most points lie beneath the 1-1-line (part b) and c) of Figure 3.12).

Overall, fractal dimension determined by compass walking is in either case disputable for rock profiles. Especially the question of defining meaningful compass

radii made Schmittbuhl et al. (1995) to advise against the use of this method. Regardless, the method functions well in the sense that D_{comp} correlates with JRC for the type-profiles. Therefore, for comparative reasons and due to its broad use, compass walking is also assessed in this study. In order to being able to make use of Lee et al.'s (1990) correlation, coherently, in this paper, their set of radii, namely r equalling 2, 4, 6, 8, 10 mm, is used.

3.5 Application to a dataset of natural surface traces

Most information mentioned afore refer to the type-profiles. In case specific prerequisites are appreciated, exercisable techniques exist to closely calculate the given JRC values from the geometry of the profiles. Obviously, as all correlations reference to the "same" 10 type-profiles very similar JRC are determined irrespective of the calculation method. But is this also valid for non-standard profiles? In this section, that question shall be elucidated by analysing profiles extracted from three-dimensional models of natural rock surfaces.

3.5.1 Data acquisition and handling

To produce the surface models the rock samples were scanned using a GOM ATOS structured light scanner. The resulting representations feature a volumetric average RMS of residuals of 40 μm based on having scanned spherical markers under the same conditions and within the object space of the rock samples. In Table 3.3, the resolution of each sample is listed. The device used is a highly capable metrology system that can be considered a standard in the industry. According to Marsch et al. (2020), consequently, the surface models produced with this procedure are trustworthy and useful in rock roughness evaluation.

Also, in that prior publication, a routine was established in which all possible standard-length profiles on a surface mesh can be extracted. In the procedure, which is also applied in this study, height information is sampled with the sliding window method, simulating an imaginary profilometer of 100 mm length that traces the mesh in a user-defined raster, in this case 1 mm x 1 mm whereas the actual sampling interval amounts to 0.1 mm. By doing so, a large quantity of profiles can be gained. All profiles are pre-processed individually (trend-removal) and then evaluated according to the methods explained earlier. This course of action is reasonable since it overcomes the usual randomness of measuring only one profile that is then said to be representative for a surface. Moreover, scale effects are avoided as the length of the extracted profiles conforms to the length of the type-profiles.

3.5.2 Rock samples

Depending on the formation regime rocks develop different textures and consequently different roughness characteristics. Hence, upon evaluation of the universal validity of a theory, it is advisable to consider samples from all three main rock classes, namely igneous, metamorphic, and sedimentary rocks. As in this study, statistical and fractal calculation routines are compared, that are solely based on geometry, it is unimportant which specific rock material is used if the selection of surfaces covers the whole range of possible JRC from 0 to 20. Consequently, the full bandwidth of roughness profiles starting with smooth appearances and ending at rough progressions must be analysed.

For this study, a collection of quarry stones was gathered to then manually introduce fresh tensional fractures into the rock blocks. That way the fracturing process is very much constrained and controllable. The resulting surfaces were presented to a group of five engineering geologists which were asked to select denominations according to the ISRM (1978). The roughness categories were assigned considering the whole laboratory size sample and therefore depict the small-scale roughness or unevenness. The average subjective assessments are given in Table 3.3. Note that the classification is by no means objective and the list shall only give a general impression of the surfaces. For a closer look and further personal analysis, the surface meshes are also accessible in the repository to this study (see Marsch, 2020).

Table 3.3: Samples used in this study

Sample	**Model resolution** $[pts/mm^2]$	**Length/Width** $[mm]$	**Category according to ISRM (1978)**
Basalt, B	47.6	178 / 113	I—rough stepped
Granite, G	51.3	172 / 95	II—smooth stepped
Limestone, K	60.5	170 / 116	IV—rough undulating
Schist, SF	55.0	170 / 103	V—smooth undulating
Sandstone, SI	55.2	162 / 112	VII—rough planar
Sandstone, SS	53.2	166 / 104	IV—rough undulating

3.5.3 Results

The inference of JRC from statistical and fractal parameters obviously involves a mathematical transformation. As discussed earlier, the correlation functions incorporate assumptions and findings of the particular authors, which consequently add another level of complexity and uncertainty. Therefore, as a first step, the plain statistical and fractal values are examined.

Analysing the rough limestone sample K, in Figure 3.13 the standardised histograms of the statistical parameters Z_2, SF, σ_i, R_p and the distributions of D according to the three methods for the determination of the fractal dimension are given. Note that the fractal distributions of course have not been standardised since they are theoretically of the same unit and scale. As expected, the z-scores for the four different statistical parameters are quite similar. Consequently, as a general approximation, these measures are also interchangeable just like for the type-profiles. However, concerning the fractal approaches, large discrepancies become visible. The compass dimension D_comp exhibits a colossal peak at around one but shows a large range of values due to extreme outliers. Hence, compared to the other methods, the compass dimension is rather indistinctive on the scale of D as it concentrates around unity. Yet, for roughness profiles, according to the theory, the fractal compass dimension should lie between one and two (c.f. Hastings and Sugihara, 1994). Indeed, profiles from more or less homogenous planer smooth surfaces would yield a low compass dimension of close to one, however, sample K has an undulating rough appearance. Taking a closer look at the values of D from the RMS-correlation method and the spectral analysis leads to the conclusion that they do not accord. In agreement with the theory, the values of D_RMS are very well situated between 1.1 and 1.5. Instead, D_FFT shows a wider range and unrealistic values below unity. These facts gain importance since the same correlation function (Equation 3.4) is suggested to

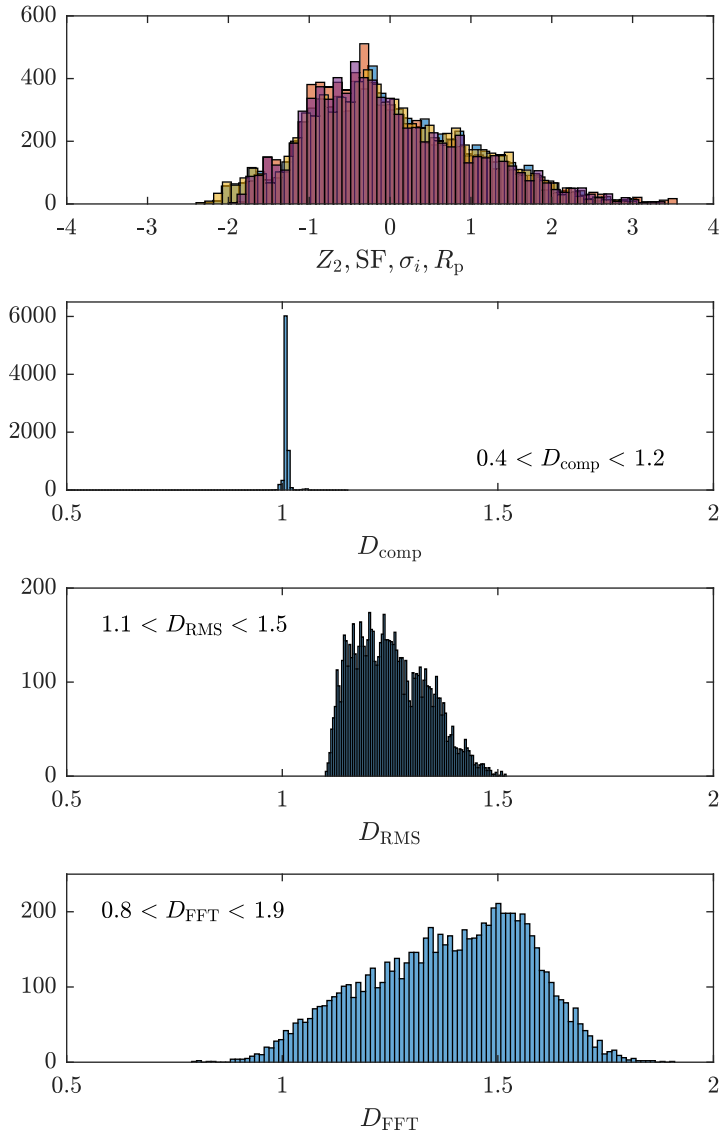

Figure 3.13: z-Scores of the statistical values and histograms of the fractal approaches, exemplified for sample K

be used for both methods to infer JRC. In general, the distribution of the fractal dimension D is evidently very much depended on the specific determination routine. Additionally, when comparing the statistical with the fractal histograms no definite similarity of the distributions can be found. Most importantly, not only for sample K, but also for all other samples used in this study the findings above are valid.

Remember, as a requisite due to referencing of all correlations (statistical or fractal) to the 10 type-profiles, for any other profile as well, irrespective of the particular calculation approach, the same JRC should result. Consequently, JRC from fractal approaches versus JRC from statistical approaches ought to plot on the bisecting line. For all samples used in this study, these graphs are given in Figure 3.14. Here, the inference of JRC from statistical approaches is represented by using Z_2, plotted on the abscissa.

There is some information that can be generalised from all samples. First, the fractal JRC values calculated according to Lee et al.'s (1990) Equation 3.8 using D_comp show a

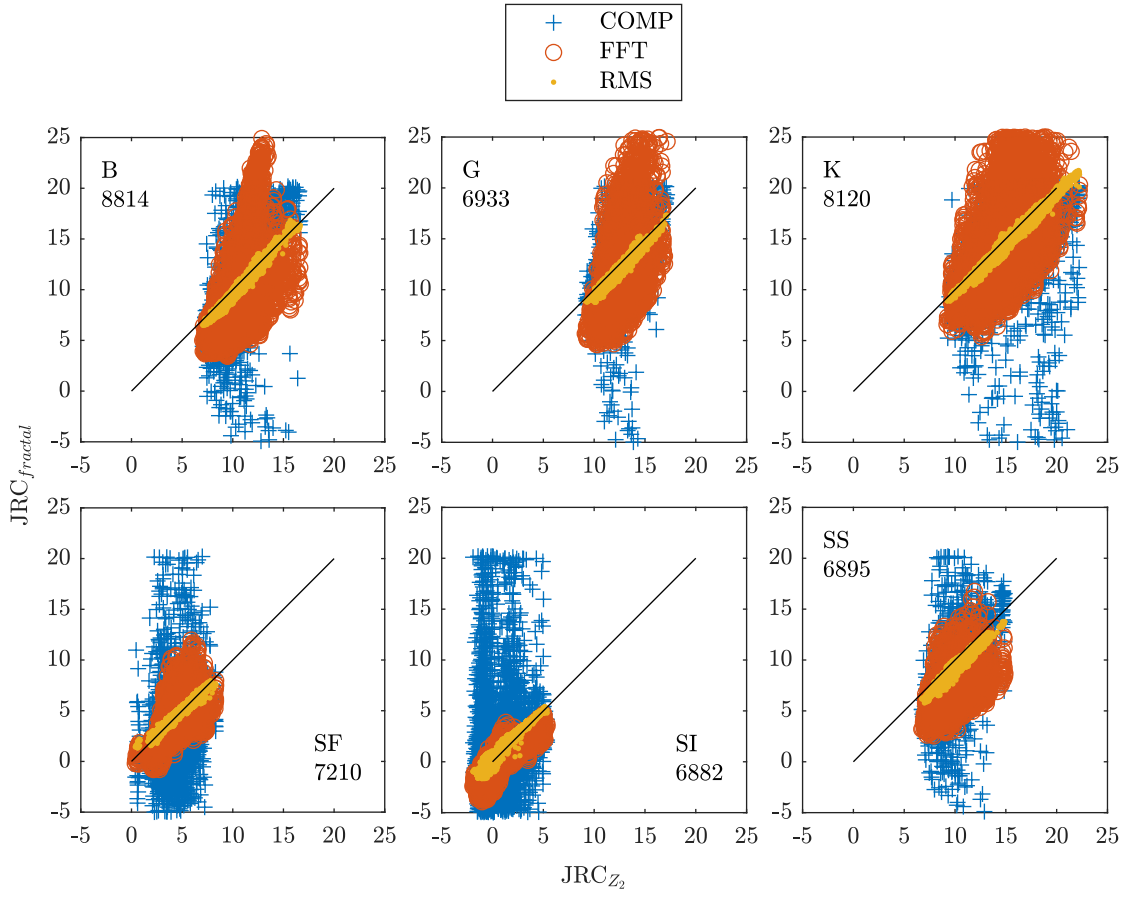

Figure 3.14: Statistical versus fractal JRC (inset: sample name and total number of profiles analysed), simply detrended profiles

large divergence from equality with the statistical JRC. The variation is enormous and always covers more than the regular range of JRC values of 0 to 20. Hereby Equation 3.8 delivers JRC smaller than zero regardless of the ISRM roughness category of the particular surface. Secondly, concerning the JRC inferred from spectral analysis, the graphs are diverse. For the undulating smooth sample SF and the planar rough sample SI, smaller discrepancy with the statistical JRC is seen compared to the other samples (still, the JRC values do not accord well). Apparently, the spectral analysis works better with surfaces that do not show large height differences or, stated otherwise, that show low variation and low amplitudes. Conversely, this underlines the critical issue within the spectral analysis of defining the asperity measure. By any means, the variation of $\mathrm{JRC}_{\mathrm{FFT}}$ is large and spans a range of at least 12.5 JRC-points (sample SS). Lastly, JRC determined with the RMS correlation method coincide with JRC_{Z_2}. For practical application, the divergence from the 1-1-line is negligibly small. This applies to all samples. Notice here that the data was not transformed (Equations 3.6 and 3.7) following the results of the re-evaluation of the type-profiles.

Regarding only the type-profiles it was shown before that simple detrending is sufficient also for the use of the spectral analysis method to achieve acceptable results. However, the large variation of $\mathrm{JRC}_{\mathrm{FFT}}$ in Figure 3.14 suggests that this is not the case for profiles other than the type-profiles. Especially in the samples B, G and K large steps are present. Consequently, extracted profiles that incorporate these steps are discontinuous in the sense that the height difference between the ends of the profiles is large. This lack of periodicity will result in spectral leakage and therefore biased values for H and $\sigma\delta h(\mathrm{d}x)$ will be obtained. In order to eliminate this effect, the profiles were additionally vertically adjusted, and the outcomes are given in Figure 3.15. Tapering the profiles removes almost all $\mathrm{JRC}_{\mathrm{FFT}}$ above the 1-1 line from the population (c.f. Figure 3.14). However, the variation of JRC from spectral analysis remains large and the values bulge under the bisecting line. Consequently, this time the JRC is underestimated compared with the use of RMS-COR or Z_2. In case Equation 3.7 was used to additionally reduce H_{FFT}-values the differences would even increase. In summary, this underestimation is contradictive to the analysis of the type-profiles where the Hurst exponents based on the power spectrum systematically exceed the H-values from RMS-COR method.

To make use of correlation functions for JRC in general, it was argued before that it is important to follow the procedures of the originators as close as possible. Therefore, a third case must be considered for using power spectral analysis with the six surfaces. As Stigsson and Mas Ivars (2019) used only the window of 64 vertices of the type-profiles with the largest asperity measure considering the first 10 vertices for their correlation, a similar procedure was used here. The rationale for this is that during direct shearing sample halves would most likely adhere to large steps of the surface. Therefore, these irregularities should be included in the roughness calculations. In this study, at first, the starting 65 vertices were taken from the 100 mm long profile. This window was then simply detrended and vertically adjusted and reduced to 64 points. Secondly, the procedure was repeated on the subsequent 65 vertices and so forth. Finally, the combination of the Hurst exponent with the largest asperity measure from the group of 35 pairs was said to be representative for the standard-length profile. The results are shown in Figure 3.16. For all samples, the values of $\mathrm{JRC}_{\mathrm{FFT}}$ were elevated compared to Figure 3.15 and now gather around the bisecting line. However, the large variation persists and for sample K, $\mathrm{JRC}_{\mathrm{FFT}}$ even extends to values greater than 20. As for the two other cases, also with this processing divergent results are obtained upon usage of spectral analysis.

However, the close agreement between $\mathrm{JRC}_{\text{RMS-COR}}$ and JRC_{Z_2} for all three pre-

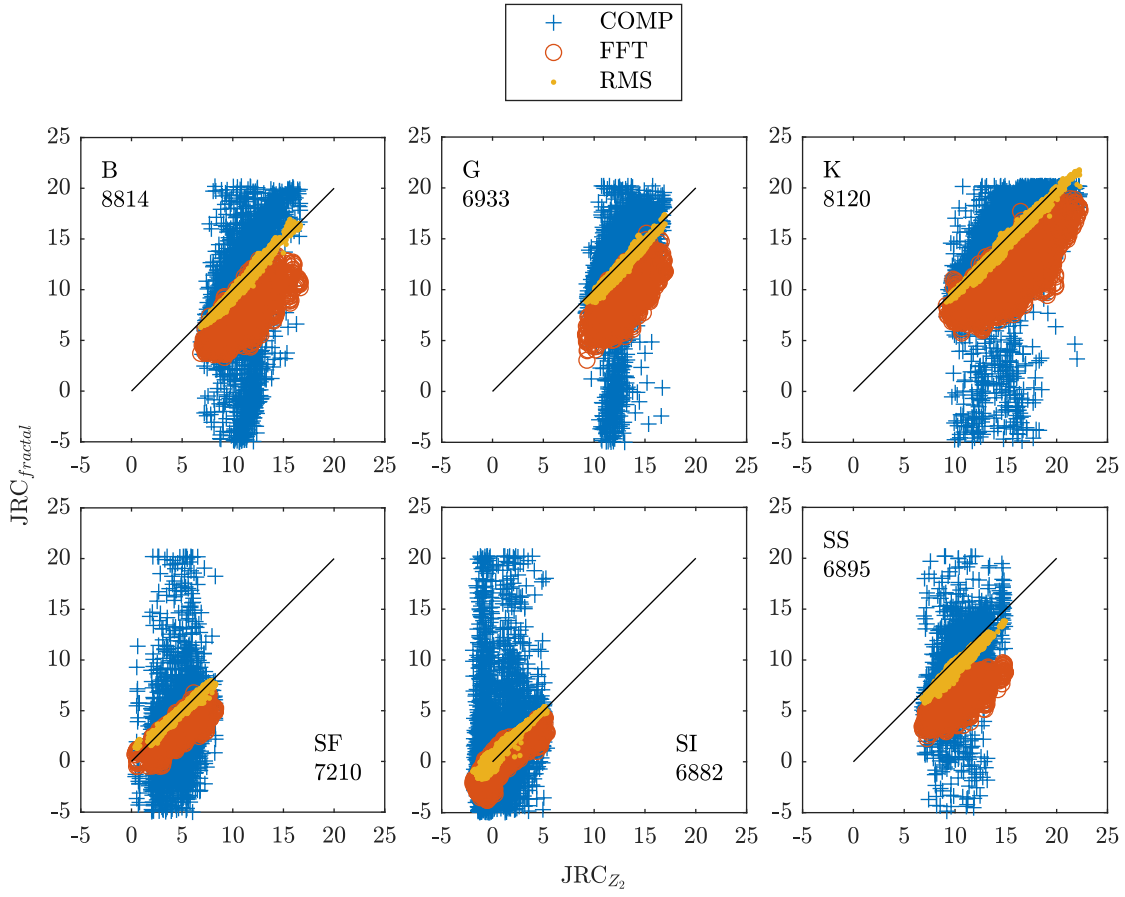

Figure 3.15: Statistical versus fractal JRC (inset: sample name and total number of profiles analysed), vertically adjusted profiles

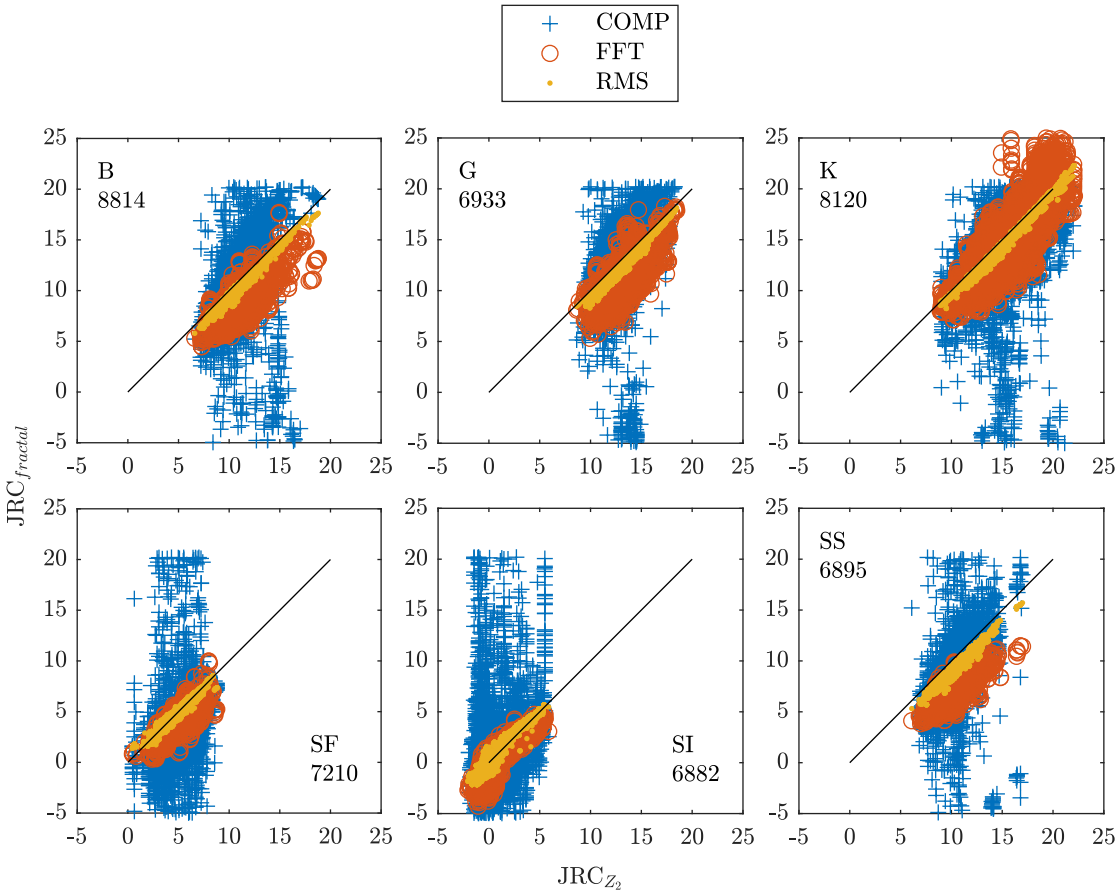

Figure 3.16: Statistical versus fractal JRC (inset: sample name and total number of profiles analysed), vertically adjusted profiles and window of 64 vertices with largest $\sigma\delta h(1\text{mm})$ per profile considered

processing cases is somewhat striking since the RMS-Correlation method is rather approximative due to the need of linear regression of $\mathrm{d}v$ and $\sigma(\mathrm{d}h)$ in log-log space. As stated earlier, fractal approaches need two parameters to be fully constrained. In Equation 3.4 the share of the asperity measure $\sigma\delta h(1\mathrm{mm})$ in the final JRC is more than a factor of 10 larger than the share of the Hurst exponent. Consequently, the JRC calculated by RMS-correlation or spectral analysis predominantly depends on the magnitude parameter. Therefore, for a closer analysis $\sigma\delta h(1\mathrm{mm})$ is plotted versus Z_2 in Figure 3.17. Most obviously, the scatter of $\sigma\delta h(1\mathrm{mm})$ deduced from spectral analysis is large but instead, in the case of RMS-COR a higher degree of similarity with Z_2 is obtained. In fact, for the special case of analysing profiles with 1 mm sampling steps the two measures $\sigma\delta h(1\mathrm{mm})$ and Z_2 must be equal. The asperity measure is defined as the sample standard deviation of the population of height differences of adjacent vertices, δh, for a profile of N points:

$$\sigma\delta h(\mathrm{d}x) = \sqrt{\frac{1}{N-1}\sum_{i=1}^{N-1}\left(\delta h_i - \bar{\delta h}\right)^2} \tag{3.10}$$

A prerequisite for the calculation of all roughness measures was that a possible overall slope is eliminated. Any procedure of detrending should result in $\bar{\delta h} = 0$. Consequently, Equation 3.10 reduces to:

$$\sigma\delta h(\mathrm{d}x) = \sqrt{\frac{1}{N-1}\sum_{i=1}^{N-1}\left(y_{i+1} - y_i\right)^2} \tag{3.11}$$

Under consideration of Equation 3.2 it becomes clear that Z_2 and $\sigma\delta h(\mathrm{d}x)$ are linked by the inverse of the distance between the vertices, $\mathrm{d}x$, reading:

$$Z_2 = \frac{1}{\mathrm{d}x} \cdot \sigma\delta h(\mathrm{d}x) \tag{3.12}$$

Now taking in mind that the concept of JRC estimation with the standard chart is valid for 1 mm sampling intervals only, in this particular case, Z_2 and the asperity measure are equal:

$$Z_2(1\mathrm{mm}) = \sigma\delta h(1\mathrm{mm}) \tag{3.13}$$

Consequently, all data points in Figure 3.17 should lie on the 1-1 line. Indeed, $\sigma\delta h(\mathrm{d}x)$ deviates from Z_2 for both RMS-COR and FFT methods. However, RMS-correlation surpasses the power spectrum approach in this matter.

3.6 Discussion

At first glance, it seems utterly simple to determine the JRC from profile traces: there exist the type-profiles as reference along with some statistical or fractal parameters and subsequently, one can calculate the JRC for whatever profile. A closer second look however reveals many pitfalls: how good is the original database for the correlations anyhow? Are the working hypotheses comprehensible? Are the calculation methods useful and forward-looking? Finally, how can the results be evaluated, and, do they cover the whole data range of possible JRC adequately?

First, when dealing with the idea of determining JRC by correlation functions based on the type-profiles, the following must be considered: roughness increases from top to

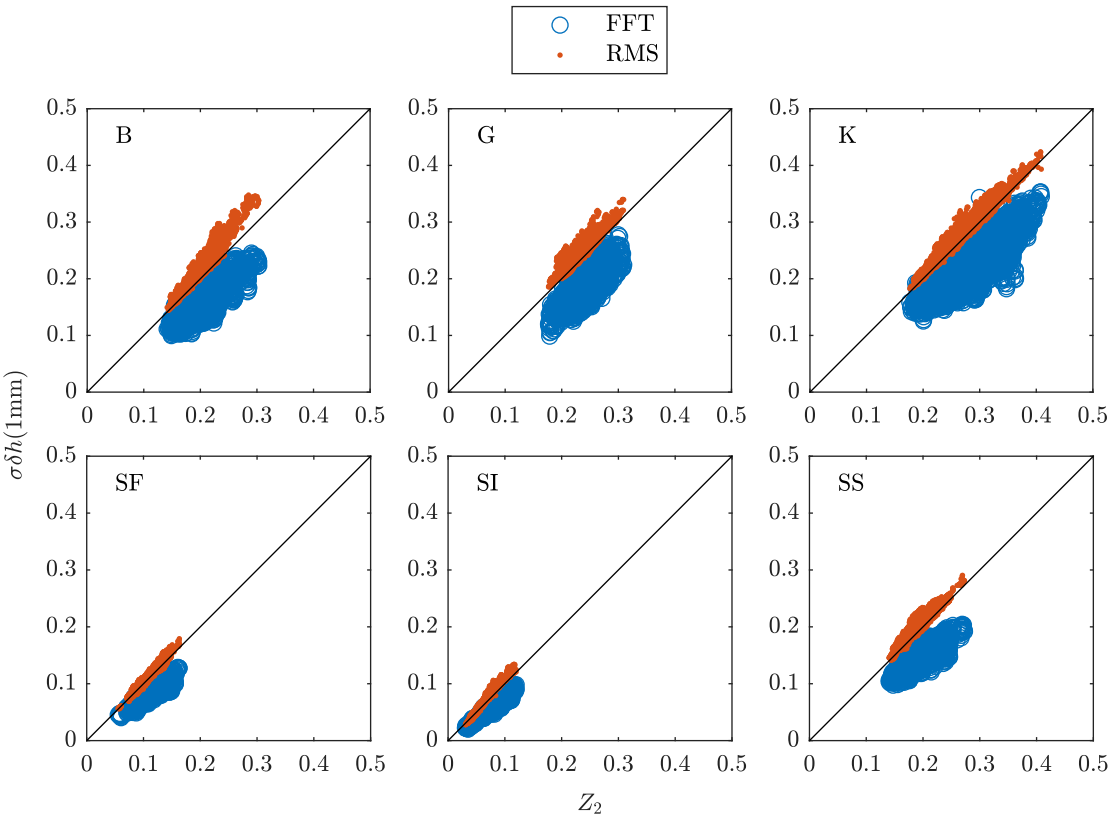

Figure 3.17: Asperity measure $\sigma\delta h(1\text{mm})$ versus Z_2, vertically adjusted profiles

bottom in the standard chart. Consequently, the predicted JRC must increase. This apparently ordinary observation is in no way trivial: it makes it imperative that any mathematical parameter (or set of parameters) deduced from the profiles can be fitted by a monotonic function (or even better strictly monotonic). This irrevocable, paramount matter of fact is visualised in Figure 3.18. As it is well-known, the statistical parameter Z_2 satisfies this requisite to the full extent without further input (cf. Figure 3.6 b)) whereas fractal approaches must yield at least two independent variables to meet this need (cf. Figure 3.8). This study pointed out the close relationship of the asperity measure $\sigma\delta h(1\text{mm})$ with Z_2. Indeed, these findings provoke the question of relevance concerning fractal approaches for JRC determination: why bother to calculate the Hurst exponent involving complex calculation routines to then scale that value with $\sigma\delta h(1\text{mm})$? Using H and $\sigma\delta h(1\text{mm})$ produces unneeded sources of error and adds unnecessary ramifications. Moreover, the influence of $\sigma\delta h(1\text{mm})$ on JRC in Equation 3.4 is one magnitude greater than the input of H. Consequently, Equation 3.4 is practically rather another statistical than a fractal correlation.

Undeniably, the visual nature of the type-profiles is of inferior quality. The information that can be gained from them is narrow. In fact, by revealing the effect of the sampling interval on JRC, Yu and Vayssade (1991) indirectly acknowledged the limitations of the standard chart. Therefore, re-digitalisation is useless and, at the latest, Tatone (2009), by sampling coherently in 1 mm intervals, squeezed out the best information. By far, his data suffices. Nevertheless, what was learned here from different data sets of the type-profiles is how sensitive specific calculation approaches are to the input signal. The robustness of the algorithms is absolutely essential before the back-

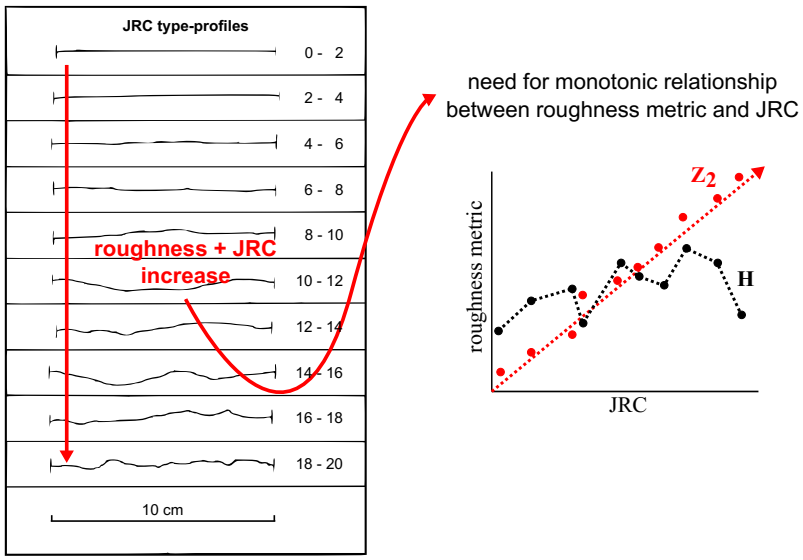

Figure 3.18: Need for monotonic relationship (profile chart redrawn from Barton and Choubey (1977))

ground that it is impossible to exactly reproduce a measurement with simple tools like the tactile profilometer. Even using modern 3D scanners will not produce an identical image of a surface repeatedly. Nevertheless, if the measured object does not change then the roughness metric should not change either, at least not that much. Having this in mind Z_2 and RMS-COR clearly outperform the FFT routine as they yielded similar results using different digitalisations of the type-profiles.

In their original work, Barton and Choubey (1977) stated that, preferably, JRC should be determined by direct shear testing. As a courtesy, they prepared the 10 type-profiles to provide engineers and geologists with a possibility to visually estimate JRC. However, over the past decades, opposed to the intended use of the type-profiles, researchers have driven correlating whatever measures with the type-profiles to the absurd, claiming to be able to calculate JRC to decimal places based on re-digitising the original data over and over again. This led to a situation in which a confusing amount of correlations exists that each time refer to a very particular data set of the, although identical, type-profiles. Moreover, divergent calculation schemes were applied and unfortunately, in most instances, they are poorly documented. Especially with fractal methods however, it is extremely important to provide all variables to guarantee a safe application by others. Consequently, there is a need for standardised procedures.

A more general issue concerns the small quantity of the type-profiles. Establishing a universally applicable theory on 10 data points may result in an extreme simplification. Dealing with natural, practically infinitely diverse matter, namely rock surfaces, demands a large database, at least to explore and prove the data distribution. Moreover, the application of extremely powerful algorithms to develop simple mathematical relationships based on so little input inevitably leads to overfitting. Additionally, there exist only few datasets for cross validation, of which some are given in Figure 3.19. Certainly, for the type-profiles an acceptable relationship exists between JRC back-calculated from mechanical tests and JRC calculated from Z_2 or RMS-COR. At least, eight pairs lie near the 1-1 line. However, a considerable variation of more than five JRC-points is seen for the data from Bandis (1980), Bandis et al. (1983) and Grasselli (2001). Apparently, surfaces that have similar geometrical characteristics, resulting in similar Z_2 or H and $\sigma\delta h(1\text{mm})$

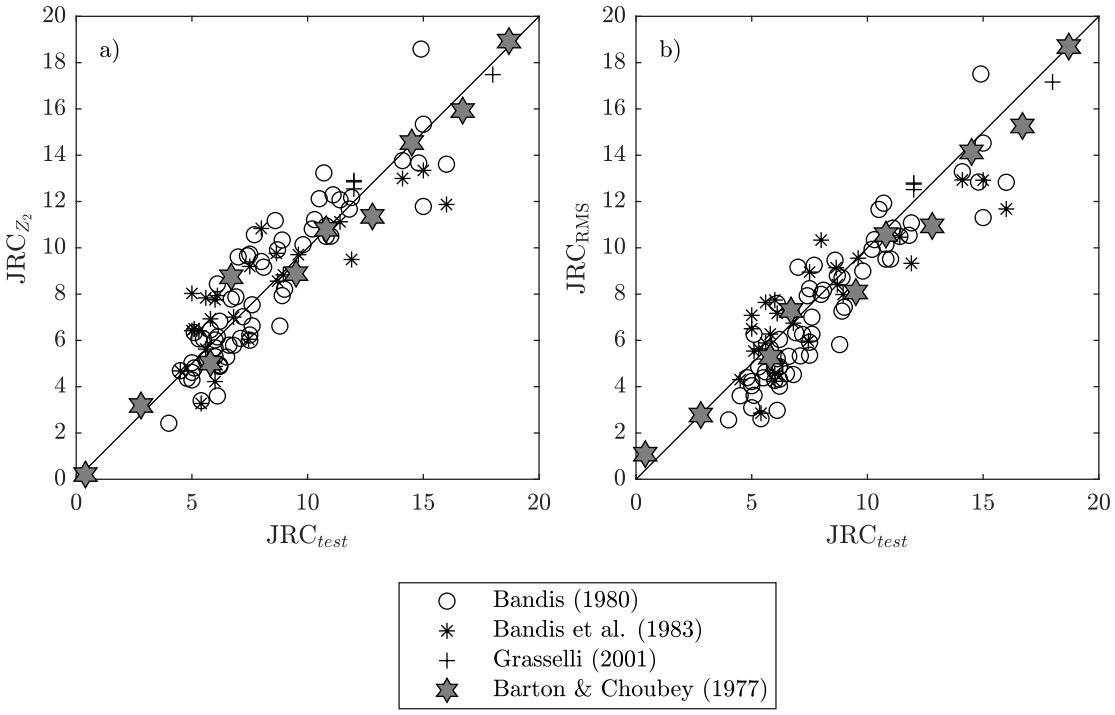

Figure 3.19: Relationship between back-calculated JRC and JRC inferred by geometrical means

and consequently similar JRC, yield different shear strength. The same holds for the reversed statement. However, the reason for the poor distribution in Figure 3.19 might lie in the selection of allegedly representative profiles from the surfaces, although, how this can be done objectively is beyond the scope of this study. Indeed, many different profiles could have been used as an agent for the surfaces in question (cf. Figure 3.13).

In summary, relying on the type-profiles only and repetitive fitting of more and more parameters to them does not help the case. The problem of roughness estimation from geometrical information must be placed on a larger foundation. Consequently, openly available more significant, preferably three-dimensional geometric data accompanied by results from direct shear tests are needed.

3.7 Conclusion

In this study, considerable efforts were made to compare different methods for determining the JRC from roughness profiles and to make their differences transparent. This allows a direct comparison of statistical and fractal methods between each other which is a novelty in the field of JRC evaluation. The focus of this study was to verify the hypothesis whether for any arbitrary profile the same JRC results irrespective of using statistical or fractal approaches and to denominate the most reasonable practice.

To do so, first, problems concerning the input data for correlations, namely the initial type-profiles, were discussed. The sparseness and low-resolution of the original data bring about unquantifiable uncertainties. The application of more and more complex mathematical routines and extensive parametrisation is not appropriate. The type-profiles should not be considered the axiomatic definition of JRC, but they are still a smart tool for estimation.

On these grounds, secondly, the accepted state-of-the-art mathematical methods to calculate reasonable statistical and fractal parameters have been described thoroughly, denominating and evaluating all input variables, and, thirdly, explaining their sensitivity by means of re-evaluating the type-profiles. All calculation routines and inputs used are available in the online repository to this publication (see Marsch, 2020). Of course, disclosing every variable and pre-processing step is an absolute necessity for comparability and quality assessment. Thereby, the following can be concluded:

- Z_2 can be used as an agent for statistical approaches,
- the input signals must be detrended and interpolated at 1 mm intervals,
- a cut-off length with RMS-correlation of $\mathrm{d}v = 0.1L$ should be used, and
- spectral analysis is sensitive to the input data.

Obviously, for the type-profiles all methods lead to similar JRC values. Therefore, in the last step of this study, a vast number of profiles was extracted from different rock surfaces to investigate the interchangeability of the calculation schemes. Based on the analysis of these profiles the following statements stand:

- compass walking is inapplicable to rock traces,
- spectral analysis is defective concerning the profile-based concept of JRC, and
- RMS-correlation accords well with Z_2.

Concerning spectral analysis and RMS-correlation, the inferred JRC heavily rely on the asperity measure. This applies to the approximation of JRC on 10-cm scale based on the type-profiles. However, clearly, the benefits of fractal approaches, being the determination of roughness on different scales and large areas, shall not be questioned.

Explicitly, thinking beyond the present type-profiles for JRC is advocated here. There exist to great of uncertainty in Barton and Choubey's (1977) original chart. The type-profiles should only be used for what they have been initially introduced, namely approximating JRC. Reporting JRC to decimal places suggests an accuracy that does not exist. The best the user can obtain from present correlations is the class of JRC.

Naturally, field engineers and practitioners want to apply routines safely. Therefore, offering suggestions on how to apply the concepts are required: using the simple measure Z_2 is good enough to determine the JRC from profiles as it is coherent with the well-meant, engineering-like standard chart. A suggested workflow for profiles of 10 cm length is given in Figure 3.20. This is the best practice from a present perspective having only the sparse and low-resolution original type-profiles at hand for referencing.

A critical point in determining JRC based on two-dimensional data is most certainly the selection or identification of representative profiles. Indeed, Barton and Choubey's (1977) type-profiles are not objective as they have been chosen for unreproducible reasons: "an attempt was [...] made to select the most typical profiles". However, this issue was not discussed in this study deliberately since direct mechanical shear tests would have been necessary to calibrate possible new sampling routines. For the future, the question needs to be addressed of how representative and more inclusive two-dimensional geometric input data can be sampled from shear surfaces in case three-dimensional parameters are unwanted. This could lead to objective and better correlations with JRC.

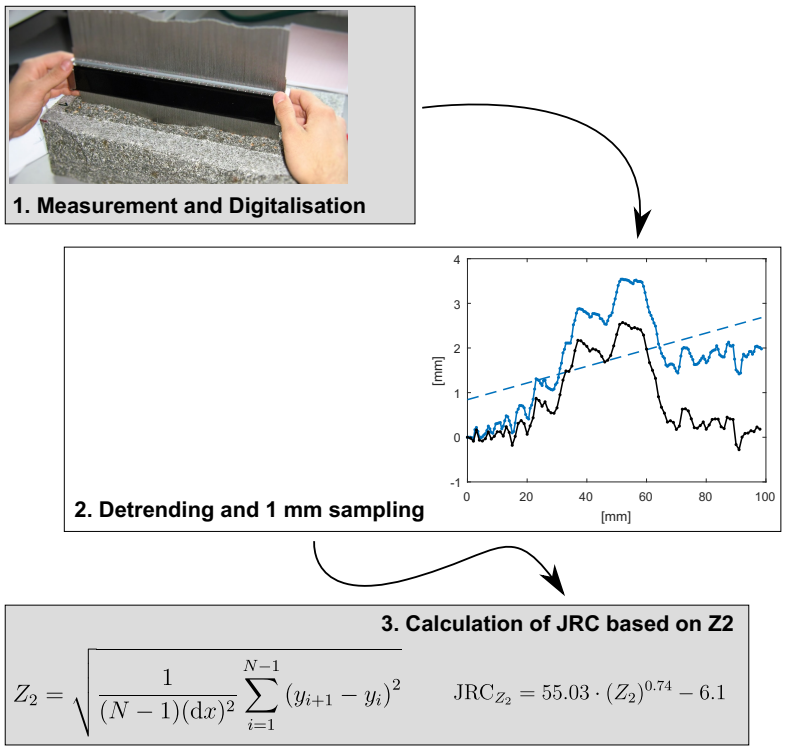

Figure 3.20: Good enough, simple workflow

3.8 References

Alameda-Hernández, P., Jiménez-Perálvarez, J., Palenzuela, J. A., Hamdouni, R. E., Irigaray, C., Cabrerizo, M. A., and Chacón, J. (2014). Improvement of the JRC calculation using different parameters obtained through a new survey method applied to rock discontinuities. *Rock Mech Rock Eng*, 47(6):2047–2060. https://doi.org/10.1007/s00603-013-0532-2.

Bae, D.-S., Kim, K.-S., Koh, Y.-K., and Kim, J.-Y. (2011). Characterization of joint roughness in granite by applying the scan circle technique to images from a borehole televiewer. *Rock Mech Rock Eng*, 44(4):497–504. https://doi.org/10.1007/s00603-011-0134-9.

Bandis, S. (1980). *Experimental Studies of Scale Effects on Shear Strength, and Deformation of Rock Joints*. PhD thesis, University of Leeds.

Bandis, S., Lumsden, A., and Barton, N. (1983). Fundamentals of rock joint deformation. *Int J Rock Mech Min*, 20(6):249–268. https://doi.org/10.1016/0148-9062(83)90595-8.

Barton, N. and Choubey, V. (1977). The shear strength of rock joints in theory and practice. *Rock Mech*, 10(1-2):1–54. https://doi.org/10.1007/bf01261801.

Barton, N. and de Quadros, E. F. (1997). Joint aperture and roughness in the prediction of flow and groutability of rock masses. *Int J Rock Mech Min*, 34(3-4):252.e1–252.e14. https://doi.org/10.1016/s1365-1609(97)00081-6.

Beer, A., Stead, D., and Coggan, J. (2002). Technical note estimation of the joint roughness coefficient (JRC) by visual comparison. *Rock Mech Rock Eng*, 35(1):65–74. https://doi.org/10.1007/s006030200009.

Bistacchi, A., Griffith, W. A., Smith, S. A., Toro, G. D., Jones, R., and Nielsen, S. (2011). Fault roughness at seismogenic depths from LIDAR and photogrammetric analysis. *Pure Appl Geophys*, 168(12):2345–2363. https://doi.org/10.1007/s00024-011-0301-7.

Candela, T., Renard, F., Bouchon, M., Brouste, A., Marsan, D., Schmittbuhl, J., and Voisin, C. (2009). Characterization of fault roughness at various scales: Implications of three-dimensional high resolution topography measurements. *Pure Appl Geophys*, 166(10-11):1817–1851. https://doi.org/10.1007/s00024-009-0521-2.

Corradetti, A., McCaffrey, K., Paola, N. D., and Tavani, S. (2017). Evaluating roughness scaling properties of natural active fault surfaces by means of multi-view photogrammetry. *Tectonophysics*, 717:599–606. https://doi.org/10.1016/j.tecto.2017.08.023.

Den Outer, A., Kaashoek, J., and Hack, H. (1995). Difficulties with using continuous fractal theory for discontinuity surfaces. *Int J Rock Mech Min*, 32(1):3–9. https://doi.org/10.1016/0148-9062(94)00025-x.

Ficker, T. and Martišek, D. (2016). Alternative method for assessing the roughness coefficients of rock joints. *J Comput Civil Eng*, 30(4):04015059. https://doi.org/10.1061/(asce)cp.1943-5487.0000540.

Frigo, M. and Johnson, S. (2005). The design and implementation of FFTW3. *Proceedings of the IEEE*, 93(2):216–231. https://doi.org/10.1109/jproc.2004.840301.

Grasselli, G. (2001). *Shear Strength of Rock Joints based on quantified Surface Description*. PhD thesis, Ecole polytechnique federale de Lausanne.

Gravanis, E. and Pantelidis, L. (2019). Determining of the joint roughness coefficient (JRC) of rock discontinuities based on the theory of random fields. *Geosciences*, 9(7):295. https://doi.org/10.3390/geosciences9070295.

Hastings, H. and Sugihara, G. (1994). *Fractals - A user's guide for the natural sciences*. Oxford Univ Press.

ISO 4287 (1997). Geometrical product specifications (GPS) – surface texture: Profile method – terms, definitions and surface texture parameters. Standard, International Organization for Standardization, Geneva, CH. https://www.iso.org/standard/10132.html.

ISRM (1978). Suggested methods for the quantitative description of discontinuities in rock masses. *Int J Rock Mech Min*, 15(6):319–368. https://doi.org/10.1016/0148-9062(78)91472-9.

Jang, H.-S., Kang, S.-S., and Jang, B.-A. (2014). Determination of joint roughness coefficients using roughness parameters. *Rock Mech Rock Eng*, 47(6):2061–2073. https://doi.org/10.1007/s00603-013-0535-z.

Kulatilake, P., Balasingam, P., Park, J., and Morgan, R. (2006). Natural rock joint roughness quantification through fractal techniques. *Geotechnical and Geological Engineering*, 24(5):1181–1202. https://doi.org/10.1007/s10706-005-1219-6.

Lee, Y.-H., Carr, J., Barr, D., and Haas, C. (1990). The fractal dimension as a measure of the roughness of rock discontinuity profiles. *Int J Rock Mech Min*, 27(6):453–464. https://doi.org/10.1016/0148-9062(90)90998-h.

Li, Y. and Huang, R. (2015). Relationship between joint roughness coefficient and fractal dimension of rock fracture surfaces. *Int J Rock Mech Min*, 75:15–22. https://doi.org/10.1016/j.ijrmms.2015.01.007.

Li, Y., Xu, Q., and Aydin, A. (2017). Uncertainties in estimating the roughness coefficient of rock fracture surfaces. *B Eng Geol Environ*, 76(3):1153–1165. https://doi.org/10.1007/s10064-016-0994-z.

Li, Y. and Zhang, Y. (2015). Quantitative estimation of joint roughness coefficient using statistical parameters. *Int J Rock Mech Min*, 77:27–35. https://doi.org/10.1016/j.ijrmms.2015.03.016.

Maerz, N., Franklin, J., and Bennett, C. (1990). Joint roughness measurement using shadow profilometry. *Int J Rock Mech Min*, 27(5):329–343. https://doi.org/10.1016/0148-9062(90)92708-m.

Magsipoc, E., Zhao, Q., and Grasselli, G. (2020). 2d and 3d roughness characterization. *Rock Mech Rock Eng*, 53(3):1495–1519. https://doi.org/10.1007/s00603-019-01977-4.

Malinverno, A. (1990). A simple method to estimate the fractal dimension of a self-affine series. *Geophys Res Lett*, 17(11):1953–1956. https://doi.org/10.1029/gl017i011p01953.

Mandelbrot, B. B. (1985). Self-affine fractals and fractal dimension. *Phys Scripta*, 32(4):257–260. https://doi.org/10.1088/0031-8949/32/4/001.

Marsch, K. (2020). Rock surface roughness determination: Matlab scripts of evaluation algorithms and original scanned surfaces. https://doi.org/10.14279/depositonce-9592.3.

Marsch, K., Wujanz, D., and Fernandez-Steeger, T. M. (2020). On the usability of different optical measuring techniques for joint roughness evaluation. *B Eng Geol Environ*, 79(2):811–830. https://doi.org/10.1007/s10064-019-01606-y.

Myers, N. (1962). Characterization of surface roughness. *Wear*, 5(3):182–189. https://doi.org/10.1016/0043-1648(62)90002-9.

Odling, N. (1994). Natural fracture profiles, fractal dimension and joint roughness coefficients. *Rock Mech Rock Eng*, 27(3):135–153. https://doi.org/10.1007/bf01020307.

Pickering, C. and Aydin, A. (2016). Modeling roughness of rock discontinuity surfaces: A signal analysis approach. *Rock Mech Rock Eng*, 49(7):2959–2965. https://doi.org/10.1007/s00603-015-0870-3.

Renard, F., Voisin, C., Marsan, D., and Schmittbuhl, J. (2006). High resolution 3d laser scanner measurements of a strike-slip fault quantify its morphological anisotropy at all scales. *Geophys Res Lett*, 33(4). https://doi.org/10.1029/2005gl025038.

Schmittbuhl, J., Vilotte, J.-P., and Roux, S. (1995). Reliability of self-affine measurements. *Phys Rev E*, 51(1):131–147. https://doi.org/10.1103/physreve.51.131.

Stigsson, M. and Mas Ivars, D. (2019). A novel conceptual approach to objectively determine JRC using fractal dimension and asperity distribution of mapped fracture traces. *Rock Mech Rock Eng*, 52(4):1041–1054. https://doi.org/10.1007/s00603-018-1651-6.

Tatone, B. S. (2009). Quantitative characterization of natural rock discontinuity roughness in-situ and in the laboratory. Master's thesis, University of Toronto.

Tatone, B. S. and Grasselli, G. (2010). A new 2d discontinuity roughness parameter and its correlation with JRC. *Int J Rock Mech Min*, 47(8):1391–1400. https://doi.org/10.1016/j.ijrmms.2010.06.006.

Tse, R. and Cruden, D. (1979). Estimating joint roughness coefficients. *Int J Rock Mech Min*, 16(5):303–307. https://doi.org/10.1016/0148-9062(79)90241-9.

Turk, N., Greig, M., Dearman, W., and Amin, F. (1987). Characterization of rock joint surfaces by fractal dimension. *Proceedings 28th Symp. Rock Mechanics, June 29 - July 1, 1987, Tucson, AZ*.

Wang, C., Wang, L., and Karakus, M. (2019). A new spectral analysis method for determining the joint roughness coefficient of rock joints. *Int J Rock Mech Min*, 113:72–82. https://doi.org/10.1016/j.ijrmms.2018.11.009.

Wang, L., Wang, C., Khoshnevisan, S., Ge, Y., and Sun, Z. (2017). Determination of two-dimensional joint roughness coefficient using support vector regression and factor analysis. *Eng Geol*, 231:238–251. https://doi.org/10.1016/j.enggeo.2017.09.010.

Yang, Z. Y., Lo, S. C., and Di, C. C. (2001). Reassessing the joint roughness coefficient (JRC) estimation using z 2. *Rock Mech Rock Eng*, 34(3):243–251. https://doi.org/10.1007/s006030170012.

Yong, R., Ye, J., Liang, Q.-F., Huang, M., and Du, S.-G. (2018). Estimation of the joint roughness coefficient (JRC) of rock joints by vector similarity measures. *B Eng Geol Environ*, 77(2):735–749. https://doi.org/10.1007/s10064-016-0947-6.

Yu, X. and Vayssade, B. (1991). Joint profiles and their roughness parameters. *Int J Rock Mech Min*, 28(4):333–336. https://doi.org/10.1016/0148-9062(91)90598-g.

Zhang, G., Karakus, M., Tang, H., Ge, Y., and Zhang, L. (2014). A new method estimating the 2d joint roughness coefficient for discontinuity surfaces in rock masses. *Int J Rock Mech Min*, 72:191–198. https://doi.org/10.1016/j.ijrmms.2014.09.009.

Chapter 4

Incoherency of replica-based shear strength criteria regarding tensile fractures with high wall strength

This chapter is a preprint version of the following submitted article:

Marsch, K., and Fernandez-Steeger, T. M. (unpublished). Incoherency of replica-based shear strength criteria regarding tensile fractures with high wall strength.

Abstract

For the estimation of the shear strength of rock discontinuities many empirical criteria exist. They aim at avoiding direct shear testing by using rather simple mechanical and geometrical index values. However, many of the criteria have been established based on direct shear tests of rock replicas. These materials show low strength compared to rock and consequently the influence of the wall strength versus the influence of the roughness may have been captured insufficiently. Accordingly, this study is to verify whether some existing shear strength criteria are applicable to high strength rocks. To answer that question direct shear tests on artificial tensile fractures exhibiting uniaxial compressive strengths of averaged 230 MPa were performed. The results are compared to data of prior studies and the predictions from four different empirical strength criteria. For the sake of comparability only criteria incorporating the well-established two-dimensional JRC and Grasselli's 3D roughness parameterisation are applied. A major finding from this study is that with the 3D roughness measure in 35% of the cases the shear strength is overestimated. Instead, with the classical JRC approach the predicted shear strength mostly do not exceed the actual shear strength. Both approaches lead to significant differences concerning the predictions and test results of high strength rocks under low normal stress, yet seemingly, the JRC approach is on the safe side. Additionally, for high strength rock not only extensive roughness but pronounced singular asperities seem to have a larger relevance. However, further tests are required to gain a more nuanced picture which could result in a greater, rock type related portfolio of constitutive equations.

4.1 Introduction

The deformational behaviour of rock masses is predominantly determined by the strength of the discontinuities within. For many rock engineering works, it is therefore important at least to estimate the shear resistance of the discontinuities in a reasonable magnitude. Due to the numerical dominance of joints (being discontinuities without visible displacement) in most rock masses, it has been common practice to use the words "joint" and "discontinuity" synonymously (c.f. Hencher and Richards, 2015). This is followed here too.

To enable the estimation of the shear strength of rock joints without conducting sophisticated direct shear tests many empirical criteria incorporating rather simple index values have been put forward. Singh and Basu (2018) give a recent overview of prior studies. In general, the criteria consider the basic friction angle (ϕ_b), the strength of the joint walls (either uniaxial compressive or tensile strength, σ_C and σ_T respectively) and the surface roughness (parametrised in varying forms). Concerning the roughness description, first, the Joint Roughness Coefficient (JRC) introduced by Barton (Barton, 1973; Barton and Choubey, 1977) is the most accepted index considering the analysis of 2D profiles – also, the ISRM (1978b) refers to the JRC for roughness characterisation. Second, Grasselli's set of indices (Grasselli et al., 2002; Tatone and Grasselli, 2009) dominates the parameterisation of rock joint roughness in 3D.

Conducting direct shear tests with natural rock discontinuities is elaborate and most of the time cumbersome. Especially under high normal stress, the surfaces are eligible for testing only once since asperities are sheared off and consequently upon subsequent tests solely the residual strength is determinable. As a way out of this dilemma many researchers used mortar or cement replicas of rock joints to establish reproducible test conditions. For example, Liu et al. (2018) argued replica material being admissible for testing due to similar σ_C to σ_T ratios compared to that of rock. However, replica materials exhibit very low compressive strength compared to many rocks. For example, Kulatilake et al. (1995) reported values for σ_C as low as 4 MPa and 11 MPa respectively. Lee et al. (2014) gave values in the range of 54 to 84 MPa and Ban et al. (2020) used material with a uniaxial compressive strength of 29 MPa. In addition, in studies on real rock samples rather low strength materials were used. For example, Barton and Choubey (1977) used seven different rocks with a mean σ_C of 92 MPa whereas Grasselli and Egger (2003) used six rock types with a mean σ_C of 108 MPa.

It must be realised that the strength of the joint walls greatly influences shear test results since the impact of the roughness on the overall shear strength is controlled by the ratio of the strength of the material to the applied normal stress. When the ratio is large, dilation takes place resulting in an increase of shear resistance. On the opposite, when the ratio is small the asperities are sheared off and the roughness share in the overall shear resistance decreases. These two cases represent idealised extreme situations that may never occur in that straight form. Instead, other situations such as interlocking at singular asperities are not considered in terms of stress. Nevertheless, it can be argued that the criteria account for the stress ratio since all incorporate a term for strength. However, as the formulations are essentially outcomes of fitting results of direct shear tests, the influence of the joint wall strength versus the influence of the roughness may be imbalanced.

Consequently, in this study high strength rocks (with a mean $\sigma_C > 230$ MPa) are used as sample material in direct shear tests. The primary objective of this research is to verify whether some existing shear strength criteria established based on low to

Table 4.1: Description and origin of the rock specimens used in this study

Sample	Approximate Origin	Roughness category according to ISRM (1978b)
Basalt (B)	Kerala, India	I—rough stepped
Granite (G)	Lausitz, Germany	II—smooth stepped
Limestone (K)	Altmühltal, Germany	IV—rough undulating
Slate (SF)	Campo-Valongo, Portugal	V—smooth undulating
Sandstone (SI)	Agra, India	VII—rough planar
Sandstone (SS)	Rakovice, Poland	IV—rough undulating

medium strength rock or rock like material could be extrapolated to high strength (real) rock surfaces. Since for most rock engineering projects above ground the magnitude of the normal stress on the discontinuities is small, in this research, a value of 0.2 MPa is applied.

4.2 Materials and Methods

4.2.1 Rock material and sample preparation

For the objective of this study the sample materials have to meet a second condition besides exhibiting comparably high σ_C values: the set of test surfaces should cover a broad range of roughness categories, following the definitions of the ISRM (1978b), as the results shall be broadly applicable. Consequently, all three main rock groups are considered since different composition and texture (because of varying formation regimes) would result in contrasting roughness upon fracturing. This need of varying degrees of roughness for the specimens is conveniently met by using man-made samples.

To produce the samples, a random selection of quarry stones was brought together meeting the conditions mentioned before. Then, the rock blocks were manually fractured along pre-produced saw cut notches using hammer and chisel. Thereby, clean tensional cuts formed where the upper and lower parts feature a high degree of accordance. Additionally, within fresh samples possible effects due to weathering concerning the strength of the subsequent discontinuity walls are kept to a minimum. Moreover, using fabricated rock blocks allows controlling the size of the produced samples and ensures full use of the working capacity of the shear test apparatus. In general, according to Vogler et al. (2017) the roughness of artificial tensile fractures spans the whole domain of natural tensile fractures. It is therefore admissible to use them as proxy surfaces.

For this study, samples were produced from basalt, granite, limestone, slate and two different sandstones. In Table 4.1 the origins and resulting roughness categories are listed. Note that the roughness categories were assigned by a group of five engineering geologists as a first estimate and are therefore rather subjective. For an independent categorisation, all geometry models of the surfaces are available digitally in the repository to this study Marsch (2021). For an impression, close-up views of some surfaces are given in Figure 4.1.

As a basic mechanical characterisation of the rocks used, σ_C, σ_T and ϕ_b were determined as they are usual inputs for most empirical shear strength criteria (c.f. Li et al., 2020). The compression and tension tests were carried out according to the ISRM (1978a, 1979). A total of 40 tests was performed. The basic friction angles were determined also

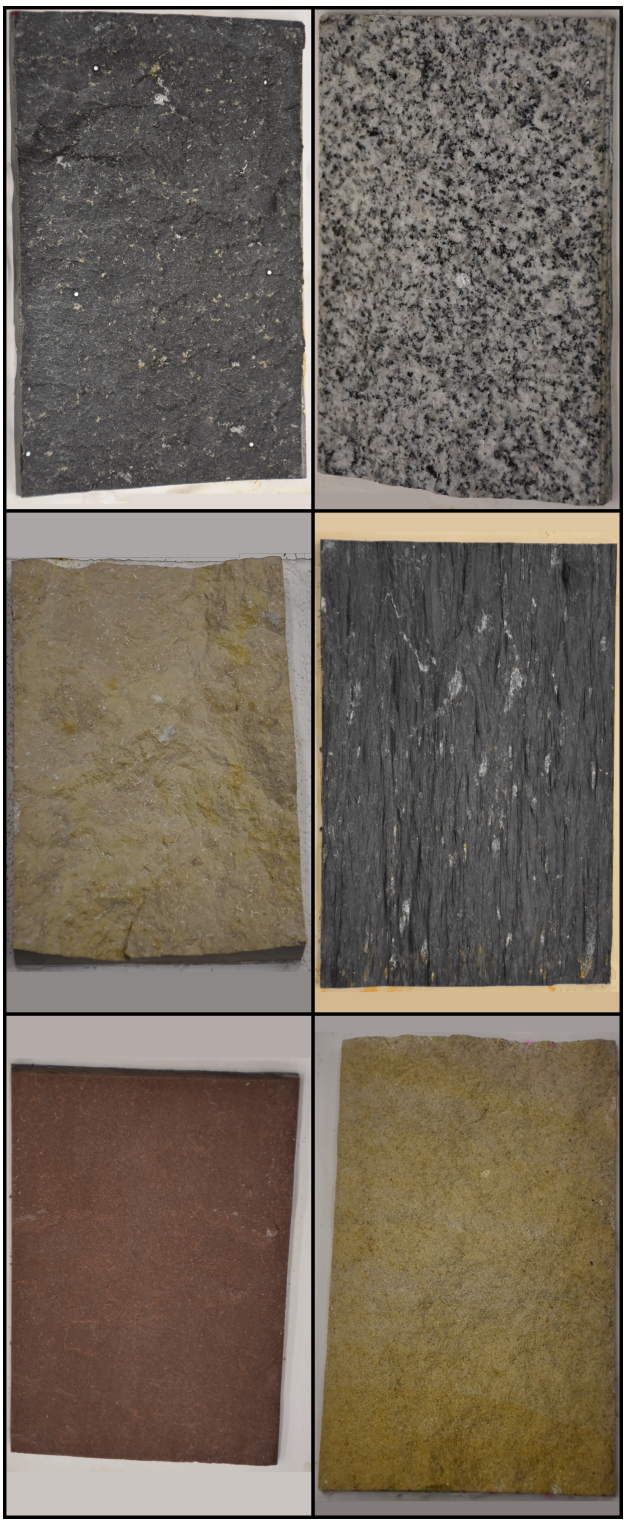

Figure 4.1: Exemplary images of on average 174 mm long samples of the 6 rock types used in this study. From upper left to lower right: Basalt (B), Granite (G), Limestone (K), Slate (SF), Sandstone (SI) and Sandstone (SS)

Table 4.2: Strength parameters from laboratory testing on cores; σ_C stands for uniaxial compressive strength, σ_T for tensile strength and ϕ_b for basic friction angle

Sample	σ_C [MPa]		σ_T [MPa]		ϕ_b [°]	
	mean	std	mean	std	median	std
Basalt (B)	328.0	1.7	22.3	0.7	30.9	1.0
Granite (G)	204.9	17.5	14.6	2.2	29.4	1.5
Limestone (K)	216.5	20.3	14.3	2.4	32.1	5.0
Slate (SF)	138.8	5.4	16.1	2.7	33.5	1.1
Sandstone (SI)	269.7	1.0	22.5	3.4	29.1	1.9
Sandstone (SS)	34.6	6.7	3.8	0.7	34.9	1.4

according to the ISRM as described in Alejano et al. (2018). For the tilt tests planar rectangular specimens as well as rock cores were used. However, the planar specimens yielded larger variation than the cores in linear contact. Therefore, it is reasonable to use the core test set-up only. After five tests on the same contact lines the cores were rotated 120° so that 15 tilt angles were measured for each rock material. A total of 90 values for ϕ_b was gathered. In Table 4.2 the mean values and the standard deviations for σ_C and σ_T are listed whereas for ϕ_b the median values (as recommended) and the standard deviations are given. Regarding the limestone, comparably large standard deviations reflect the also visible heterogeneity of the material. Concerning the slate, the compressive and tensional tests were carried out perpendicular to the dominant cleavage conforming to the later normal loading direction during shear testing. The low strength sandstone sample SS serves as a reference specimen for the other materials.

A key issue in direct shear testing is a correct placement of the samples in the testing machine. To avoid additional moment forces within the shearing process, great care must be taken concerning the alignment of the surfaces especially with the shear load direction. Consequently, the visual best-fit plane of the irregular sample surfaces must coincide with the actual shear plane of the apparatus as good as possible. Placement becomes increasingly important with large-scale samples as already small tilt angles produce comparably great height differences at the opposite ends of the sample. This must be avoided since artificial slopes due to erroneous installation, if not accounted for in the assessment of the tests, would add to the overall shear strength. The standard procedure towards reducing these effects involves encapsulating the specimens in cement or plaster (see Muralha et al., 2014). For this study a fast curing dental plaster was used as casting material that yields uniaxial compressive strength of approximately 60 MPa when fully hardened. Additionally, having fixated the samples in such way ensures flat and orthogonal shaped perimeters, establishing a force-locked connection with the testing apparatus.

4.2.2 Direct shear testing

In this study, a direct shear testing apparatus developed in-house from the Ruhr University at Bochum/Germany was used as described in Gehle and Kutter (2003). It consists of a high stiffness frame that accommodates the servo-controlled shear and normal load actuators. A special feature of the machine is its immobile normal load actuator sitting in a vertical linear guide bearing that does not allow rolling or pitching of the upper sample half. By that, the testing set-up is very much constrained and controllable.

First, a normal stress of 0.2 MPa was applied. Thereafter the specimens were sheared at a constant normal load with a displacement rate of 0.003 mm/sec, which is in accordance with the ISRM suggested method (Muralha et al., 2014). Since this study focuses on the peak strength, the tests were stopped approximately 1 mm after the maximum shear resistance was reached. However, the overall shear displacement was always at least 2 mm. The shear and normal loads as well as the horizontal and vertical displacements were recorded.

4.2.3 Surface capturing and roughness evaluation

The devices used for capturing of the surfaces and the resulting quality of the models have large effects on the derived roughness indices (c.f. Marsch et al., 2020). To acquire credible representations of the tensile fractures in this study a GOM ATOS structured light scanner, being a special photogrammetric device, was used. It offers a spatial accuracy for the final surface models as good as 40 μm. The average resolution in the evaluation plane considering all samples scanned approximates to 50 points per mm^2. Most importantly, the acquired surface meshes were only cleansed of obvious artefacts-—no data was interpolated as the resolution of the measurement outcomes was already high. Due to the controlled production of the samples, resulting in assumed equal upper and lower sample halves, only the lower parts were scanned. All models are also given in the repository to this study (see Marsch, 2021). As mentioned in the introduction, the Joint Roughness Coefficient and Grasselli's roughness measure are most widely used for roughness parameterisation in 2D and 3D, respectively (c.f. Singh and Basu, 2018). Therefore, in this study these two approaches are applied.

The standard procedure for the determination of the JRC involves comparative use of the nomographic chart developed by Barton and Choubey (1977). For a more objective estimation different statistical and fractal measures were calculated for the standard profiles in the past. Magsipoc et al. (2020) give an overview of the techniques whereas Li and Zhang (2015) and Li and Huang (2015) list correlations of the specific measures with JRC. However, Marsch and Fernandez-Steeger (2021) showed that fractal calculation schemes do not improve the determination of JRC and that the simple statistical parameter Z_2 by Myers (1962) suffices for rock roughness characterisation from profiles. Consequently, the correlation of JRC with Z_2 from Tatone and Grasselli (2010) in the following form was used (being valid only for sampling intervals of 1 mm):

$$\mathrm{JRC}_{Z_2} = 55.03 \cdot (Z_2)^{0.74} - 6.1 \tag{4.1}$$

For the determination of JRC two paths of data gathering were followed: (1) measuring profiles with a tactile profile gauge and (2) extracting profiles from the 3D representations of the surfaces. Concerning the profile gauge, profiles were measured parallel to the shear direction with a spacing of 10 mm between each profile and a sampling interval along the profiles of 1 mm. To minimise digitalisation errors, the traces were processed using the algorithm from Alameda-Hernández et al. (2014). Gathering profile-based information on roughness with a tactile profilometer is the method used in the underlying work by Barton and Choubey (1977). It still is a straightforward and intuitive approach which is used often in field and laboratory practice. Depending on the dimensions of the direct shear samples between 18 and 24 lines were traced, resulting in a total of 422 measurements (see Marsch (2021) for data).

Regarding the extraction of profiles from the 3D models, first, traces covering the full length of the samples along the shear direction were acquired with a parallel spacing of

1 mm. They were then linearly interpolated at 0.1 mm intervals according to the average raster resolution of the surfaces of 0.14 mm. Establishing a constant sampling interval is a basic prerequisite for usage of correlations. Second, by means of a sliding window, segments of 100 mm length were extracted every millimetre along the traces of the first processing step. Subsequently, the resulting profiles were individually detrended and sampled at 1 mm steps to obtain JRC via Equation 4.1. This routine was established since Barton and Choubey's (1977) standard profiles feature a length of 100 mm.

The three-dimensional characterisation of joint roughness according to Grasselli et al. (2002) consists of three numbers. At first, all areas of a surface (A_{θ^*}) which face the shear direction, and which fall below a pre-set threshold dip angle (θ^*) are identified successively. Then, a power function with the exponent C is fitted to this cumulative area distribution as follows:

$$A_{\theta^*} = A_0 \left(\frac{\theta^*_{max} - \theta^*}{\theta^*_{max}} \right)^C \tag{4.2}$$

Here, A_0 denotes the y-axis intercept and θ^*_{max} is the maximum dip angle. Following Tatone and Grasselli (2009) the three numbers condense to a roughness index, named Grasselli-Parameter GP in this study:

$$GP = 2A_0 \, \frac{\theta^*_{max}}{C+1} \tag{4.3}$$

However, there exists a problem with the maximum dip angle θ^*_{max}: it varies significantly depending on the measurement resolution (Magsipoc et al., 2020). Hence, a standard resolution should be defined in the future to establish comparability. In this context, Tatone and Grasselli (2009) recommend a nominal point spacing smaller than 0.5 mm. Instead, Tian et al. (2018) used models with a point spacing of 0.25 mm, however not finding contradictions with Grasselli's original roughness definition. Consequently, higher resolutions are not needed especially since the original definition is most likely based on lower resolution measurements. In any case, the resolution used in this study (0.14 mm on average) is sufficient.

4.3 Selective review of shear strength studies and criteria

Without doubt, Patton (1966) pioneered the works on shear resistance of rock discontinuities with the development of his bi-linear criterion. Another important research is that by Ladanyi and Archambault (1970) who advanced Patton's findings and introduced a more realistic continuously curved failure envelope. After that many others joined in the process of investigating shear strength. A wide but non-comprehensive overview of available studies introducing shear strength criteria can be found in Singh and Basu (2018).

Since comprehensibility is an important criterion and a prerequisite for a thorough interpretation, for this research only studies entered the shortlist in Table 4.D for which at least direct shear test results, information on the materials, and numbers of tests are accessible. At best, also morphological measurements are available, but this is unfortunately not always the case. Figure 4.2 visualises the results of these selected prior studies which were re-digitised from the online versions of the publications. Looking at the full normal stress range in part a), it becomes obvious that most research focused on normal stresses up to roughly 2.5 MPa which are therefore depicted more closely in b). The attention of prior studies on that stress range is most probably due to the shearing-off

of asperities with increasing normal stress. Consequently, the resistance stemming from the surface morphology loses significance in the overall strength. Note that in both parts of Figure 4.2 Mohr-Coulomb lines (no cohesion) with overall friction angles of 32° and 70° are drawn. The 70°-line was suggested by Barton and Choubey (1977) as a maximum allowable shear strength envelope for design purposes. Instead, the 32°-line found here establishes a reasonable lower bound considering all data points in the figure. This general value is quite interesting because obviously every study used its own set of samples with different strengths and additionally with various roughness degrees. Nonetheless, 32° and 70° are good minimum and maximum estimates for the overall friction angle of rock or rock-like materials used so far irrespective of the wall strength and surface roughness, at least in cases of the normal stress being smaller than approximately 2.5 MPa.

For the establishment of shear strength criteria however, the wall strength of the samples and their roughness should not be left out of consideration. Therefore, in Figure 4.3, in case this information was accessible, the uniaxial compressive strength σ_C is plotted versus roughness parameterised in the forms of JRC and GP, respectively. Here, the JRC values are those given by the authors and determined solely on a geometrical basis either by visual comparison of profiles to the standard-chart or by calculation using different correlation functions. Consequently, the values are difficult to compare. Also note that Fardin (2008) determined his high values of σ_C using cubic specimens (which is fundamentally different to the other studies where cores from replica materials were used) and that the numbers from Barton and Choubey (1977) represent the lower bound, the mean, and the upper bound of their whole data set (as no values for each rock material was provided). Concerning the uniaxial compressive strength, in general, from Figure 4.3 it becomes obvious that the replica materials of the considered studies exhibit low values compared to the real rocks used. This is of paramount importance since the effects of roughness on the shear strength may not have been reproduced with these replica materials fully, as the samples might have failed too early due to stress concentration at prominent asperities. Consequently, the shear-off component in the overall shear strength could be overrepresented and the roughness component underrepresented in the test results. Furthermore, the narrowness regarding the (geometrical) roughness of the underlying data is another limiting factor for the applicability of the considered empirical shear strength criteria. For example, Ban et al. (2020) used five different morphologies ranging from 6.3 to 10.1 on the JRC scale whereas Xia et al. (2014) built their equation even only on three surfaces featuring 5.12, 7.75 and 11.14 on the GP scale. Anyhow, to enhance reliability and improve significance of the work at hand, all data from studies fulfilling the requirements mentioned above have been considered and plotted.

It must be emphasised that the roughness values depicted in Figure 4.3 were derived from the surface topographies only. However, there exists no direct correlation which allows to convert GP, being a purely geometrical parameter, into JRC, without considering mechanical input parameters such as the applied normal stress and the material strength (c.f. Grasselli and Egger, 2003). Consequently, a comprehensible, solely geometrical comparison of the two roughness definitions is impossible. Therefore, to obtain a general sense of the ranges of roughness tested in prior studies, the mechanical JRC were back-calculated for the data sets of Figure 4.3 where possible. The outcomes are depicted in Figure 4.4 (note the different abscissa). There, also the results of this study are plotted for comparison (addressed more detailed below). It can be seen for example that a few tests from Dong et al. (2017) led to values of JRC_{MECH} below zero, yet their geometrically determined JRC were well above 5. Instead, some tests from Tang and Wong (2016) or Grasselli and Egger (2003) yielded JRC_{MECH} well beyond 20.

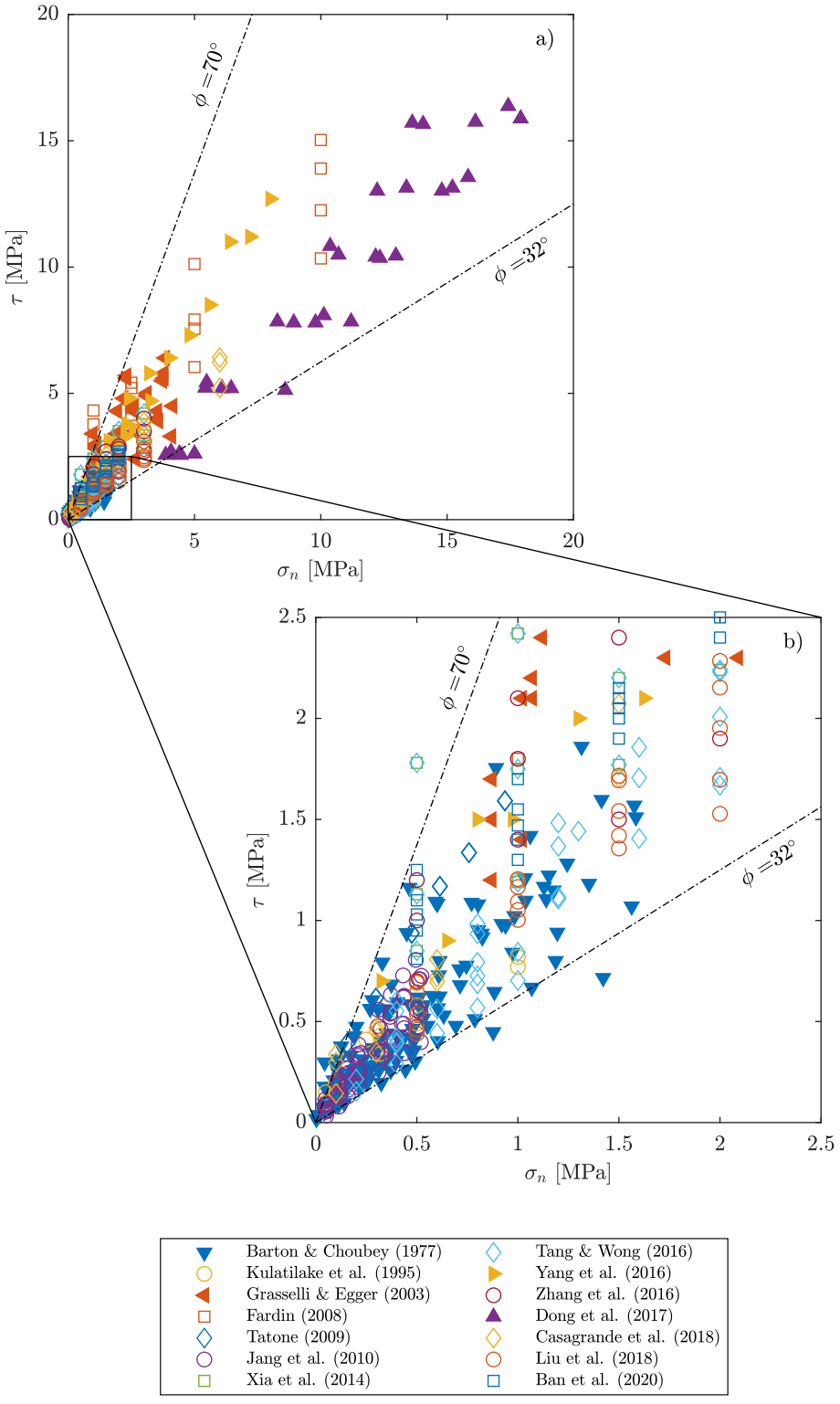

Figure 4.2: τ/σ diagram plotting direct shear test results from the studies indicated in the symbol list - unfilled symbols denote replicas made of non-rock materials like concrete, mortar, or artificial stone, while filled symbol show data from rock specimen

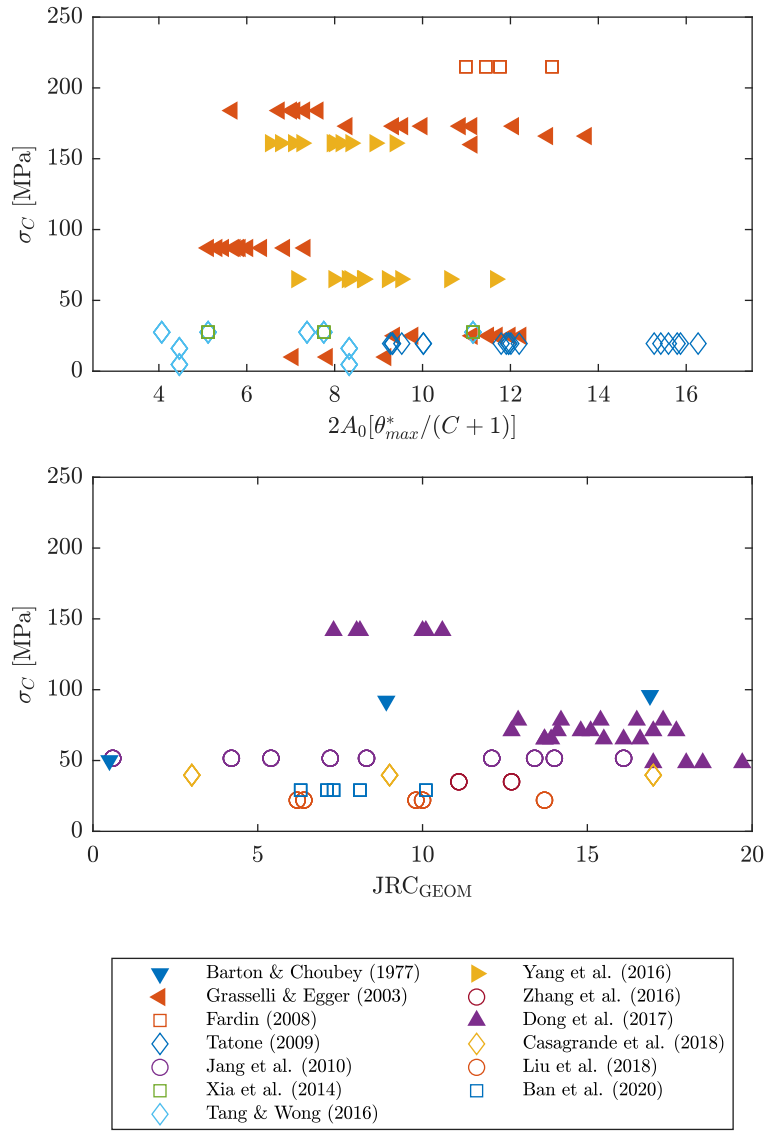

Figure 4.3: Uniaxial compressive strength σ_C and geometrical roughness in terms of the Grasselli-Parameter GP and the geometric Joint Roughness Coefficent $\mathrm{JRC_{GEOM}}$ from the studies indicated in the symbol list - unfilled symbols denote replicas made of non-rock materials like concrete, mortar, or artificial stone, while filled symbol show data from rock specimen

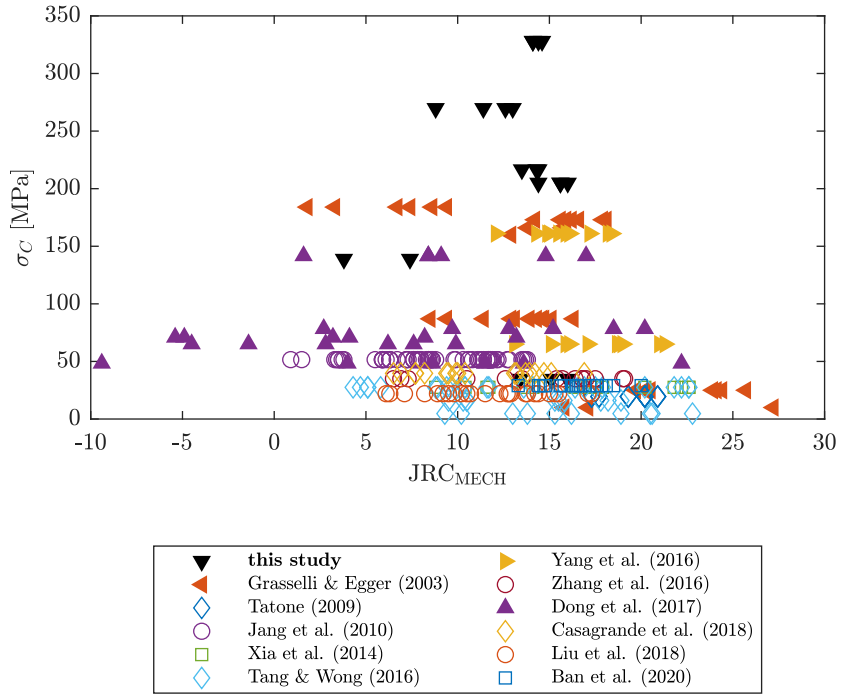

Figure 4.4: Rearranged compilation of the test results from the studies indicated in the symbol list in terms of the back-calculated mechanical roughness JRC$_{\mathrm{MECH}}$ - unfilled symbols denote replicas made of non-rock materials like concrete, mortar, or artificial stone, while filled symbol show data from rock specimen

All these cases are outside of the range of definition of JRC defined by Barton (1973), which is 0 to 20. However, most importantly, Figure 4.4 shows that also for studies which initially used the GP roughness approach the back-calculated (mechanical) JRC lie predominantly between 5 and 20, and that there is a general lack of data for samples having JRC$_{\mathrm{MECH}}$ smaller 5.

To identify clusters of roughness and uniaxial compressive strength in the available data, Figure 4.4 was advanced to Figure 4.5. For that, a classification in groups comprising one unit on the JRC scale and ten units of σ_C was performed. Firstly, materials with uniaxial compressive strengths of 50 $\pm$5 MPa, and 25 $\pm$10 MPa were tested most often in prior works. Secondly, surfaces exhibiting JRC-roughness of 8 $\pm$0.5 and 12 $\pm$0.5 are significantly overrepresented. Another less pronounced and broader cluster is seen at JRC ranging from 15.5 to 18.5. This overrepresentation of some roughness and strength combinations has a large effect on the applicability of the deduced shear strength criteria: although validity being promised for many types of rock and roughness classes, all shear strength criteria rely on their respective, very specific sets of samples. Consequently, strength parameters and morphological characteristics are incorporated implicitly in the final formulations which result from fitting more or less physically meaningful functions to direct shear test data.

In many cases the results from the underlying shear tests are only given in terms of peak values. However, to evaluate the applicability of a criterion to other cases the deformational behaviour of the initial samples provides further important information. Concerning the studies from Table 4.D, in case information was accessible, in Figure 4.6 the ratios of shear to normal stress are plotted versus shear displacements. Even though to different degrees, essentially the same behaviour is seen for all six studies: no signif-

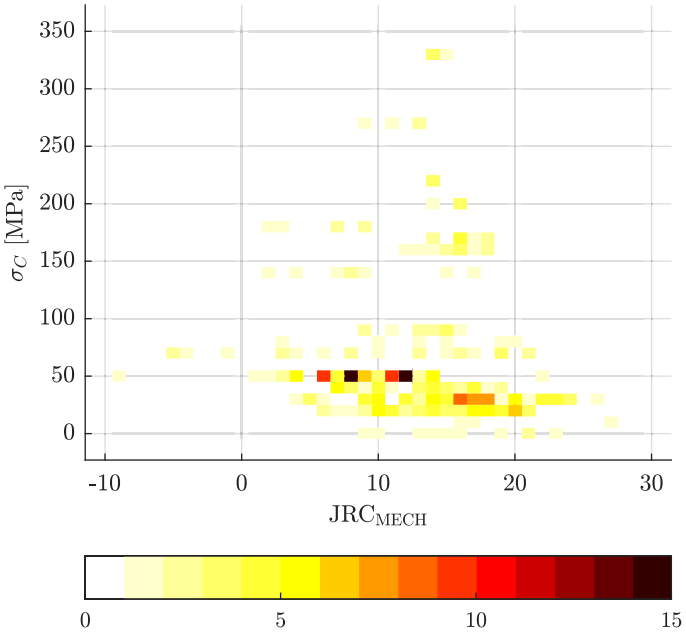

Figure 4.5: Frequency of occurrence of back-calculated (mechanical) JRC in the prior studies as of Figure 4.4 - the colouring corresponds to the number of data points in the specific class of roughness and σ_C

icant drops of the stress ratio occurs after the initial slope is overcome. This gives the impression that all the various replica materials deform in ductile mode. This is important as it could indicate that their strengths may be too low (irrespective of being determined under uniaxial or tensile conditions) and that their mechanical behaviour may be too different to justify a simple extrapolation of the results to real rock material.

Under consideration of the issues mentioned afore, especially before the background of large variation of the shear resistance in the low normal stress range (Figure 4.2), the choice to make between the many empirical shear strength criteria is not trivial—-and, there exist at least 25 of them (c.f. Singh and Basu, 2018; Li et al., 2020). Also, traceability and comparability concerning the roughness parameterisation play important roles. Hence, for this study, solely criteria incorporating the well-established roughness metrics JRC or GP are considered. As it is the primary objective of this research to verify the application of replica-based shear strength criteria for real (high strength) rock surfaces, besides the original (rock based) criteria from Barton (1973) and Grasselli and Egger (2003), in each case one alternative equation is employed. The selected criteria are given in Table 4.3. Tang et al.'s (2014) equation was chosen because it uses Grasselli's roughness definition in a new arrangement rather than adjusting coefficients as done by Xia et al. (2014) for example. Furthermore, the morphology component is integrated in a physically reasonable way in form of an addition to the basic friction angle ϕ_b. On the side of an alternative JRC-related criterion, Jang et al.'s (2010) equation was selected because it is based on samples covering a relatively broad range of JRC roughness classes (c.f. Figure 4.3).

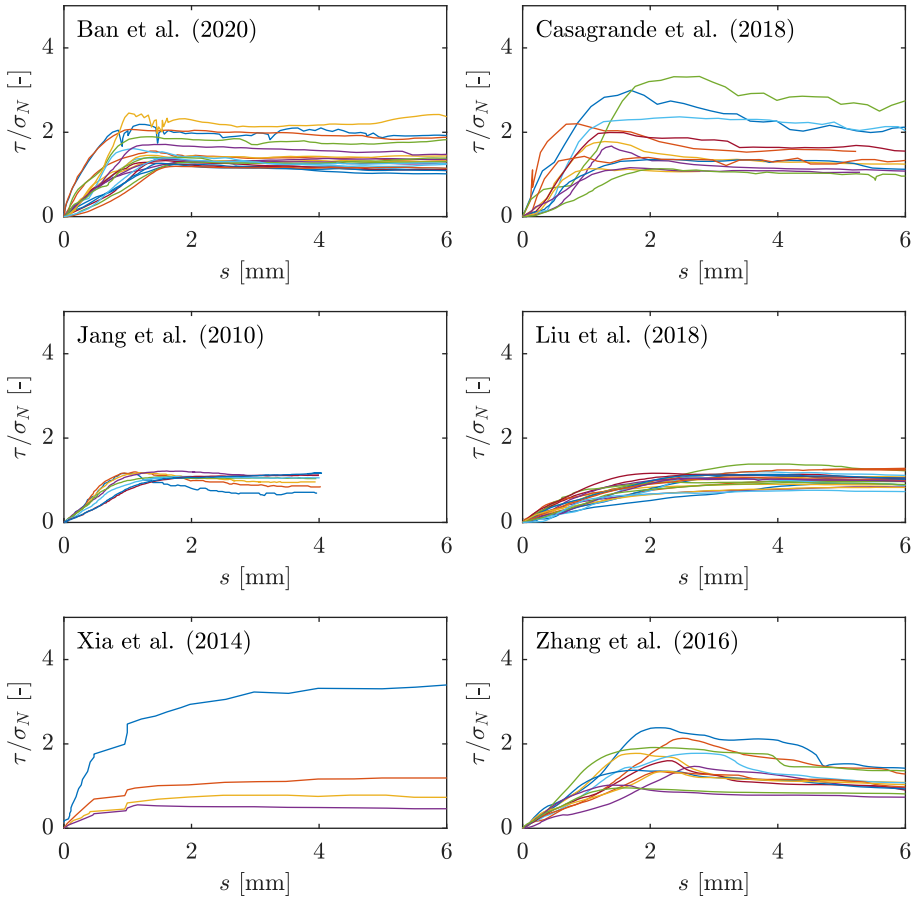

Figure 4.6: Ratio of shear to normal stress plotted versus shear displacement from six different studies which used replicas from rock surfaces made of non-rock materials like concrete, mortar, or artificial stone (digitised from the original publications)

Table 4.3: Selected empirical shear strength criteria

Reference	**Shear strength criterion**
Barton (1973)	$\tau = \sigma_n \cdot \tan\left[\phi_b + \text{JRC} \cdot \log\left(\frac{\text{JCS}}{\sigma_n}\right)\right]$
Grasselli and Egger (2003)	$\tau = \sigma_n \cdot \tan\left[\phi_b + \left(\frac{\theta^*_{max}}{C}\right)^{1.18\cos\alpha}\right] \cdot \left[1 + e^{-(\theta^*_{max}/9A_0C)(\sigma_n/\sigma_T)}\right]$
Jang et al. (2010)	$\tau = \sigma_n \cdot \tan\left[\phi_b + 3.15 \cdot \text{JRC}^{0.5} \cdot \log\left(\frac{\text{JCS}}{\sigma_n}\right)\right]$
Tang et al. (2014)	$\tau = \sigma_n \cdot \tan\left[\phi_b + 10 \cdot \frac{A_0\theta^*_{max}}{1+C} \cdot \frac{(\sigma_T/\sigma_n)}{1+(\sigma_T/\sigma_n)}\right]$

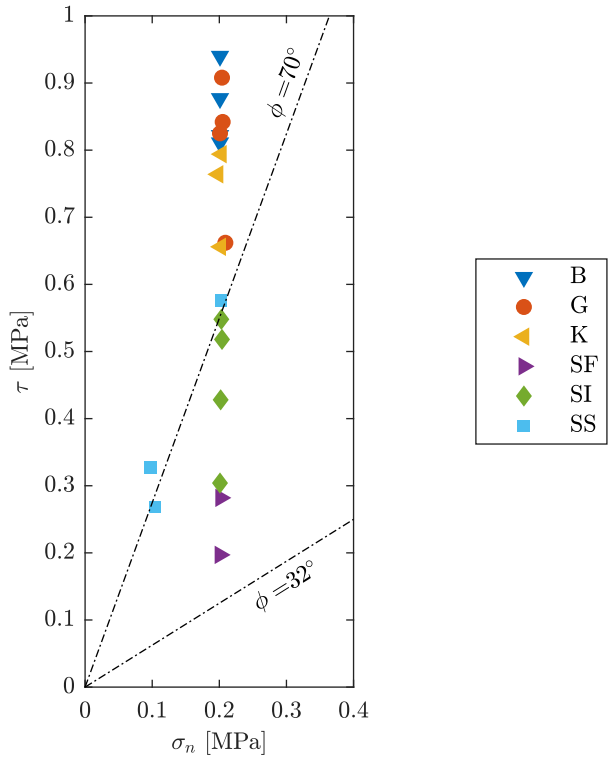

Figure 4.7: Direct shear test results as peak shear stress

4.4 Results

In Figure 4.7 the peak shear stress is plotted versus the applied normal stress in terms of engineering stresses for the original samples of this study. It is common practise to relate the applied loads to the overall, nominal surface (c.f. Muralha et al., 2014; Hencher and Richards, 2015) since the real contact area upon failure is unknown. For the rough, high strength samples B, G and K the obtained peak shear stresses clearly exceed the 70°-line. Compared to prior studies (as depicted in Figure 4.2) so far, no test results of such rock material under this low stress level have been published in the context of establishing empirical shear strength criteria. It can be concluded, for the case of very low normal stress, that tensile fractures in high strength rock appearing rough on the micro-scale exhibit large ratios of peak shear stress to normal stress in excess of 3.5. The samples SF being in a medium range of strength but having a comparably high basic friction angle fall well in-between the 32° and 70°-lines. Most interestingly, the high strength although planar surfaces SI lean towards the upper bound of past studies. Here, step-like plateaus very low in amplitude running transverse to the shearing direction in combination with the high strength of the material result in relatively high shear resistance. The results for the sandstone samples SS which are fairly rough and have strength parameters similar to material of previous studies accord well with the 70°-line.

Additionally, the ratios of shear stress to normal stress are plotted versus the shear displacements in Figure 4.8. The evenly stepped samples B and G exhibit the largest peak ratios from all six rock types tested. Also, the value of the peak shear displacement being roughly 1 mm is rather uniform for all samples, although, each curve refers to a different surface morphology. Apparently, mechanically quite similar surfaces develop in the basalt and granite used here upon the applied method of specimen production in

tensile failure. Regarding the limestone samples (K), one of the three samples exhibits a distinct brittle failure mode with a sharp drop of the stress ratio. That specific sample incorporates a significant upfold rising out of the otherwise undulating surface which could explain the result of this test. Instead, the other two curves from K show a more flat, continuous post-peak progression indicating a ductile behaviour. The results for the two smooth undulating slate samples (SF) are showing, as expected, the lowest shear strength of all samples of this study. Moreover, no pronounced peaks in the curves are visible. Instead, the shearing takes place at a more or less constant level of shear stress (residual strength) after the initial slope is overcome. A very different picture evolves for samples SI compared to the other rocks-—their mode of failure is extremely brittle. Two out of four samples show a kind of stick-slip behaviour with a smaller peak of the stress ratio followed by a larger final peak. These peaks, variable in magnitude for each specimen, are most likely due to the already mentioned step-like plateaus. However, after shearing-off of these steps all four specimens arrive at very similar residual stress ratios. It must be beard in mind that a correct, mating placement of such planar samples showing very low relief is difficult. This is visible in the curve of one sample as initially a shear displacement of more than one millimetre at roughly the residual stress ratio is reached before the interlocking of the sample halves is seen (increase of the ratio to the peak ratio). The results for the other, only comparative sandstone specimens SS, are similar to SI, also exhibiting clear peaks and arriving at the same residual stress ratio, however, without showing preliminary peaks.

Overall, five out of six rock materials tested in this study fail in brittle mode and demonstrate significant shear stiffness. In all tests a distinct stress drop after failure can be observed, except for the slate SF where the drop is not as pronounced. This absolutely differs from cases for which replica materials were used as depicted in Figure 4.6. Only the slate samples SF of this study show similar, most probably ductile ductile deformational behaviour. Consequently, the question arises if, in general, the existing criteria can be used to predict the shear strength of all kinds of rock materials, and especially the ones used in this study.

Before applying empirical shear strength criteria, the roughness parameters must be determined. Naturally, by considering the whole surface in the GP approach, its roughness is characterised by one, unmistakable set of parameters, namely A_0, θ^*_{max} and C as a function of the sample area. Instead, in the JRC concept the selection of a representative profile for the surface is not unambiguously defined: depending on the placement of the profile gauge naturally different JRC result (e.g. Li et al., 2019; Marsch et al., 2020; Babanouri et al., 2020). Moreover, in the laboratory usually profilometer measurements consider all the available area of the samples resulting in profiles shorter or longer than Barton's type-profiles (c.f. Hencher and Richards, 2015; Kim et al., 2015). Clearly, the standard chart is valid only for profiles of 100 mm length and scale effects have been reported to be present (Bandis et al., 1981).

To overcome the scaling problem with JRC determination, as mentioned above, all possible 100 mm profiles were extracted in a 1 mm x 1 mm raster from the 3D models of the surfaces. As a function of the specimen size between 5332 and 9744 traces were produced (8400 traces per sample on average). To investigate the differences between this (1) "global" sampling routine and (2) tactile profilometer measurements over the whole length of the samples with a parallel spacing of 10 mm, in Figure 4.9, box plots are given. The elongate, filled (red) boxes stand for the raster-like sampling from the 3D models and the wider, unfilled (blue) boxes summarise the tactile tracing (between 18 and 24 lines per sample). The central markers indicate the median value of the population

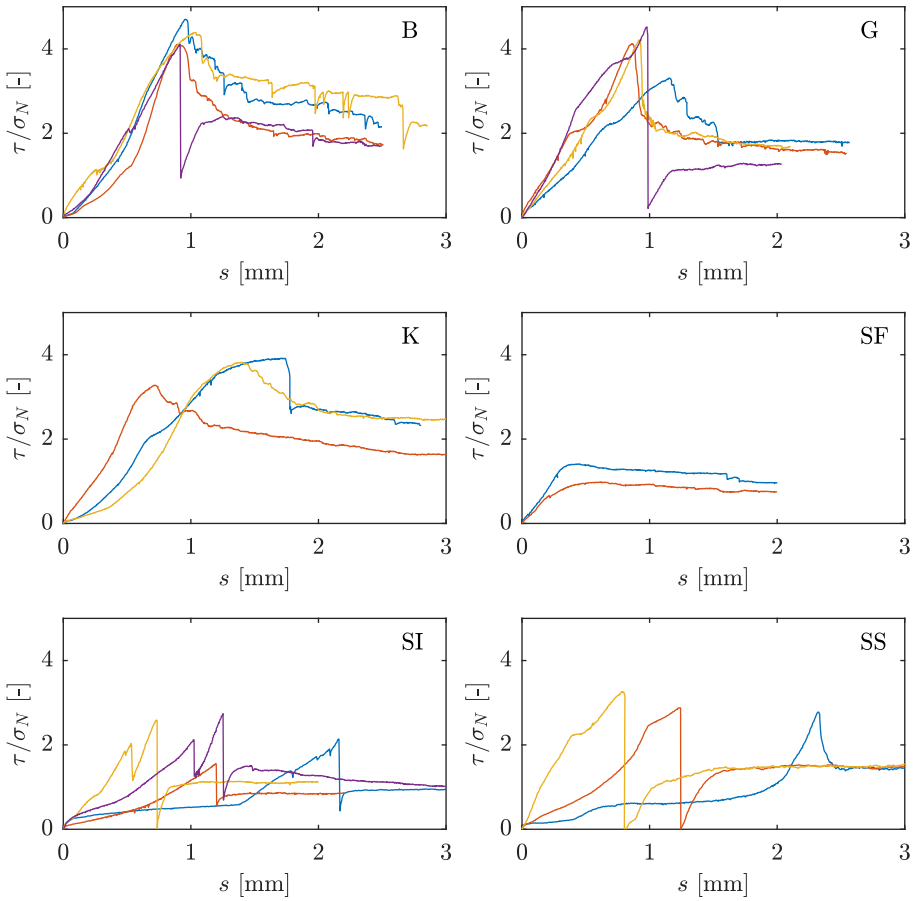

Figure 4.8: Ratio of shear to normal stress plotted versus shear displacement for all 20 direct shear tests separated by rock material

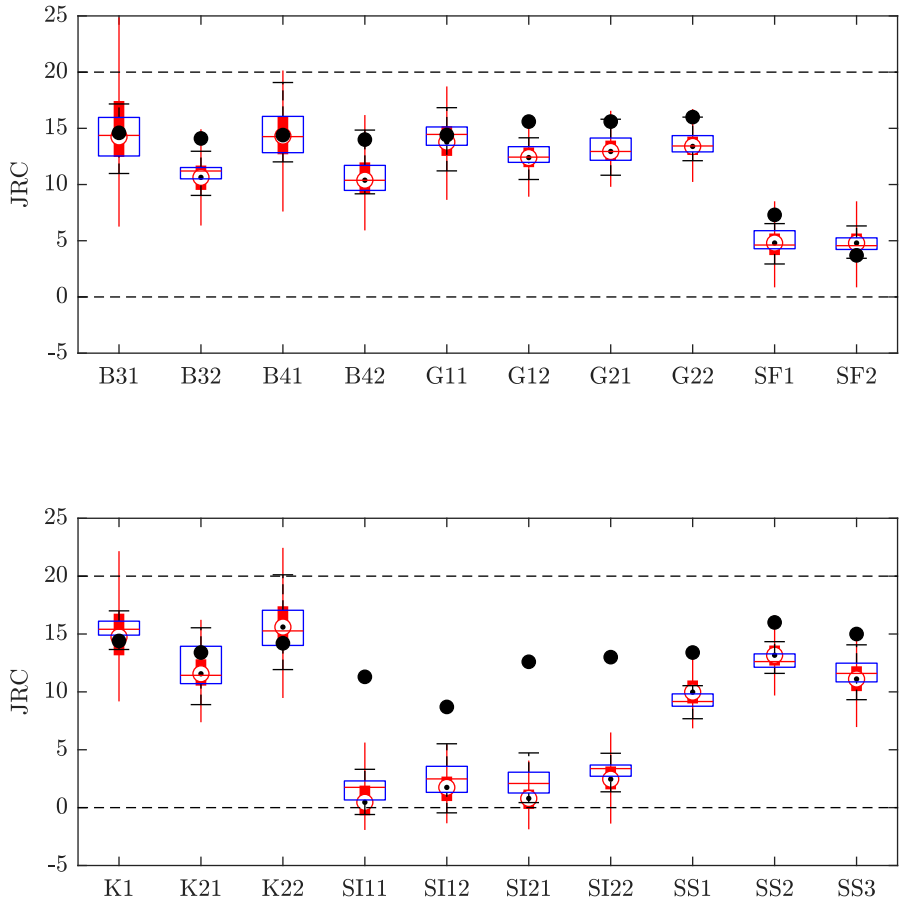

Figure 4.9: Box plots of two different sampling routines for JRC: red boxes show the variation of geometrical JRC derived from point cloud models and blue boxes from tactile measurements - the circles indicate back-calculated JRC values from direct shear tests (dashed lines limit the domain of definition of the JRC concept)

whereas the boxes extend from the 25th to the 75th percentiles. The whisker-ends show extreme data points. For better readability, outliers of the populations are not shown. In general, for the samples of this study, the span of JRC values from standard-length raster sampling is larger than from whole-length tactile measuring: the red whiskers are longer than the black dashed whiskers with end-marks. In some cases, they reach even beyond the domain of definition of the JRC concept undercutting 0 or exceeding 20 (dashed lines). This is particularly the case for the rough samples B and K. In fact, the rougher a surface is, the higher becomes the variance and in consequence a representative sampling or placement of the profile gauge becomes more relevant.

Looking closer at the box sizes in Figure 4.9, apparently, they are very similar for both sampling methods. Also, the median values fit quite well. This was not expected because the ratios of the actual sample lengths to the standard length are between 1.5 and 1.8. According to Barton and Bandis (1982) this would necessitate a correction of the measured JRC. They found that JRC decreases with increasing profile length. On the contrary, from this study it is concluded that for laboratory size samples having up to roughly twice the length of the standard profiles no correction for scale is necessary. This clearly contradicts Barton and Bandis (1982) who, for an exemplary JRC of 15, suggest an increase of JRC of approximately 2 points on this sampling scale. Based on Figure 4.9,

it can be concluded that the application of a tactile profile gauge in parallel spacing of 10 mm on samples being roughly 100 mm wide and having lengths of up to 200 mm leads to a robust estimate of JRC compared to sophisticated and cumbersome profile-based analyses of 3D models.

For comparison, in Figure 4.9 also the back-calculated values of JRC from the direct shear tests are given. It must be kept in mind that somewhat opposing definitions of JRC are compared here: the box plots show the geometrical deduction of JRC based on the type-profiles but the back-calculated JRC from the shear tests are rather fitting parameters with mechanical meaning, implicitly also incorporating the wall strength and the basic friction angle of the rock materials. Especially for samples SI, the differences are significant, and a pronounced effect of the great wall strength is seen: the back-calculated JRC are large although the surfaces are more planar.

The pivotal results of this study are shown in Figure 4.10. There, predicted shear strengths using the selected criteria as of Table 4.3 are compared to results from direct shear tests. Besides the results of this study some data from the previously discussed studies are also shown (see the figure caption for reference).

To begin with considering only the samples of this study, the distribution of the results in the diagrams differ significantly depending on whether the profile-based JRC approach or the area-measured GP method is used. Applying the JRC concept the predicted and measured shear strengths plot rather in a linear band whereas for GP the points are considerably scattered. This is illustrated in detail by means of sample-groups B and SF. Comparably high shear strength is expected for the rough, stepped basalt samples (B) but low strength for the smooth, undulating slates (SF). As anticipated, this is indeed the result from the direct shear tests and also on applying the JRC concept with the criteria from Barton (1973) as well as applying that from Jang et al. (2010), although less pronounced. However, using the original GP criterion from Grasselli and Egger (2003) the predicted shear strengths for sample-groups B and SF arrive at erroneously similar values, contradicting the observations from direct shear tests. The criterion from Tang et al. (2014) instead yields no meaningful results for the samples of this study. Note that the JRC used for the predictions (determined from Equation 4.1 are the mean values from tactile profilometer measurements as described above, considering the whole sample length of 174 mm on average. Furthermore, Jang et al.'s (2010) equation yields lower predicted shear strengths of the rough sample-groups B, G and K compared to Barton's (1973) original equation. Yet, for the low roughness samples SI and SF the results are similar. The reason for this discrepancy is suspected in (1) the narrow selection of samples by Jang et al. (2010) who used replicas of low roughness Gneiss and Schist only and in (2) the replica-based deduction of the equation in general. In summary, for the samples of this study the original JRC-based criterion from Barton (1973) yields the best results in the sense that it is coherent with the different classes of JRC of the test surfaces and (except for the very rough limestone samples K) that it does not overestimate the actual strength.

Looking at the replica data in Figure 4.10, a different picture evolves. In principle, all four criteria used give acceptable results for stress ratios of τ/σ_N approximately smaller 1.5, yet Grasselli and Egger's (2003) formula tends to overestimate the shear strength in that stress ratio range. Instead, for $\tau/\sigma_N > 1.5$ considerable differences between the actual and predicted shear strengths exist. A plausible explanation is that this is due to the calibration of all four criteria using low wall strength materials which fail early and therefore show relatively low shear stress to normal stress ratios. The original JRC-based criterion from Barton (1973) leads to higher predicted strength in many cases whereas

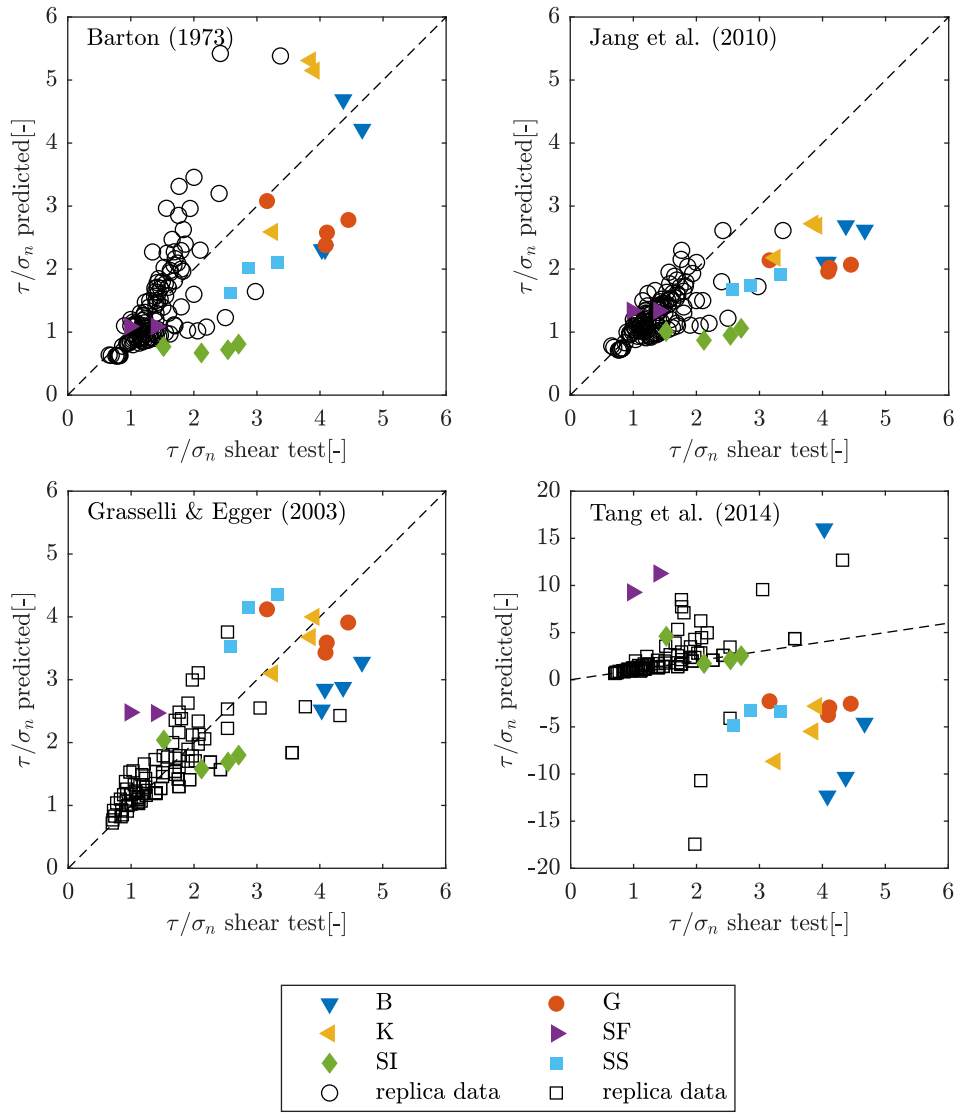

Figure 4.10: Plot of predicted versus measured ratios of shear to normal stress considering the four different empirical criteria as of Table 4.3: JRC-based replica data plotted as black circles is from Jang et al. (2010), Zhang et al. (2016), Casagrande et al. (2018) and Ban et al. (2020), and the black squares represent GP-based data from Fardin (2008), Tatone (2009), Xia et al. (2014) and Tang and Wong (2016) - data from this study is presented as coloured symbols

the results using Jang et al.'s (2010) equation plot near the 1-1-line or below. However, it must be realised that the geometrical JRC used for the prediction of the shear strength have been determined very differently by the respective authors: for example, Ban et al. (2020) used the mean Z_2-derived JRC of 11 profile measurements obtained using a laser scanner whereas Casagrande et al. (2018) give visual JRC values without further explanation. This uncertainty regarding the JRC could be the reason for the differences between predicted and actual shear strength. Regarding the 3D-roughness-based data on the other hand, once again Tang et al.'s (2014) criterion yields implausible (negative) or extremely overestimated shear strength. The results from the original GP-based criterion from Grasselli and Egger (2003) show a cone-like appearance meaning that for relatively high stress ratios the predicted strengths are over- as well as underestimates of the actual strength. Consequently, the predictive capabilities of the two GP-based criteria used here for replica materials are rather limited. For these materials, considering the selected four criteria, Jang et al.'s (2010) equation gives the best results.

In summary and most importantly concerning the usefulness of the JRC and GP approaches for engineering practise, a major disparity exists. On the hand of applying the two JRC-based criteria from Barton (1973) and Jang et al. (2010) to the high strength (real) rocks of this study, in general, an underestimation of the shear strength is seen. Except for the limestone, upon usage of Barton's (1973) original criterion, in Figure 4.10 all other points lie close to or under the 1-1-line. This means that in both cases some safety margin is present. From an engineering point of view, this is advantageous since the predicted results are on the safe side. However, it carries the risk of oversizing of safety measures. On the other hand, using the original GP approach from Grasselli and Egger (2003) leads to a statistically reasonable distribution of the points around equality. However, it also leads to overestimation of the shear strength in roughly 35% of the cases of this study-—regarding safety of design this could be dangerous as unquantified risks can occur. Defining a partial safety factor for GP could reduce risks, yet this cannot be justified based on the small amount of available data in this study. When all this is considered, as mentioned above, Barton's (1973) original criterion is the most reasonable on grounds of discarding replica data. Certainly, it is not perfect but for this relationship the predicted and actual shear strengths are comparably close to each other and/or the predicted values do not exceed the results from direct shear tests. However, for the high strength rock material in this study, significant differences between predicted and actual shear resistance are observed for this criterion as well.

4.5 Discussion

Although an ISRM suggested method for determining the shear strength of rock discontinuities exists many different testing apparatuses, testing procedures and specimen mounting arrangements have been used in the past. This renders uncertainties in comparing different studies and effects the results of this study. Therefore, a more rigid standardisation especially of the encapsulation material and the boundary conditions of the mobile sample half is desirable.

Additionally, no standardisation exists concerning the production of the 3D models from the tested surfaces. For the various studies mentioned before different digitalisation techniques were used and the representations differ in terms of resolution and accuracy. How possible differences can affect deduced roughness parameters was investigated by Marsch et al. (2020) and it is therefore not elaborated here.

Leaving the problems above out of consideration, already the diversity of sample

materials of prior studies entails limitations. All available shear strength criteria clearly rely on their specific sets of samples. This is for example shown in Figure 4.10 upon usage of Tang et al.'s (2014) equation which is inadequate for the samples of this study and also for some referential replica data. Their criterion seems to be overly specific and performs well only for their own replica material. Yet, their criterion and most others are promised to be valid for all types of rock and roughness classes or, at least, mostly no restrictions were reported. It must be considered that the final mathematical formulations rely on the input data and consequently indirectly on (1) the chosen rock or replica material, as well as on (2) the morphological characteristics of the test surfaces. Indeed, this is accounted for in all criteria by means of considering material parameters. However, this also implies that shear strength criteria developed on the basis of specimens covering only a subset of the natural variability, e.g. material strength, may have undiscovered deficits and are therefore limited in their applicability without further verification.

If universal criteria are difficult to achieve, or only at an unacceptable loss of accuracy, perhaps it is also time to look beyond today's rock mechanics view and consider diversifying the portfolio of shear strength criteria. In the field of soil mechanics for example usually different constitutive equations are selected according to the respective soil types. Consequently, also in rock mechanics practitioners could choose the shear strength criterion according to a class of rock types present in the project to be able to better predict strength and deformational behaviour. In cases where no adequate criterion is available, it is preferable to use at least one based on data that covers a wide range of parameters or considers comparable rock groups or roughness.

For a safe and economic design, the best possible agreement between predicted and actual shear strength is of course desired. However, considering the heterogeneous nature of rock material and the consequent uncertainties in the strength parameters, above all, the predicted shear strength should not exceed the actual strength. Only this allows for some safety margin to be present. Indeed, the shear strength could be reduced by means of partial safety factors however, up to date no extensive studies exist from which suggestions on that matter could be drawn.

While the shear behaviour of low strength materials has been investigated often there is a lack of data as well as empirical equations that apply to high strength rock. In principle, as discussed above, Barton's criterion seems to cover also high strength materials. However, there are cases where its predictive capabilities decline: for discontinuities having high wall strength and showing singular prominent asperities, at least under low normal stress, situations arise in which mechanically unclear conditions evolve. They originate in pronounced obstacles that could be termed "nonuniform roughness" and that dominate the shearing process by lever effects and moment forces. Consequently, it is important that the stress conditions of a test case meet the stress conditions under which the particular empirical equation was established. In fact, Barton himself insinuated that there is a problem in using the JRC concept with overly rough surfaces showing nonuniform roughness by rejecting the push-test and tilt-test setups for discontinuities showing JRC values of larger than 12 (c.f. Barton and Choubey, 1977). Apparently, in these cases the boundary conditions of the shear strength equation are not met whereas a clear definition of the area of application was not given. Naturally, rough steps provide a large share of the overall shear resistance especially in competent rock. Current shear strength equations and roughness parameterisations seem to not account for this effect.

4.6 Conclusion

In this study, to investigate the applicability of some existing shear strength criteria, established based on low to medium strength rock or rock like material, a selection of artificial tensile fractures with a mean wall strength $\sigma_C > 230$ MPa was tested in direct shear. For this, basic mechanical descriptions of the rocks used were given along with explanations of the roughness capturing and evaluation routines. Together with the underlying surfaces models, which are available in the repository to this publication (see Marsch, 2021), this allows to fully retrace the results. Finally, the selection process of the shear strength criteria used was described on grounds of a short literature review.

Based on the results of this study it can be concluded that tensile fractures in high strength rock which appear rough on the micro-scale develop large ratios of peak shear stress to normal stress. Values of greater than 3.5 have been observed. This accords well with the observation of predominantly brittle failure of the samples resulting in considerable shear stiffness. Obviously, no replica material published in studies so far shows similar behaviour. The results indicate that the replica-based criteria used are not applicable to estimate the peak shear strength of the high strength rock materials of this study since the differences of predicted and actual shear strength are large.

Additionally, concerning the profile-based concept of JRC it was shown that a correction for scale as of Barton and Bandis (1982) regarding laboratory size samples is unneeded and has no advantage. For the samples of this study being roughly twice the length of the standard profiles the median JRC gathered with a tactile gauge over the whole sample length agree very well with the median JRC of all possible standard-length profiles from a global, quasi 3D analysis.

Most importantly however is the observation that Grasselli's 3D roughness parameter set yields larger predicted than actual shear strength for 35% of the shear tests of this study, even so the statistical fit seems to be better. On the contrary, with the JRC approach an underestimation of the shear strength is seen. Consequently, from an engineering point of view the application of the JRC concept should be preferred since apparently it incorporates a safety margin, yet unquantifiable. Grasselli's 3D roughness parameterisation leads to a more realistic distribution of the shear strength for different morphologies. However, it cannot be applied safely without definition of a partial safety factor. Still, more than 4 decades later, the Barton criterion is still valid in many cases (when care is taken in the estimation of JRC) since the database for establishing the equation is relatively large compared to more recent works and/or ensures good coverage of parameter variability.

For the future, if universal shear strength criteria are not available, specific criteria for specific situations or rock types might be developed, based on larger data sets of direct shear tests accompanied by detailed surface roughness information. Also, it appears reasonable to use only samples from natural materials as the mechanical behaviour of replica materials does not always reflect that of rock.

4.7 Acknowledgements

The authors would like to thank Michael Alber of the Ruhr University at Bochum, Germany who kindly gave permission to use their direct shear testing machine. The guidance in the laboratory by Ferdinand Stöckert was greatly appreciated. This study was supported by internal funds of the TU Berlin.

4.8 Appendix

Table 4.D: Framework of selected shear strength studies

Reference	(Rock) Material	Strength			Normal Stress	No. of tests	Roughness Metric	Notes
		σ_C [MPa]	σ_T [MPa]	ϕ_b [°]	[MPa]			
Barton and Choubey (1977)	Slate	/	/	/	0.05–1.5	7	JRC defining study	No roughness data
	Aplite	/	/	31		36		
	Gneiss	/	/	30		17		
	Granite	88	/	33		38		
	Hornfels	64	/	34		17		
	Soapstone	/	/	19		5		
	Shale	/	/	28		15		
Kulatilake et al. (1995)	Concrete	4	/	24	0.05–1.0	60	2D statistical and fractal approaches	No roughness data, 3 morphologies tested in various directions
	Concrete	4	/	24		60		
	Concrete	11	/	30		60		
Grasselli and Egger (2003)	Sandstone	10	0.7	37	0.9–4.1	3	GP (A_0, θ^*_{max}, C) defining study	
	Limestone	25	2.4	36		7		
	Marble	87	9.2	37		11		
	Granite	173	8.8	34		7		
	Serpentinite	166	6.0	39		2		
	Gneiss	184	9.5	36		7		
Fardin (2008)	Concrete	215	9.1	33	1.0–10.0	16	GP	
Tatone (2009)	Mortar	20	1.5	32	0.15–0.94	18	GP	
Jang et al. (2010)	Cement	52	/	31	0.05–0.5	72	JRC (based on Z_2)	
Xia et al. (2014)	Mortar	28	1.5	35	0.5–3.0	15	GP	

Continuation of Table 4.D

Reference	(Rock) Material	Strength			Normal Stress	No. of tests	Roughness Metric	Notes
		σ_C [MPa]	σ_T [MPa]	ϕ_b [°]	[MPa]			
Tang and Wong (2016)	Mortar	28	1.5	35	0.2–3.0	25	GP	
	Mortar	16	1.4	31		10		
	Mortar	5	0.6	25		10		
Yang et al. (2016)	Granite	161	8.8	34	0.3–8.0	10	GP	
	Sandstone	65	2.6	28		10		
Zhang et al. (2016)	Cement	35	1.1	35	0.5–3.0	15	new 2D approach	
Dong et al. (2017)	Marble I	142	15.1	31	3.9–17.9	6	new 3D approach	
	Marble II	71	17.3	36		6		
	Marble III	65	13.0	36		6		
	Marble IV	48	10.3	37		6		
	Sandstone	78	3.8	30		6		
Casagrande et al. (2018)	Mortar	40	/	35	0.1–6.0	18	JRC (visual)	
Liu et al. (2018)	Mortar	22	0.9	31	0.5–3.0	25	JRC (new approach)	
Ban et al. (2020)	Cement	29	/	33	0.5–2.0	20	Pseudo 3D (new approach)	

4.9 References

Alameda-Hernández, P., Jiménez-Perálvarez, J., Palenzuela, J. A., Hamdouni, R. E., Irigaray, C., Cabrerizo, M. A., and Chacón, J. (2014). Improvement of the JRC calculation using different parameters obtained through a new survey method applied to rock discontinuities. *Rock Mech Rock Eng*, 47(6):2047–2060. https://doi.org/10.1007/s00603-013-0532-2.

Alejano, L., Muralha, J., Ulusay, R., Li, C., Pérez-Rey, I., Karakul, H., Chryssanthakis, P., and Aydan, O. (2018). ISRM suggested method for determining the basic friction angle of planar rock surfaces by means of tilt tests. *Rock Mech Rock Eng*, 51(12):3853–3859. https://doi.org/10.1007/s00603-018-1627-6.

Babanouri, N., Asadizadeh, M., and Hasan-Alizade, Z. (2020). Modeling shear behavior of rock joints: A focus on interaction of influencing parameters. *Int J Rock Mech Min*, 134:104449. https://doi.org/10.1016/j.ijrmms.2020.104449.

Ban, L., Qi, C., Chen, H., Yan, F., and Ji, C. (2020). A new criterion for peak shear strength of rock joints with a 3d roughness parameter. *Rock Mech Rock Eng*, 53(4):1755–1775. https://doi.org/10.1007/s00603-019-02007-z.

Bandis, S., Lumsden, A., and Barton, N. (1981). Experimental studies of scale effects on the shear behaviour of rock joints. *Int J Rock Mech Min*, 18(1):1–21. https://doi.org/10.1016/0148-9062(81)90262-x.

Barton, N. (1973). Review of a new shear-strength criterion for rock joints. *Eng Geol*, 7(4):287–332. https://doi.org/10.1016/0013-7952(73)90013-6.

Barton, N. and Bandis, S. (1982). Effects of block size on the shear behavior of jointed rock. *Proceedings 23rd Symp. Rock Mechanics, August 25-27, 1982, Berkeley, CA*.

Barton, N. and Choubey, V. (1977). The shear strength of rock joints in theory and practice. *Rock Mech*, 10(1-2):1–54. https://doi.org/10.1007/bf01261801.

Casagrande, D., Buzzi, O., Giacomini, A., Lambert, C., and Fenton, G. (2018). A new stochastic approach to predict peak and residual shear strength of natural rock discontinuities. *Rock Mech Rock Eng*, 51(1):69–99. https://doi.org/10.1007/s00603-017-1302-3.

Dong, H., Guo, B., Li, Y., Si, K., and Wang, L. (2017). Empirical formula of shear strength of rock fractures based on 3d morphology parameters. *Geotechnical and Geological Engineering*, 35(3):1169–1183. https://doi.org/10.1007/s10706-017-0172-5.

Fardin, N. (2008). Influence of structural non-stationarity of surface roughness on morphological characterization and mechanical deformation of rock joints. *Rock Mech Rock Eng*, 41(2):267–297. https://doi.org/10.1007/s00603-007-0144-9.

Gehle, C. and Kutter, H. (2003). Breakage and shear behaviour of intermittent rock joints. *Int J Rock Mech Min*, 40(5):687–700. https://doi.org/10.1016/s1365-1609(03)00060-1.

Grasselli, G. and Egger, P. (2003). Constitutive law for the shear strength of rock joints based on three-dimensional surface parameters. *Int J Rock Mech Min*, 40(1):25–40. https://doi.org/10.1016/s1365-1609(02)00101-6.

Grasselli, G., Wirth, J., and Egger, P. (2002). Quantitative three-dimensional description of a rough surface and parameter evolution with shearing. *Int J Rock Mech Min*, 39(6):789–800. https://doi.org/10.1016/s1365-1609(02)00070-9.

Hencher, S. and Richards, L. (2015). Assessing the shear strength of rock discontinuities at laboratory and field scales. *Rock Mech Rock Eng*, 48(3):883–905. https://doi.org/10.1007/s00603-014-0633-6.

ISRM (1978a). Suggested methods for determining tensile strength of rock materials. *Int J Rock Mech Min*, 15(3):99–103. https://doi.org/10.1016/0148-9062(78)90003-7.

ISRM (1978b). Suggested methods for the quantitative description of discontinuities in rock masses. *Int J Rock Mech Min*, 15(6):319–368. https://doi.org/10.1016/0148-9062(78)91472-9.

ISRM (1979). Suggested methods for determining the uniaxial compressive strength and deformability of rock materials. *Int J Rock Mech Min*, 16(2):137. https://doi.org/10.1016/0148-9062(79)91450-5.

Jang, B.-A., Kim, T.-H., and Jang, H.-S. (2010). Characterization of the three dimensional roughness of rock joints and proposal of a modified shear strength criterion. *Journal of Engineering Geology*, 20(3):319–327.

Kim, D. H., Poropat, G. V., Gratchev, I., and Balasubramaniam, A. (2015). Improvement of photogrammetric JRC data distributions based on parabolic error models. *Int J Rock Mech Min*, 80:19–30. https://doi.org/10.1016/j.ijrmms.2015.09.007.

Kulatilake, P., Shou, G., Huang, T., and Morgan, R. (1995). New peak shear strength criteria for anisotropic rock joints. *Int J Rock Mech Min*, 32(7):673–697. https://doi.org/10.1016/0148-9062(95)00022-9.

Ladanyi, B. and Archambault, G. (1970). Simulation of shear behavior of a jointed rock mass. *Proceedings 11th Symp. Rock Mechanics, June 16-19, 1969, Berkeley, CA*.

Lee, Y.-K., Park, J.-W., and Song, J.-J. (2014). Model for the shear behavior of rock joints under CNL and CNS conditions. *Int J Rock Mech Min*, 70:252–263. https://doi.org/10.1016/j.ijrmms.2014.05.005.

Li, Y. and Huang, R. (2015). Relationship between joint roughness coefficient and fractal dimension of rock fracture surfaces. *Int J Rock Mech Min*, 75:15–22. https://doi.org/10.1016/j.ijrmms.2015.01.007.

Li, Y., Mo, P., Aydin, A., and Zhang, X. (2019). Spiral sampling method for quantitative estimates of joint roughness coefficient of rock fractures. *Geotech Test J*, 42(1):245–255. https://doi.org/10.1520/gtj20170213.

Li, Y., Tang, C., Li, D., and Wu, C. (2020). A new shear strength criterion of three-dimensional rock joints. *Rock Mech Rock Eng*, 53(3):1477–1483. https://doi.org/10.1007/s00603-019-01976-5.

Li, Y. and Zhang, Y. (2015). Quantitative estimation of joint roughness coefficient using statistical parameters. *Int J Rock Mech Min*, 77:27–35. https://doi.org/10.1016/j.ijrmms.2015.03.016.

Liu, Q., Tian, Y., Ji, P., and Ma, H. (2018). Experimental investigation of the peak shear strength criterion based on three-dimensional surface description. *Rock Mech Rock Eng*, 51(4):1005–1025. https://doi.org/10.1007/s00603-017-1390-0.

Magsipoc, E., Zhao, Q., and Grasselli, G. (2020). 2d and 3d roughness characterization. *Rock Mech Rock Eng*, 53(3):1495–1519. https://doi.org/10.1007/s00603-019-01977-4.

Marsch, K. (2021). Surface models and profiles from a rock joint shear strength study. https://doi.org/10.14279/depositonce-12280.

Marsch, K. and Fernandez-Steeger, T. M. (2021). Comparative evaluation of statistical and fractal approaches for JRC calculation based on a large dataset of natural rock traces. *Rock Mech Rock Eng*, 54(4):1897–1917. https://doi.org/10.1007/s00603-020-02348-0.

Marsch, K., Wujanz, D., and Fernandez-Steeger, T. M. (2020). On the usability of different optical measuring techniques for joint roughness evaluation. *B Eng Geol Environ*, 79(2):811–830. https://doi.org/10.1007/s10064-019-01606-y.

Muralha, J., Grasselli, G., Tatone, B., Blümel, M., Chryssanthakis, P., and Yujing, J. (2014). ISRM suggested method for laboratory determination of the shear strength of rock joints: Revised version. *Rock Mech Rock Eng*, 47(1):291–302. https://doi.org/10.1007/s00603-013-0519-z.

Myers, N. (1962). Characterization of surface roughness. *Wear*, 5(3):182–189. https://doi.org/10.1016/0043-1648(62)90002-9.

Patton, F. (1966). Multiple modes of shear failure in rock. *Proceedings 1st ISRM Congress, September 25 - October 1, Lisbon, Portugal*.

Singh, H. and Basu, A. (2018). Evaluation of existing criteria in estimating shear strength of natural rock discontinuities. *Eng Geol*, 232:171–181. https://doi.org/10.1016/j.enggeo.2017.11.023.

Tang, Z.-C., Liu, Q.-S., and Huang, J.-H. (2014). New criterion for rock joints based on three-dimensional roughness parameters. *J Cent South Univ*, 21(12):4653–4659. https://doi.org/10.1007/s11771-014-2473-7.

Tang, Z.-C. and Wong, L. N. Y. (2016). New criterion for evaluating the peak shear strength of rock joints under different contact states. *Rock Mech Rock Eng*, 49(4):1191–1199. https://doi.org/10.1007/s00603-015-0811-1.

Tatone, B. S. (2009). Quantitative characterization of natural rock discontinuity roughness in-situ and in the laboratory. Master's thesis, University of Toronto.

Tatone, B. S. and Grasselli, G. (2009). A method to evaluate the three-dimensional roughness of fracture surfaces in brittle geomaterials. *Rev Sci Instrum*, 80(12):125110. https://doi.org/10.1063/1.3266964.

Tatone, B. S. and Grasselli, G. (2010). A new 2d discontinuity roughness parameter and its correlation with JRC. *Int J Rock Mech Min*, 47(8):1391–1400. https://doi.org/10.1016/j.ijrmms.2010.06.006.

Tian, Y., Liu, Q., Liu, D., Kang, Y., Deng, P., and He, F. (2018). Updates to grasselli's peak shear strength model. *Rock Mech Rock Eng*, 51(7):2115–2133. https://doi.org/10.1007/s00603-018-1469-2.

Vogler, D., Walsh, S. D., Bayer, P., and Amann, F. (2017). Comparison of surface properties in natural and artificially generated fractures in a crystalline rock. *Rock Mech Rock Eng*, 50(11):2891–2909. https://doi.org/10.1007/s00603-017-1281-4.

Xia, C.-C., Tang, Z.-C., Xiao, W.-M., and Song, Y.-L. (2014). New peak shear strength criterion of rock joints based on quantified surface description. *Rock Mech Rock Eng*, 47(2):387–400. https://doi.org/10.1007/s00603-013-0395-6.

Yang, J., Rong, G., Hou, D., Peng, J., and Zhou, C. (2016). Experimental study on peak shear strength criterion for rock joints. *Rock Mech Rock Eng*, 49(3):821–835. https://doi.org/10.1007/s00603-015-0791-1.

Zhang, X., Jiang, Q., Chen, N., Wei, W., and Feng, X. (2016). Laboratory investigation on shear behavior of rock joints and a new peak shear strength criterion. *Rock Mech Rock Eng*, 49(9):3495–3512. https://doi.org/10.1007/s00603-016-1012-2.

Chapter 5

Synthesis

Estimating the shear strength of rock discontinuities is vital to the design of rock engineering structures as the strength of rock masses is predominantly determined by the mechanics of their structural inventory. As means to avoid direct shear testing at least 25 empirical shear strength criteria are available in the literature (c.f. Singh and Basu, 2018; Li et al., 2020). They all rely on strength parameters for the rock material and surface roughness as input parameters. Little dispute exists on the selection and the determination of the wall strength parameters, at least for unweathered rocks. However, the discussion on how to quantify the roughness component is ongoing: common procedures consider profiles whereas lately more and more criteria using three-dimensional measures were published.

Naturally, to quantify roughness the surfaces must be captured and sampled in some way. Due to rapidly increasing availability of highly capable metrology systems and Structure-from-Motion workflows (c.f. Abellan et al., 2016; Eltner et al., 2016), more often very detailed representations of the surfaces are produced. No standard procedures have been formulated yet and consequently prior studies are difficult to compare.

Regarding roughness quantification, both for 2D and 3D statistical and fractal approaches are delineated (c.f. Magsipoc et al., 2020). Parametric statistical approaches are straightforward and easy to implement, whereas fractal methods are often complex. As recently, it was realised that the use of fractal theory is helpful for roughness determination only if the calculation schemes yield the Hurst exponent and additionally an amplitude parameter (c.f. Magsipoc et al., 2020; Stigsson and Mas Ivars, 2019).

In the introduction of this thesis the question was asked whether the use of elaborate roughness parametrisations and sophisticated measuring devices is beneficial for shear strength estimation. The notion of "elaborate roughness parameterisations" applies specifically to fractal approaches since for their safe usage a deeper understanding of the theory of fractals is needed as well as a thorough knowledge of the crucial setscrews in the involved algorithms. Also, 3D approaches are considered elaborate since they require spatial surface models. The appellation of "sophisticated measuring devices" refers to those machines that are costly, sensitive to interference from outside (vibration, lighting, dust, etc.) and logistically demanding. It also extends to those surveying techniques that yield very detailed representations of rock joints in terms of resolution and accuracy. In appreciation of the overall goal of estimating the shear strength of rock joints practitioners need to robustly measure and parameterise roughness as inputs for empirical strength criteria and to have a sense of which criterion is most useful. For these goals this thesis offers the following condensed conclusions:

- Structure-from-Motion/Dense Image Matching produces surface representations suitable for roughness evaluation. It is a reliable means also on millimetre-scale in case a norm is present in the object space for metric referencing. Industry metrology systems are unneeded. (This finding is especially valuable because SfM/DIM is highly versatile and used easily in the field.)
- Type-profile based JRC are determined most safely by statistical correlations using Z_2. Fractal RMS-correlation is applicable but comes with the cost of higher complexity and uncertainty. Fractal power spectrum analysis is defective in this context. Overall, fractal approaches do not improve JRC calculation.
- Shear strength criteria based on Grasselli's 3D parameter may yield realistic but unsafe estimates of the shear strength for some high strength rock material used in this study. For these particular cases, from an engineering point of view, Barton's original 2D concept of JRC and using a tactile profilometer is not inferior to modern approaches.

These shortened findings are based on the detailed studies of chapters 2, 3 and 4. As they refer to components of the establishment of shear strength criteria, these insights are valuable for future works. To substantiate the list above, in the following, the specific results of the self-contained papers are summarised under consideration of the overarching questions of this thesis.

5.1 Interdependence of roughness measurement and parameterisation

Historically, the subject of rock roughness evaluation has been approached from two sides: (i) having surface representations (i.e. traces or 3D models) at hand that shall be parameterised, or (ii) wishing to apply a theoretical, geometrical framework to representations that are yet to be captured. Figure 5.1 depicts these thoughts. Without doubt, the somewhat retroactive parameterisation of the JRC, being the quasi standard for roughness quantification (c.f. ISRM, 1978; ISO 14689, 2017), falls in the first category. Tse and Cruden (1979), and the many others thereafter, simply used the traces published by Barton and Choubey (1977). Instead, Grasselli (2001) moved rather proactively and defined his roughness parameter first and then accordingly selected the measuring approach.

Naturally, in both cases the final roughness index for a surface image must be viewed as a combination of the two aspects, namely geometric input data and parameterisation. Ignoring deficiencies of one of the other will inevitably result in a wrongful estimation of roughness and ultimately in a wrongful estimation of shear strength. That is why chapter 2 deals with the production of the input data and shortcomings of some ready-to-use packages of optical measuring approaches, thereby revealing contradictions between statistical and fractal roughness parameterisation, whereas chapter 3 readopts these contractions and especially gives attention to the deficiencies of fractal roughness evaluation.

Regarding the geometric input data, in chapter 2, the resolution and accuracy of the final surface meshes produced using four different optical measuring techniques are evaluated. The measurements from industry standard, stationary SLS (stand.SLS) serve as the reference for the outcomes of handheld SLS (hand.SLS), TLS and SfM/DIM. All devices and software used for this thesis are proprietary commercial systems in respect of which their dealing with noise and outliers are incomprehensible and calculation of errors remains impractical. Their final outcomes must be taken as they are, which

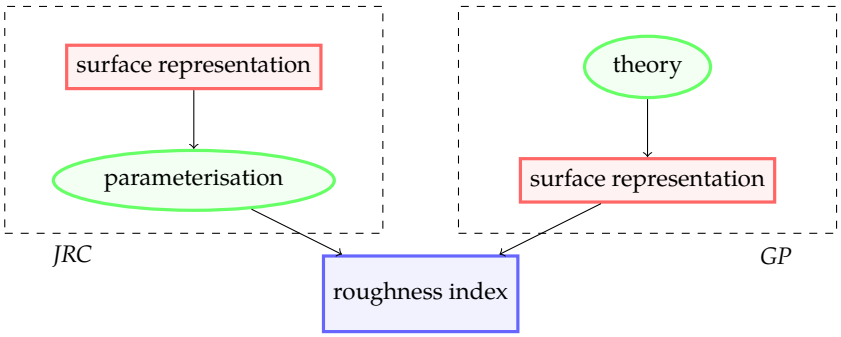

Figure 5.1: Two ways of approaching rock roughness

is however common practise in shear strength studies (e.g. Grasselli and Egger, 2003; Dong et al., 2017; Liu et al., 2018). Yet this uncritical, even unscrupulous use without knowing the margins of error impacts on the roughness quantification. In case the input data is defective, empirical connections built on that would also be flawed. Moreover, in past studies mostly only the theoretical resolution and accuracies based on the manufacturer's data sheets were given, yet these sheets only specify the resolution of elementary observations, meaning the ones of individual sensor components. Instead, for the first-time concerning roughness determination, in chapter 2, numbers for the achievable resolution and accuracy of the recorded outcome are given thereby establishing a benchmark for the quality of models from other studies. Based on the transformation of the models into one coordinate system and aligning them using an ICP algorithm, in a first step, the 3D deviations of the models are calculated. For three exemplary surfaces hand.SLS yields the lowest standard spatial deviations of 0.09 mm on average and with TLS the largest deviations ranging from 0.23 to 0.57 mm are obtained. SfM/DIM give results somewhat in-between (0.08 and 0.13 mm). However, such a simple geometrical evaluation is not constructive because it is practically impossible to capture the same exact points on a surface by different devices due to their varying technical specifications. Consequently, the uncertainty of the transformation into one coordinate system is large. Therefore, in a second step, the models are evaluated based on the statistics of the deduced JRC and GP. This gives a different picture: compared to the reference the roughness measures originating from hand.SLS now deviate, and in case of TLS they deviate substantially. Moreover, no universal rule can be established such as that roughness determined from these two methods is systematically lower or higher than values derived from the reference data. Roughness quantified based on hand.SLS and TLS is rather erratic and concerning TLS depends heavily on the texture and radiometric properties (bright colour and penetrable quartz grains) of the surfaces in question. On the contrary DIM accords excellently with the reference for all tested surfaces. In summary, TLS is unable to capture second-order roughness (even more so true for field-use) and hand.SLS, with some trade-off, bridges the gap to stat.SLS and SfM/DIM. Concerning handheld SLS, stationary SLS and SfM/DIM, all methods can be used as replacement for tactile profilometry. Besides the most important outcome, which is that SfM/DIM gives results equivalent to industry-standard structured light scanners – this has high relevance because practically everyone can produce high quality models now – chapter 2 reveals that some statistical and fractal roughness parameterisations result in very different JRC. However, due to the referencing of all JRC correlations to the type-profiles, also for all other traces the deduced JRC should be equal. In natural ways, this inconsistency gives birth to the topic of chapter 3.

Due to the importance of the input data as discussed in chapter 2, at first in chapter 3 the original type-profiles are revisited. The focus is directed towards the effect of ignoring the indisputable deficiencies of the type-profiles, i.e. their inferior quality in terms of the unquantified uncertainty and resolution of the measurement. Based on three openly available digitalisations of the standard chart from Tatone (2009), Li and Zhang (2015) and Stigsson and Mas Ivars (2019), which are used to avoid possible transcription errors upon once again re-digitalisation and to enhance comparability, the sensitivity to that input data of some statistical and fractal measures is investigated. On the side of the statistical approaches Z_2 serves as a proxy: for the type-profiles meaningful transfer-functions to other statistical parameters are found. Irrespective of the dataset, the Z_2 method yields very similar results, in which simple rotational detrending, using the mean line of each profile derived from linear-least squares regression, and 1 mm sampling intervals are the only requirements. Instead, on the side of the fractal approaches RMS-correlation, power-spectral analysis (FFT) and compass walking are applied. Regarding RMS-correlation, the particular digitalisation of the type-profiles has little effect. On the contrary, power spectral analysis is very sensitive to the input data and significant variation is seen depending on the data sets used. In this context it must be kept in mind that the high frequencies dominate the power spectrum, yet, they are absent in the low-resolution and heavily filtered type-profiles (profile gauges capture only the highest point in the interval). This could explain the large errors concerning the deduced JRC. Obviously, gathering more meaningful data in the first place, fitting the needs of the roughness parameterisation to be used, would resolve that problem. Remember, how high-resolution data with sufficient accuracy can be recorded is discussed in chapter 2. Although, compass walking was denoted inapplicable to rock roughness (c.f. Schmittbuhl et al., 1995), it is the fractal method used most so far (c.f. Li and Huang, 2015) and is therefore used here as well. A large sensitivity of the method to the pre-set compass radii is seen. Already, the reevaluation of the fractal approaches considering only the type-profiles leads to doubts concerning their usefulness. Consequently, a cross-validation on independent data of all calculation schemes mentioned afore is performed. The hypothesis is to be tested whether irrespective of the specific parameterisation the same JRC result. Indeed, this is a requirement as all correlations refer to the type-profiles. Six rock surface representations are sampled using the sliding window approach. This way scale effects are avoided because only standard-length profiles, namely 100 mm, are considered. Moreover, tracing all possible standard-length profiles on a surface overcomes sampling bias which is a major argument against profile-based roughness description (c.f. Li et al., 2019). This "global" sampling is used throughout the works of this thesis. Based on this data, the cross-validation affirms that compass walking is inadequate for rock roughness evaluation. Additionally, spectral analysis results in huge differences with respect to Z_2 and RMS-correlation. With this method especially the detrending routine and the selection of the sampling window are potential sources of error. On the contrary, regarding Z_2 and RMS very good accordance is seen. The results mentioned afore apply to profiles sampled at 1 mm intervals, which is a requirement for the use of JRC correlations in general due to the initial measurement quality of the standard chart. Most importantly, for this specific sampling interval the asperity measure $\sigma\delta h(1\text{mm})$ and Z_2 are equal. In the FFT and RMS-COR algorithms the asperity measure is derived graphically from the y-axis intercept of a linear regression in log-log space which is naturally imprecise. In case of RMS-correlation this graphical process leads to close numbers for $\sigma\delta h(1\text{mm})$ and Z_2, yet in case of spectral analysis it does not. $\sigma\delta h(1\text{mm})$ however has a large effect on JRC as it dominates over the Hurst exponent

by more than one magnitude in the equation from Stigsson and Mas Ivars (2019). Their JRC correlation is the only available fractal formula that takes account of the self-affine nature of rock traces, however, due to the equality of Z_2 and $\sigma\delta h(1\text{mm})$ it must be considered rather yet another statistical equation with additional uncertainty. Overall, due to high error-proneness fractal calculation schemes are unneeded for JRC correlation.

Collectively, the chapters 2 and 3 point at the interdependence of roughness measurement and roughness parameterisation thereby focusing on the most common JRC. This investigation is important because the practice to re-digitise the type-profiles over and over again and to correlate more and more measures with them (e.g. Ficker and Martišek, 2016; Wang et al., 2017; Yong et al., 2018; Gravanis and Pantelidis, 2019) is ongoing. Yet, the low quality of the standard chart is neglected continuously. In summary, on grounds of the conducted cross-validation and regarding the sparse and low-resolution type-profiles, using sensitive fractal calculation schemes, such as spectral analysis, is senseless. However, now broadly available SfM/DIM-derived surface models open way for better roughness parameterisation and, in conjunction with new reference profiles or referential surface data, could lead to better estimates of JRC, maybe even upon usage of fractal approaches.

5.2 2D vs. 3D roughness characterisation for high strength rock materials

The understanding in this thesis is that research on the topic of roughness characterisation should not remain on a theoretical basis since it is the primary goal to estimate actual shear resistance. Conducting direct shear tests, as of chapter 4, for validation of roughness parameterisation is utterly necessary. In many prior studies only low-strength replica materials were used (e.g. Kulatilake et al., 1995; Lee et al., 2014; Ban et al., 2020). Consequently, in the study of chapter 4 high strength rocks are used to investigate whether the extrapolation of results is admissible. Additionally, the best-practise, good enough rules concerning the determination of the JRC established in chapters 2 and 3 are tested against Grasselli's 3D roughness.

Upon reviewing more than ten shear strength studies (of which many led to the establishment of shear strength criteria) it seems to exist a lower bound of the shear strength for normal stresses smaller than 2.5 MPa. Most prior test results plot above a Mohr-Coulomb line with null cohesion and a friction angle of 32°. Consequently, this value can be used for a first approximation in design together with the suggested maximal friction angle of 70° postulated by Barton and Choubey (1977). Most interestingly the lower bound of 32° is irrespective of the particular wall strength and wall roughness of the rock or replica materials tested. This also applies to all rocks tested in chapter 4 of this thesis, yet, for the rough samples friction angles of even greater than 70° are obtained.

Concerning the measurement of the profiles for JRC two sampling routines are applied. On one hand, profiles are gathered over the whole length of the laboratory samples by means of a tactile profilometer. This follows Barton's original sampling approach and results in 18 to 24 measurements per sample with spacings of approximately 1 cm. On the other hand, the already mentioned "global" sampling approach (to avoid scale effects) is employed which leads to 8400 standard-length traces per sample on average. As results, it is seen that the "global" sampling yields very much larger spans of JRC_{Z_2} but the interquartile ranges (middle 50% of the population) and median values accord very well for both sampling routines. Consequently, correction for scale as suggested by

Barton and Bandis (1982) is unnecessary as well as cumbersome extraction of profiles from 3D models.

For the three-dimensional roughness characterisation GP is used as it is established and incorporated in many shear strength criteria (c.f. Li et al., 2020). For the comparison of predicted with test-derived shear strength, in both cases of using JRC and GP, the original criteria from Barton and Choubey (1977) and Grasselli and Egger (2003) are considered, accompanied by one alternative, more recent criterion, namely the JRC-based equation from Jang et al. (2010) and the GP-based equation from Yang et al. (2016). One major outcome is the general disparate distribution of the predicted shear strength regarding the use of JRC and GP. In principal, it is expected that rough samples yield comparably higher shear strength than smooth samples. The direct shear tests indeed affirm this assumption and so do the JRC-based criteria. However, using GP-based approaches the picture is not that apparent. There, the predicted values show considerable scatter and no clear relationship between roughness and shear strength is observed. Additionally, the original criteria produce better results than the two exemplary recent criteria. However, no indication is found that the applied criteria should not be used for high strength rocks. Most importantly, in 35% of the test cases the shear strength is overestimated upon usage of the GP approach. In summary, Grasselli's three-dimensional parameter is theoretically superior to the JRC concept because it considers the whole surface, however, its usefulness regarding the samples tested in this study is limited. Consequently, tracing profiles in spacings of 1 cm over the whole sample length with a tactile profile gauge and calculating the JRC based on Z_2 is still valuable because it yields safe estimates of the shear strength at least for the tension fractures considered in chapter 4.

Although, the test results suggest the criteria used here being more or less applicable to high strength materials, their predictive capabilities decline when singular prominent asperities are present. This "nonuniform roughness" in conjunction with the low normal stresses applied entail mechanically unclear conditions: the contact area of the samples halves dwindles to these pronounced obstacles. The results are lever effects and moment forces that are yet not quantifiable. Apparently, present roughness parameterisations do not account for "nonuniform roughness" as the methods compress the geometrical information into only one parameter.

5.3 Discussion and outlook

Geometric benchmarks When dealing with roughness characterisation for shear strength estimation, as mentioned in the introduction, engineers fall back to the suggested methods of the ISRM (1978) and Barton's type-profiles (Barton and Choubey, 1977). Still, more than 40 years after their publication they are the only benchmarks available and because of the lack of alternatives researchers and practitioners still rely on them. However, it is shown in chapter 3 that the usefulness of the type-profiles is limited. Consequently, there is an urgent need for better openly available geometric preferentially spatial representations that can be linked to direct shear test data. Unfortunately, even for more recent roughness parameterisation approaches such as the 3D approach from Grasselli et al. (2002) no geometric inputs were provided. For studies to come, colleagues are strongly advised to make all their data available.

Sample population In prior works only small amounts of rock samples were tested in direct shear. The effects of small sample populations are touched in chapter 4, where

also numbers of samples and their lithology are listed for some prior publications. It must be realised that establishing empirical criteria based on small sample sizes will lead to equations that very narrowly trace the underlying data. This is to be described as overfitting. This fact is clearly demonstrated in chapter 4 where significant differences of predicted and actual shear strength upon application of some criteria are found. There are two ways out of this dilemma; (i) extending the data space drastically which means testing as much rock joints with different genetic histories as possible, or (ii) developing criteria whose application are strictly limited to certain cases. It could be useful to come up with categories for shear strength criteria according to the rock material or roughness classes to which they apply. A similar approach is used for example in soil mechanics where constitutive equations are geared to the soil types. In rock mechanics instead, the practise of creating more and more criteria with only minor changes but claiming their broad applicability, or at least not restricting their field of application rigorously, should be put to an end. Certainly, in chapter 4 also an unsatisfactory small amount of only 20 samples are tested, however, due to the reasons described, creating yet another shear strength criterion is refrained from.

Surveying accuracy and resolution Naturally different measuring techniques and devices due to their intrinsic properties produce differing representations of the same surface (see chapter 2). To achieve a minimum of comparability of the outcomes and subsequently meaningful, objective, and robust small-scale roughness parameterisation, in the near future, some basic demands on the surveying equipment should be formulated. Besides the accuracy and resolution also the post-processing routines of the original point cloud measurement, namely the dealing with outliers and noise, must be considered. Remembering that the only accepted roughness quantification approach, the JRC, relies on 1 mm point intervals, a minimum resolution of 0.5 mm seems sufficient according to the Nyquist–Shannon sampling theorem. Concerning the accuracy, one magnitude smaller than the pursued resolution, consequently 0.1 mm, could be sufficient. Regarding the use of SfM/DIM for JRC estimation most recently García-Luna et al. (2021) give information on the achievable resolution in the field. However, more systematic studies are needed which should also consider the needs of other roughness parameterisations.

Scale This thesis focuses explicitly on laboratory-size samples. It should not be forgotten that rock joints are natural materials: already, in small segments within a rock mass the roughness will vary by nature. Consequently, investing much effort in surveying small areas with high accuracy and high resolution could be unneeded. The ISRM has a clear opinion on that:

> "Several automatic recording profilographs are described in the literature [...]. Most of these are suitable for describing the finest details of roughness. They obviously give a much more accurate picture [...]. Normally this accuracy is unnecessary for rock mechanics purposes." ISRM (1978)

Upon reviewing studies on shear strength thereby focusing on scale effects Bahaaddini et al. (2014) pointed out contradictive result: positive as well as negative correlation of scale and roughness were found. Yet, their own study used numerical models of also only 40 cm length which is similar to the sample sizes used by Bandis et al. (1981). Bandis' works regarding JRC are in general an often-cited source for effects of scale on shear strength. More recent studies (e.g. Liu et al., 2020; Huang et al., 2020) consider samples

of up to 1 m, however, it remains an open issue how roughness for rock engineering purposes should be characterised on larger, in-situ scales of several metres.

Rock mass modelling As in many other engineering disciplines also in rock engineering simulating construction cases by means of numerical modelling becomes more and more important (e.g. Day et al., 2019). Viewed in general terms, joints could be considered (i) implicitly in continuum approaches, for example by using the GSI-based Hoek-Brown-Criterion (latest edition see Hoek and Brown, 2019) in the finite element method (FEM), or (ii) explicitly by using discrete fracture networks (DFN) incorporated in discrete element method (DEM) models. The usefulness of contact elements in FEM models instead is limited since only small displacements could be considered. Indeed, surface representations captured with optical measuring techniques as used in this thesis could be introduced in such models. However, computational efficiency is a problem (Lei et al., 2017) and it would decrease by introducing more complex geometries based on high-resolution scans. In the end, models for most engineering projects would have to extend over tens or a few hundreds of metres which makes simulations of sub-millimetres effects appear questionable and, in any case, unfeasible at the time being. However, DFNs in conjunction with spatial roughness characterisation as a possibility of more realistic modelling should of course be explored also for engineering cases in the future.

5.4 References

Abellan, A., Derron, M.-H., and Jaboyedoff, M. (2016). "Use of 3D Point Clouds in Geohazards" Special Issue: Current Challenges and Future Trends. *Remote Sensing*, 8(2):130. https://doi.org/10.3390/rs8020130.

Bahaaddini, M., Hagan, P., Mitra, R., and Hebblewhite, B. (2014). Scale effect on the shear behaviour of rock joints based on a numerical study. *Engineering Geology*, 181:212–223. https://doi.org/10.1016/j.enggeo.2014.07.018.

Ban, L., Qi, C., Chen, H., Yan, F., and Ji, C. (2020). A new criterion for peak shear strength of rock joints with a 3d roughness parameter. *Rock Mech Rock Eng*, 53(4):1755–1775. https://doi.org/10.1007/s00603-019-02007-z.

Bandis, S., Lumsden, A., and Barton, N. (1981). Experimental studies of scale effects on the shear behaviour of rock joints. *Int J Rock Mech Min*, 18(1):1–21. https://doi.org/10.1016/0148-9062(81)90262-x.

Barton, N. and Bandis, S. (1982). Effects of block size on the shear behavior of jointed rock. *Proceedings 23rd Symp. Rock Mechanics, August 25-27, 1982, Berkeley, CA*.

Barton, N. and Choubey, V. (1977). The shear strength of rock joints in theory and practice. *Rock Mech*, 10(1-2):1–54. https://doi.org/10.1007/bf01261801.

Day, J. J., Diederichs, M. S., and Hutchinson, D. J. (2019). Composite geological strength index approach with application to hydrothermal vein networks and other intrablock structures in complex rockmasses. *Geotech Geol Eng*, 37(6):5285–5314. https://doi.org/10.1007/s10706-019-00980-4.

Dong, H., Guo, B., Li, Y., Si, K., and Wang, L. (2017). Empirical formula of shear strength of rock fractures based on 3d morphology parameters. *Geotechnical and Geological Engineering*, 35(3):1169–1183. https://doi.org/10.1007/s10706-017-0172-5.

Eltner, A., Kaiser, A., Castillo, C., Rock, G., Neugirg, F., and Abellán, A. (2016). Image-based surface reconstruction in geomorphometry – merits, limits and developments. *Earth Surf Dynam*, 4(2):359–389. https://doi.org/10.5194/esurf-4-359-2016.

Ficker, T. and Martišek, D. (2016). Alternative method for assessing the roughness coefficients of rock joints. *J Comput Civil Eng*, 30(4):04015059. https://doi.org/10.1061/(asce)cp.1943-5487.0000540.

García-Luna, R., Senent, S., and Jimenez, R. (2021). Using telephoto lens to characterize rock surface roughness in SfM models. *Rock Mech Rock Eng*. https://doi.org/10.1007/s00603-021-02373-7.

Grasselli, G. (2001). *Shear Strength of Rock Joints based on quantified Surface Description*. PhD thesis, Ecole polytechnique federale de Lausanne.

Grasselli, G. and Egger, P. (2003). Constitutive law for the shear strength of rock joints based on three-dimensional surface parameters. *Int J Rock Mech Min*, 40(1):25–40. https://doi.org/10.1016/s1365-1609(02)00101-6.

Grasselli, G., Wirth, J., and Egger, P. (2002). Quantitative three-dimensional description of a rough surface and parameter evolution with shearing. *Int J Rock Mech Min*, 39(6):789–800. https://doi.org/10.1016/s1365-1609(02)00070-9.

Gravanis, E. and Pantelidis, L. (2019). Determining of the joint roughness coefficient (JRC) of rock discontinuities based on the theory of random fields. *Geosciences*, 9(7):295. https://doi.org/10.3390/geosciences9070295.

Hoek, E. and Brown, E. (2019). The Hoek-Brown failure criterion and GSI – 2018 edition. *J Rock Mech Geotech Eng*, 11(3):445–463. https://doi.org/10.1016/j.jrmge.2018.08.001.

Huang, M., Hong, C., Ma, C., Luo, Z., Du, S., and Yang, F. (2020). A new representative sampling method for series size rock joint surfaces. *Sci Rep*, 10(1):9129. https://doi.org/10.1038/s41598-020-66047-0.

ISO 14689 (2017). Geotechnical investigation and testing — identification, description and classification of rock. Standard, International Organization for Standardization, Geneva, CH. https://www.iso.org/standard/66347.html.

ISRM (1978). Suggested methods for the quantitative description of discontinuities in rock masses. *Int J Rock Mech Min*, 15(6):319–368. https://doi.org/10.1016/0148-9062(78)91472-9.

Jang, B.-A., Kim, T.-H., and Jang, H.-S. (2010). Characterization of the three dimensional roughness of rock joints and proposal of a modified shear strength criterion. *Journal of Engineering Geology*, 20(3):319–327.

Kulatilake, P., Shou, G., Huang, T., and Morgan, R. (1995). New peak shear strength criteria for anisotropic rock joints. *Int J Rock Mech Min*, 32(7):673–697. https://doi.org/10.1016/0148-9062(95)00022-9.

Lee, Y.-K., Park, J.-W., and Song, J.-J. (2014). Model for the shear behavior of rock joints under CNL and CNS conditions. *Int J Rock Mech Min*, 70:252–263. https://doi.org/10.1016/j.ijrmms.2014.05.005.

Lei, Q., Latham, J.-P., and Tsang, C.-F. (2017). The use of discrete fracture networks for modelling coupled geomechanical and hydrological behaviour of fractured rocks. *Comput Geotech*, 85:151–176. https://doi.org/10.1016/j.compgeo.2016.12.024.

Li, Y. and Huang, R. (2015). Relationship between joint roughness coefficient and fractal dimension of rock fracture surfaces. *Int J Rock Mech Min*, 75:15–22. https://doi.org/10.1016/j.ijrmms.2015.01.007.

Li, Y., Mo, P., Aydin, A., and Zhang, X. (2019). Spiral sampling method for quantitative estimates of joint roughness coefficient of rock fractures. *Geotech Test J*, 42(1):245–255. https://doi.org/10.1520/gtj20170213.

Li, Y., Tang, C., Li, D., and Wu, C. (2020). A new shear strength criterion of three-dimensional rock joints. *Rock Mech Rock Eng*, 53(3):1477–1483. https://doi.org/10.1007/s00603-019-01976-5.

Li, Y. and Zhang, Y. (2015). Quantitative estimation of joint roughness coefficient using statistical parameters. *Int J Rock Mech Min*, 77:27–35. https://doi.org/10.1016/j.ijrmms.2015.03.016.

Liu, Q., Tian, Y., Ji, P., and Ma, H. (2018). Experimental investigation of the peak shear strength criterion based on three-dimensional surface description. *Rock Mech Rock Eng*, 51(4):1005–1025. https://doi.org/10.1007/s00603-017-1390-0.

Liu, X., Zhu, W., and Li, L. (2020). Numerical shear tests on the scale effect of rock joints under CNL and CND conditions. *Adv Civil Eng*, 2020:1–15. https://doi.org/10.1155/2020/6465231.

Magsipoc, E., Zhao, Q., and Grasselli, G. (2020). 2d and 3d roughness characterization. *Rock Mech Rock Eng*, 53(3):1495–1519. https://doi.org/10.1007/s00603-019-01977-4.

Schmittbuhl, J., Vilotte, J.-P., and Roux, S. (1995). Reliability of self-affine measurements. *Phys Rev E*, 51(1):131–147. https://doi.org/10.1103/physreve.51.131.

Singh, H. and Basu, A. (2018). Evaluation of existing criteria in estimating shear strength of natural rock discontinuities. *Eng Geol*, 232:171–181. https://doi.org/10.1016/j.enggeo.2017.11.023.

Stigsson, M. and Mas Ivars, D. (2019). A novel conceptual approach to objectively determine JRC using fractal dimension and asperity distribution of mapped fracture traces. *Rock Mech Rock Eng*, 52(4):1041–1054. https://doi.org/10.1007/s00603-018-1651-6.

Tatone, B. S. (2009). Quantitative characterization of natural rock discontinuity roughness in-situ and in the laboratory. Master's thesis, University of Toronto.

Tse, R. and Cruden, D. (1979). Estimating joint roughness coefficients. *Int J Rock Mech Min*, 16(5):303–307. https://doi.org/10.1016/0148-9062(79)90241-9.

Wang, L., Wang, C., Khoshnevisan, S., Ge, Y., and Sun, Z. (2017). Determination of two-dimensional joint roughness coefficient using support vector regression and factor analysis. *Eng Geol*, 231:238–251. https://doi.org/10.1016/j.enggeo.2017.09.010.

Yang, J., Rong, G., Hou, D., Peng, J., and Zhou, C. (2016). Experimental study on peak shear strength criterion for rock joints. *Rock Mech Rock Eng*, 49(3):821–835. https://doi.org/10.1007/s00603-015-0791-1.

Yong, R., Ye, J., Liang, Q.-F., Huang, M., and Du, S.-G. (2018). Estimation of the joint roughness coefficient (JRC) of rock joints by vector similarity measures. *B Eng Geol Environ*, 77(2):735–749. https://doi.org/10.1007/s10064-016-0947-6.

List of Figures

List of Tables

Chapter A

Appendix

Declaration of academic integrity
(*Eidesstattliche Versicherung*)

I hereby declare in lieu of an oath that I have written this dissertation independently. All sources and aids used are listed and the information on personal contributions in the case of co-authorship is correct.

Hiermit erkläre ich an Eides statt, dass ich diese Dissertation selbstständig verfasst habe. Alle benutzen Quellen und Hilfsmittel sind aufgeführt und die Angaben zu den Eigenanteilen bei Co-Autorenschaft sind zutreffend.

Berlin, 11. August 2021

The author's contribution (*Erklärung zum Eigenanteil*)

This thesis consists of three manuscripts, which form chapters 2, 3 and 4. The author's contributions are as follows:

Chapter 2 — First author

On the usability of different optical measuring techniques for joint roughness evaluation

All authors developed the concept and the design of the study. The author and the co-author Daniel Wujanz conducted the laboratory work and processed the data. The author wrote the evaluation algorithms and collected the literature for the study. The author wrote the original draft and handled the manuscript during the editorial process. The co-author Tomas M. Fernandez-Steeger contributed to the review and editing. All authors reviewed and approved the final version of the manuscript.

Chapter 3 — First author

Comparative Evaluation of Statistical and Fractal Approaches for JRC Calculation Based on a Large Dataset of Natural Rock Traces

Both authors developed the concept of the study. The author conducted the laboratory work, processed the data, and wrote the evaluation algorithms. The author collected the literature for this study. Both authors interpreted the results. The author wrote the manuscript, supported by suggestions from the co-author.

Chapter 4 — First author

Incoherency of replica-based shear strength criteria regarding tensile fractures with high wall strength

The author posed the overall research question and developed the concept of the study, supported by the co-author. The author conducted the laboratory work, analysed the data, and collected the literature for the study. Both authors interpreted the results. The author wrote the manuscript, supported by suggestions from the co-author.

Acknowledgments

First of all, I would like to thank Prof. Joachim Tiedemann, who gave me the opportunity to start a doctorate in the first place. I would also like to thank the chair of the doctoral committee, Prof. Frank Rackwitz, and the reviewer, Prof. Kurosch Thuro, for the pleasant procedure.

My special thanks go to the supervisor of this thesis, Prof. Tomas Fernandez-Steeger, who gave me great freedom in working on the topic and always had an open ear for fruitful discussions. He supported me continuously.

Sincere thanks go to Dr. Daniel Wujanz, with whom I collaborated for the first manuscript. At his suggestion, I gave my first talk at an international conference. It was fun and enriching to work with him.

I would also like to thank my family: my parents, my sister and my brother, who have supported and cheered me on my way.

Above all, I owe a great debt of gratitude to my partner and my young son, who often had to do without me.